*American Mineralogist Manuscript #4837 – Revision 1*

# The petrogenesis of impact basin melt rocks in lunar meteorite Shişr 161

Axel Wittmann[1,*], Randy L. Korotev[1], Bradley L. Jolliff[1], Thomas J. Lapen[2], and Anthony J. Irving[3]

[1] Department of Earth and Planetary Sciences, Washington University St. Louis, Campus Box 1169, 1 Brookings Dr., St. Louis, MO 63130-4899, USA

[2] Department of Earth and Atmospheric Sciences, University of Houston, 4800 Calhoun Road, Houston, Texas 77004.

[3] Department of Earth and Space Sciences, University of Washington, 4000 15th Avenue NE, Seattle, Washington 98195.

*corresponding author e-mail address: wittmann@levee.wustl.edu

## ABSTRACT

This study explores the petrogenesis of Shişr 161, an immature lunar regolith breccia meteorite with low abundances of incompatible elements, a feldspathic affinity, and a significant magnesian component. Our approach was to identify all clasts >0.5 mm in size in a thin section, characterize their mineral and melt components, and reconstruct their bulk major and minor element compositions. Trace element concentrations in representative clasts of different textural and compositional types indicate that the clast inventory of Shişr 161 is dominated by impact melts that include slowly cooled cumulate melt rocks with mafic magnesian mineral assemblages. Minor exotic components are incompatible-element-rich melt spherules and glass fragments, and a gas-associated spheroidal precipitate. Our hypothesis for the petrologic setting of Shişr 161 is that the crystallized melt clasts originate from the upper ~1 km of the melt sheet of a 300 to 500 km diameter lunar impact basin in the Moon's feldspathic highlands. This hypothesis is based on size requirements for cumulate impact melts and the incorporation of magnesian components that we interpret to be mantle-derived. The glassy melts likely formed during the excavation of the melt sheet assemblage, by an impact that produced a >15 km diameter crater. The assembly of Shişr 161 occurred in a proximal ejecta deposit of this excavation event. A later impact into this ejecta deposit then launched Shişr 161 from the Moon. Our geochemical modeling of remote sensing data combined with the petrographic and chemical characterization of Shişr 161 reveals a preferred provenance on the Moon's surface that is close to pre-Nectarian Riemann-Fabry basin.

**Keywords:** Lunar meteorite, spherule, Feldspathic Highlands Terrane, impact melt, cumulate, Riemann-Fabry basin.

## INTRODUCTION

At present, 43 of the 96 distinct lunar meteorites (exclusive of pairings) are feldspathic breccias with bulk rock $Al_2O_3$ contents ≥25 wt%, FeO <8 wt%, and Th <1 ppm (<http://meteorites.wustl.edu/lunar/>, last accessed February 3, 2014), implying launch from the lunar highlands at locations with no significant contribution of material from the incompatible element-enriched Procellarum KREEP-Terrane (Jolliff et al. 2000). About 70% of these feldspathic breccias have a ferroan character in that bulk rock Mg# [Mg/(Mg/Fe) in mol%] is <70 (e.g., Korotev et al. 2006). The ferroan character of these meteorites is consistent with the idea that the ferroan anorthositic lunar crust had an average Mg# of ~63 (e.g., Warren 1990). The remaining feldspathic breccia meteorites, however, are more magnesian, with Mg# >70, suggesting the presence of a magnesian mafic component that occurs ubiquitously near the surface of the lunar highlands (Korotev and Jolliff 2001; Treiman et al. 2010). The nature of this magnesian component remains elusive. Mixing with magnesian-suite rocks that are interpreted as intrusions into the crust (Lindstrom and Lindstrom 1986; Warren 1986; Shearer and Papike 2005; Treiman et al. 2010), or the incorporation of mantle rocks into the impact melts of large lunar impact craters (Hess 1994; Vaughan et al. 2013) are possible scenarios.

Collected in the Dhofar governorate of Oman in 2008, lunar meteorite Shişr 161 (Fig. 1) is a 57.2 g feldspathic, clast-rich regolith breccia (Foreman et al. 2009) with a feldspathic bulk rock chemical composition, a Mg# of 71, and a Th concentration of 0.16 ppm (Foreman et al. 2009; Korotev 2012), pointing to an origin in or near the feldspathic lunar highlands. In order to characterize the origin and petrological settings of magnesian lunar highlands rocks, we surveyed the lithologic inventory of Shişr 161.

## SAMPLES AND METHODS

We analyzed one rectangular thin section that captures a sample area of 547 $mm^2$ of Shişr 161 under the petrographic microscope. Using optical microscopy, we identified ca. 90 clasts in the section (Fig. 2), including all clasts >0.5 mm in size. Using back-scattered electron (BSE) images and energy dispersive spectrometry, we verified mineral identification using the JEOL 8200 electron microprobe (EMP) in the Department of Earth and Planetary Sciences, Washington University in St. Louis. We determined the sizes and proportions of major and minor mineral components in BSE images of these clasts using the image analysis software ImageJ (National Institutes of Health, < http://rsbweb.nih.gov/ij/>). We analyzed the chemical composition of each mineral and melt component with the EMP, using an acceleration voltage of 15 kV, an electron beam current of 15 nA, and varied beam diameters ranging from 1 µm to 20 µm, depending on the nature and size of components. To avoid volatilization of Na, we used beam diameters between 5 and 20 µm for glassy domains and determined concentrations of the elements Si, Ti, Al, Fe, Ca, Mg, Na, K, Cr, Ni, P, S, and Mn in silicates and oxides with wavelength-dispersive spectroscopy. For the silicate measurements, we set the electron beam to analyze Na, Mg, Al, and Si for 60 seconds (35 seconds on the peaks, and 2×12.5 seconds on the respective backgrounds) and for the analyses on K, Ca, Mn, Fe, Ti, Cr, Ni, P, and S to 35 seconds (20 seconds on the peaks, and 2×7.5 seconds on the respective backgrounds). We measured natural and synthetic standard materials for our calibration and data reduction, which yielded typical detection limits of 0.02 wt% for MgO, $Al_2O_3$, $K_2O$ and $SO_3$, 0.03 wt% for $Na_2O$, $SiO_2$, CaO and $P_2O_5$, 0.04 for $TiO_2$ and $Cr_2O_3$, 0.05 for MnO and FeO, and 0.06 wt% for NiO. For the analysis of metal and sulfide components, we used a different analytical set-up that included the elements P, S, Mg, Si, Cr, Fe, Cu, Ni, Ti, Zn, Mn, and Co. For these measurements, we set the electron beam to analyze all elements for 60 seconds (30 seconds on the peaks, and 2× 15 seconds on the respective backgrounds). We set our backgrounds appropriately to avoid the interference of the Fe-$K_{\alpha}$ X-ray peak with the Co $K_{\beta}$ X-ray peak and attained typical detection limits of 0.02 wt% for P, S, Mg, Si and Cr, 0.03 wt% for Fe and Mn, 0.04 wt% for Ti and Co, and 0.05 wt% for Ni. Repeated analyses with the JEOL 8200 on standard reference materials give typical one-sigma relative errors better than 2 % for element concentrations >10 wt%, better than 5% for element concentrations between <10 and ~0.5 wt%, and relative errors >10 % for smaller concentrations.

To determine bulk rock compositions for clasts, we did modal recombination by calculating the vol% abundances of major and minor elements from the compositions and proportions of the respective mineral components in the clasts. Then, we recalculated the wt% concentrations by using appropriate density corrections following the method of Berlin (2009). Following the reasoning of Treiman et al. (2010) for the evaluation of the level of uncertainty in modal mineral abundances, we estimate typical 2σ of wt% standard errors for our modally recombined bulk clast compositions of ≤5 % for the major and minor oxide components and ≤50 % for trace concentrations of the oxide values.

At the University of Houston, we determined the concentrations of 35 trace elements for 24 clasts in Shişr 161 by laser ablation-inductively coupled plasma-mass spectrometry (LA-ICP-MS) with a Varian 810 ICP-MS, using a 193 nm excimer laser (Analyte.193 ultra-short pulse excimer ablation system, Photon Machines Inc.) that we focused to diameters of 50 and 90 μm and operated at a repetition rate of 8 Hz. We processed the concentration data with the LA-ICP-MS data reduction software Glitter (Access Macquarie Ltd.), using Si or Ca abundances determined by EMP for the analyzed clasts and minerals as internal, and United States Geological Survey basalt glasses BHVO-2 and BIR-1 as external standards. For the reproducibility of multiple standard analyses we generally found a 2–13% relative standard deviation to published values for BHVO-2 and BIR-1 (GeoReM, Max-Planck Institut fuer Chemie 2006, http://georem.mpch-mainz.gwdg.de/sample_query_pref.asp).

## RESULTS

### Petrography

Shişr 161 is a 4×3×3 cm polymict breccia stone with a brown color and no recognizable fusion crust (Fig. 1). Angular clasts <1 cm in size are embedded in a well indurated, clastic groundmass that has an estimated average grainsize of 5 µm. Some particles have transitional, interfingering contacts with the breccia groundmass, suggesting emplacement while they were still melted. Shock metamorphic features occur in abundance in the lithologic inventory of Shişr 161. They range from brittle to crystal-plastic deformation such as mosaicism in olivine and pyroxene to planar deformation features in plagioclase (Appendix-Fig. A1), diaplectic feldspar glass (maskelynite, Appendix-Fig. A2), bulk rock impact melting, impact melt spherules with accreted clastic debris (Heiken et al. 1974; Delano 1986), and even a possible gas-associated spheroidal precipitate (GASP, Warren 2008).

Overall, terrestrial weathering of Shişr 161 is minor. Nonetheless, magnesian olivine is in places replaced by phyllosilicates, veins of Ca carbonate fill fracture spaces, and secondary celestine and barite crystals occur.

We characterized all 40 clasts >0.5 mm$^2$ in size (which are typically larger than ~1 mm in maximum length) petrographically and determined their compositions. In order to attain a more complete estimate of lithological and compositional variability, we complemented this quantitative study of the largest clasts with smaller clasts (the smallest being a 0.002 mm$^2$ spherule), altogether characterizing 94 clasts under the electron microprobe.

**Matrix and ungrouped, mono- and polymineralic clasts.** The groundmass of particles <5 µm in size accounts for <50 vol% of the rock. Clasts up to 0.5 $mm^2$ in size are mono and polycrystalline rock and glass fragments and glassy to crystallized spherules. While most of these fragments could be derived from the lithologies represented by larger component clasts, some are exotic. These include ferroan pyroxene crystals composed of pigeonite with fine, ~5 µm thick lamellae of augite, a few plagioclase fragments that are relatively rich in $Na_2O$, one fragment with forsteritic olivine laths embedded in a feldspathic mesostasis that constitute a texture reminiscent of a barred olivine chondrule (Appendix-Fig. A3), and a grain that contains kamacite with Ni and Co abundances typical for L-chondrites.

**Spherules.** Thirteen spherules are 0.002 to 0.163 $mm^2$ in size, occupying a combined area of 0.316 $mm^2$ (Table 1). They are represented by three cryptocrystalline specimens, 7 that are vitrophyres with intersertal to hyalophitic textures, and three that are fully crystallized to intergranular textures (Fig. 3). Five of these spherules accreted clastic and melted components, two are inclusions in melt clasts, and 5 show some fracturing and abrasion that suggests reworking.

**Impact melt clasts.** The 40 clasts >0.5 $mm^2$ in size occupy 24 % of the thin section. Size spectra of constituent crystals are given in Fig. 4.

The major fraction (9 vol%) is represented by 10 granular melt clasts (Fig. 5) composed of 10 to 500 µm subhedral plagioclase and olivine crystals that are intergrown with poikilitic pyroxene crystals ± chrome spinel, ilmenite, troilite and FeNi metal particles. Very rarely, accessory chlorapatite, pentlandite, and $ZrO_2$ crystals occur. On the basis of these textures, we interpret the plagioclase and olivine crystals as cumulus crystals and the pyroxene oikocrysts as intercumulus material (Irvine 1982). Adcumulus growth likely produced subhedral shapes of plagioclase crystals, and the occasional occurrence of 120°-angles in grain junctions. In three clasts that are the most fine-grained, relict 0.5 mm plagioclase xenocrysts are present. Compositionally and texturally, rocks similar to the Shişr 161 cumulate clasts are the Apollo poikilitic granulites, which are regarded as ancient metamorphosed breccias or melt rocks (Hollister 1973; Ashwal 1975; Lindstrom and Lindstrom 1986; Cushing et al. 1999; Norman and Nemchin 2014). Melt origins are confirmed by cathodoluminescence imaging that reveals igneous, concentric zonation in the plagioclase crystals of the Shişr 161 cumulate clasts (Fig. 5c, cf. Norman and Nemchin 2014), where they have not been obscured by shock deformation.

More finely crystallized melt clasts occupy 7% of the thin section (Fig. 6). They are composed of plagioclase, olivine, and pyroxene ± chrome spinel, troilite, FeNi metal, and ilmenite (Table 2). These crystallized clasts exhibit variable textures from poikilitic to sub-ophitic, intergranular and coalescent. Most of them indicate the presence of admixed xenoliths of plagioclase ± olivine and pyroxene fragments. One xenolith-free clast of this group has a variolitic texture of intergrown, zoned plagioclase and pyroxene crystals that is reminiscent of basalt (Fig. 6f).

Vitrophyre clasts are composed of domains of glass and/or mesostasis with crystals of plagioclase, olivine and pyroxene. These clasts occupy 5% of the thin section area (Fig. 7) and have shapes that range from angular, shard-like to ameboid. These morphologies indicate that some of these clasts were emplaced, while they were melted. One of these vitrophyre clasts is a glassy coating on a cumulate clast and contains fragments of its host (Fig. 5a). Other glassy fragments contain a few µm size angular xenoliths that are fused to their outside, indicating these clasts are ropy glasses (Fruland et al. 1977; Fig. 7d; Table 3).

Two clasts, a 14.1 $mm^2$ polymict breccia (Fig. 8; clast 1 in Fig 2) and a 0.6 $mm^2$ mosaicized anorthosite (clast 14 in Fig. 2), take up 3 % of the thin section area. The polymict breccia is a complex, subrounded aggregate of similar components as in Shişr 161 that are also embedded in a fine, particulate groundmass. Its largest sub-clast is a 1.1 mm cataclastic anorthosite with less than 5 vol% anhedral pyroxene and olivine crystals.

**Clast compositions**

**Plagioclase**. Ninety per cent of the plagioclase analyses cluster at $An_{95–98}$ [An is mol% Ca/(Na+Ca+K)], including all 123 analyses associated with the 12 cumulate clasts (Fig. 9). The ranges of plagioclase compositions in crystallized melt clasts ($An_{90–98}$, number of analyses n=117) and vitrophyre clasts ($An_{89–99}$, n=90) are wider than in cumulate clasts. The $K_2O$ concentrations in plagioclase crystals of these melt clasts, and a few maskelynite grains, are up to 0.08 wt% (Appendix-Table A1) but typically near the detection limit of the EMP of 0.02 wt%. We found exotic plagioclase compositions enriched in Na and K in two monomineralic clasts ($An_{67–75}$ and $Or_{0.2–1.6}$ , n=5), in 4 spherules ($An_{81–99}$ and $Or_{0–2.3}$ , n=43), and in a barred chondrule-like clast ($An_{84–88}$ and $Or_{0.1}$ , n=3).

**Olivine.** The 283 analyses cluster around $Fo_{55–80}$ (Fig. 10; Appendix Table A2). Cumulate-clast olivine shows the narrowest range of compositions, a magnesian ($Fo_{74–79}$, n=62) and ferroan ($Fo_{46–56}$, n=22) type. Crystallized melt-clast olivine shows a weaker clustering around $Fo_{61–71}$ (n=67) and $Fo_{76–84}$ (n=24) and a few exotic compositions ($Fo_{19–51}$, n=3). The 53 analyses on olivine crystals associated with vitrophyre and ropy glass clasts and the 21 analyses of olivine crystals associated with spherules show a wide range of compositions ($Fo_{6–84}$) due to compositional zoning of phenocrysts and the presence of undigested olivine clasts. This observation is supported by the data for olivine clasts in the groundmass of Shişr 161 and olivine clasts in a polymict breccia clast that show a similarly wide range of compositions ($Fo_{6–81}$, n=23). An exotic, barred olivine chondrule-like clast contains zoned olivine with $Fo_{91–94}$. The molar Fe/Mn for Shişr 161 olivine analyses mostly cluster on the approximate trendline for lunar olivine (Fig. 11; Papike 1998), even for the highly magnesian, barred olivine crystals in a chondrule-like clast (Fig. 2). The biggest deviation from the lunar trend occurs for a number of olivine crystals associated with vitrophyre melt clasts, which appear to be relatively depleted in Mn compared with the typical trend of lunar olivine.

**Pyroxene.** Advanced equilibration is evident in all but two cumulate clasts (Fig. 12; clast 26, $En_{47–56}Fs_{38–43}Wo_{6–15}$, n=15, and $En_{39–47}Fs_{18–27}Wo_{30–37}$, n=14, and clast 38, $En_{70–79}Fs_{16–18}Wo_{4–14}$, n=7). We used the QUILF code (Andersen et al. 1993) to assess the equilibration temperatures recorded by low- and high Ca-pyroxene pairs of the cumulate clasts and found equilibration temperatures between 1100 and 900 °C. Furthermore, the cumulate clasts fall into a magnesian group (8 clasts; $En_{75–80}Fs_{18–21}Wo_{2–5}$, n=55, and $En_{47–51}Fs_{7–10}Wo_{38–45}$, n=36) and a ferroan group (2 clasts; $En_{57–72}Fs_{24–39}Wo_{5}$, n=3, and $En_{41–45}Fs_{17–21}Wo_{34–42}$, n=12).

The pyroxene compositions of 19 crystallized melt clasts ($En_{52–81}Fs_{17–44}Wo_{2–5}$, n=26; $En_{25–75}Fs_{22–56}Wo_{11–20}$, n=69; $En_{12–75}Fs_{20–25}Wo_{32–43}$, n=37; Appendix Table A3) show trends of equilibration, which is evident by relatively homogeneous compositions in the respective clasts and the presence of high- and low-Ca pyroxene pairs in some of the clasts.

The pyroxenes hosted by 12 vitrophyre clasts are unequilibrated phenocrysts or undigested clasts of orthopyroxene ($En_{56–79}Fs_{17–40}Wo_{2–5}$, n=25), pigeonite ($En_{40–67}Fs_{21–41}Wo_{6–19}$, n=12), and augite ($En_{33–49}Fs_{9–40}Wo_{25–43}$, n=6).

Associated with 6 spherules are orthopyroxene ($En_{61}Fs_{36–37}Wo_{2–3}$, n=3) clasts, and pigeonite ($En_{54–78}Fs_{17–30}Wo_{6–19}$, n=8), and augite ($En_{12–58}Fs_{17–64}Wo_{22–44}$, n=9) crystals.

Our analyses of pyroxene crystals in the groundmass of Shişr 161 and in a polymict breccia clast indicate a wide range of compositions ($En_{43–87}Fs_{10–52}Wo_{3–5}$, n=15; $En_{29–47}Fs_{18–62}Wo_{6–20}$, n=36; $En_{25–46}Fs_{13–45}Wo_{23–44}$, n=38). Among them are three 0.4 to 0.5 mm size exsolved pyroxene crystals, a Fe-rich pigeonite with exsolution lamellae of augite, a magnesian pigeonite with thin lamellae of augite, and a variably Fe-rich augite. An exotic 0.2 × 0.15 mm feldspathic clast that is a component of the large polymict breccia clast (Fig. 8) contains ~20 µm size crystals of magnesian low-Ca pyroxene ($En_{85–87}$). The molar Fe/Mn of the Shişr 161 pyroxene analyses clusters on and between the approximate trendlines for lunar and terrestrial pyroxene (Papike 1998; Fig. 13).

**Ilmenite.** Ilmenite is a rare, accessory component in Shişr 161. It is only moderately abundant in one ferroan cumulate clast and was identified as single crystals in two other cumulate clasts. These ilmenite crystals contain 2.1 to 4.3 wt% MgO and 0.1 to 0.7 wt% $Cr_2O_3$ (Appendix Table A4). In 5 crystallized melt clasts, ilmenite occurs as ~10 µm, euhedral crystals and contains 1 to 6.4 wt% MgO and 0.1 to 0.8 wt% $Cr_2O_3$ (n=7). In small clasts within the groundmass of Shişr 161, ilmenite is found as subhedral intergrowths with one pyroxene ($En_{30}Fs_{62}Wo_8$, n=2, and $En_{26}Fs_{38}Wo_{36}$, n=2) and one olivine clast ($Fo_{6–7}$, n=3); the MgO contents are <1 wt% and $Cr_2O_3$ concentrations are <0.2 wt% (n=11) in these ilmenite crystals.

**Spinel.** Our 36 analyses of spinel crystals have compositions of $Mg_{0.1–0.5}Fe_{0.5–1.6}Ti_{0–0.6}Al_{0.2–1.2}Cr_{0.5–1.4}O_4$ (Appendix Table A5, Fig. 14). Five magnesian cumulate clasts contain spinel crystals with similar compositions ($Mg_{0.2–0.3}Fe_{0.5–0.6}Ti_{0.05–0.16}Al_{0.2–0.3}Cr_{1.2–1.3}O_4$; n=20), and one that is notably different in that it is enriched in $Al_2O_3$ ($Mg_{0.5}Fe_{0.5}Ti_{0.03}Al_{1.2}Cr_{0.8}O_4$). Rare spinel in a ferroan cumulate clast is enriched in FeO and $TiO_2$ ($Mg_{0.1}Fe_{1.6}Ti_{0.59}Al_{0.2}Cr_{0.5}O_4$) compared to the spinel crystals found in the magnesian cumulate clasts. Our analyses of spinel crystals in 6 crystallized melt clasts indicate compositions of $Mg_{0.1–0.5}Fe_{0.5–1.3}Ti_{0.01–0.53}Al_{0.3–1.1}Cr_{0.7–1.3}O_4$ (n=8). The spinel crystals associated with 5 vitrophyre clasts fall in a range of compositions between $Mg_{0.1–0.5}Fe_{0.5–1}Ti_{0.01–0.16}Al_{0.4–1.1}Cr_{0.8–1.3}O_4$, (n=6) and one with a composition close to spinel *sensu stricto* ($Mg_{0.9}Fe_{0.1}Al_2O_4$) of a euhedral crystal in a vitrophyre clast that is part of a polymict breccia clast (Fig. 8).

**Metal and sulfide particles.** Sufficiently large metal particles for EMP analysis (>3 μm in size) occur in four vitrophyre clasts, three spherules, as three 40 to 120 μm nuggets in the breccia groundmass (of which only two were analyzed), in 9 crystallized melt clasts (Appendix Table A6), and in 10 cumulate clasts (Fig. 15). Metal particles in most cumulate clasts and in three crystallized melt clasts have Ni concentrations >35 wt% (Appendix Table A6). Although their compositions can vary within the same clast, Ni and Co abundances cluster around the chondritic ratio of 20:1, suggesting a meteoritic impactor signature (e.g., Warren 1993), and, thus, an impact-induced petrogenesis of these clasts. The metal particles associated with vitrophyre clasts fall in the field for Apollo 17 mare basalts, and the field for most Apollo polymict rocks (Ryder et al. 1980), as do the analyses of 4 metal particles in spherules. A 60 µm metal nugget in the groundmass of Shişr 161 is an intergrowth of kamacite with tetrataenite that matches the Ni and Co compositions of such particles in L-chondrites (Clarke and Scott 1980; Affiattalab and Wasson 1980).

FeNi metal particles are typically associated with sulfide crystals (Appendix Table A7). The elevated Ni contents in some of the troilite analyses hint at possible mixture measurements of troilite and minute FeNi metal domains. A magnesian and a ferroan cumulate clast contain crystals of pentlandite, which is a rare lunar mineral (Ramdohr 1972; Carter et al. 1975; Nazarov et al. 1980; Kuehner et al. 2005).

**Vitric matrixes and glass compositions.** Table 4 shows the compositions of glass and mesostasis domains in vitrophyres and spherules. The vitrophyre clasts that only retain up to 5 µm continuous domains of melt mesostasis required modal recombination of the phenocrysts and the mesostasis melt. All glass particles except one have Mg/Al [wt%] $<1.5$, which suggests they are of impact origin, not volcanic (Delano 1986). The lone exception is the glass component of spherule 9 (Fig. 3a), which apart from a relative enrichment in $Na_2O$ matches the compositional characteristics of GASP, which Warren (2008) identifies as impact vapor condensates. The mesostases are melt residues, so their Mg/Al is not indicative of volcanic or impact origins; however, their petrographic contexts, such as accreted debris, (Figs. 3d–e; 7c–e) point to impact origins.

**Clast bulk compositions**

We determined the modal mineralogy of clasts in Shişr 161 by calculating the CIPW-norm from the recombined bulk compositions and the glass analyses for the vitrophyre clasts, and from the image analysis results for the crystallized melt clasts and the cumulate clasts (Table 5, Fig. 16). The vast majority of modal mineralogies plot between 60 and 90 vol% plagioclase in the vicinity of the estimated average composition of the lunar crust based on numerous feldspathic lunar meteorites (Korotev et al. 2003). Only 4 clasts indicate plagioclase abundances >90 vol% and only one, a 0.6 $mm^2$ cumulate clast with >95 vol% plagioclase classifies as "pure anorthosite" (Hawke et al. 2003).

### Recombined compositions and bulk compositions of clasts

Most of the clasts have major-element compositions similar to the majority of feldspathic lunar meteorites (Fig. 17), that is, the clasts are compositionally typical of the feldspathic highlands. Of those clasts that do not, a few are more feldspathic; however, most are more mafic, which may account for the relatively low $Al_2O_3$ concentration of Shişr 161 compared to other feldspathic lunar meteorites. The weighted mean averages (WMA) of all clasts indicate Mg#s of 69.1 and 23.7 wt% $Al_2O_3$, which is not close to the bulk rock composition of Shişr 161. However, if variolitic noritic gabbro clast #23 (Table 3, Figure 6F) is excluded, the WMA for the combined clasts constitutes a Mg# of 71.3 and an $Al_2O_3$ concentration of 25.3 wt%, which is in good agreement with the bulk rock composition of Shisr 161. This suggests that clast #23 was likely not represented in the bulk rock analysis of Shişr 161. The majority of the mafic clasts, largely vitrophyres and spherules, have compositions intermediate to feldspathic lunar meteorites and mare basalts. A subset falls in the compositional range of magnesian-suite norites and gabbronorites (Fig. 17). The WMA of all 52 vitrophyre and spherule clasts yields a Mg# of 65.3 and 22.3 wt% $Al_2O_3$. Several mafic clasts, including some of the crystallized and cumulates, are more magnesian and plot in the field of magnesian-suite norites and gabbronorites. The WMA of all 18 crystallized melt clasts (excluding clast #23) gives a Mg# of 69.1 and 25.8 wt% $Al_2O_3$. In contrast, the WMA for the 12 cumulate clasts is considerably more magnesian in character as indicated by the Mg# of 75.6 and 26.8 wt% $Al_2O_3$ and, thus, identifies the cumulate clasts as the main carriers for the magnesian component in Shişr 161.

Three spherules have a strong affinity to the composition of Apollo 15 KREEP basalt (Fig. 18), suggesting that they derive from impacts into the Procellarum KREEP terrane (Lucey et al. 2006). Two spherules, one that crystallized fayalitic olivine and one that appears to be a GASP plot at low Th and high FeO concentrations, suggesting they do not represent simple mixtures between typical lunar crustal lithologies. Most melt clasts cluster around the compositional range for troctolites and troctolitic anorthosites.

The chondrite-normalized Rare Earth Element (REE) patterns of 18 Shişr 161 impact melt clasts are mostly flat-trending and overlap between ~1 and 11×CI (Fig. 19). Two small gabbroic clasts with poikilitic textures of clinopyroxene oikocrysts that contain plagioclase chadacrysts are anomalous in that they are the only ones that exhibit negative Eu anomalies. Spherules also reveal distinct characteristics. The accreted portion on a mafic spherule (Fig. 3d) and a possible spherule that is an inclusion in a vitrophyre melt clast have REE abundances that fall in the typical range for the impact melt clasts in Shişr 161. In contrast, the main portion of the mafic spherule (Fig. 3d) and a GASP particle (Fig. 3a) have REE concentrations that are 1–2×CI except for a small positive Eu anomaly. Four other spherules (Fig. 3 b, c, e) show strong enrichments in incompatible elements and display REE patterns 100–400×CI, which suggests an affinity to KREEP (e.g., Papike et al. 1998 and references therein). The bulk-rock CI normalized REE patterns for two medium grained magnesian cumulate clasts are flat-trending (La/Yb 1.2–1.6; 2 to 4× enriched relative to CI; Fig. 19), with positive Eu-anomalies (Eu/Eu* 3.8 and 4.6) that are modest compared to those of some ferroan anorthosites [e.g., Eu/Eu* 34.1 for 60015,64 (Taylor et al. 1973)]. A fine-grained magnesian cumulate clast and an unequilibrated ferroan cumulate clast exhibit moderately evolved REE patterns with relative enrichments of the heavy REE of 5–8×CI (La/Yb ~0.2–0.3) and minor Eu anomalies (Eu/Eu* 1.7 and 2.4).

## DISCUSSION

### The composition of Shişr 161

We determined the clast inventory of Shişr 161 and characterized it chemically (Tables 1–6, Appendix Tables A1–A7). Our petrographic and chemical data, especially the Fe/Mn of mafic silicates (Figs. 11, 13), together with bulk rock trace element characteristics (Korotev 2012) confirm a lunar origin for Shişr 161. Here, we explore possible petrogenetic relationships among the clast components in Shişr 161 and implications for their provenance through comparison of their compositions to the composition of the lunar crust.

We calculated the normative mineralogy of 38 clasts >0.5 $mm^2$ in size and determined their modal mineralogies based on normative plagioclase abundances. Figure 20 shows the resulting normative lithological abundances of clast components in Shişr 161 and the $Al_2O_3$ content calculated from the recombined compositions and normative abundances of these clasts compared to those in the model lunar crust of Wieczorek et al. (2006) and the bulk rock composition of Shişr 161 (Korotev 2012). As discussed in the context of recombined clast compositions, variolitic, crystallized melt rock clast #23 (Fig. 6f, Table 2) was excluded from these calculations because it was not represented in the bulk chemical analysis of Shişr 161 (Korotev 2012). The results (Fig. 20) show that the clast assemblage in Shişr 161 over-represents modal lithologies with intermediate (70±10 vol%) plagioclase contents compared to abundances of such lithologies in the model upper or lower lunar crust. This suggests that the clast assemblage in Shişr 161 did not form due to a simple mixing of upper and lower crust. Nonetheless, an affinity towards a lower crustal composition is indicated by the $Al_2O_3$ contents in the clasts in Shişr 161 (Fig. 20) that closely correspond to the independently determined whole rock data of Shişr 161 (Korotev 2012). Major and minor element compositions (Figs. 17–18) do not support the possibility that admixed mare components are mainly responsible for this character. If a petrogenetic link among most clasts is assumed, then possible derivation from an impact melt volume that was produced from a melt zone in the lower crust needs to be explored.

The petrogenetic settings for widely recognized lunar impact melts are small to modest melt volumes. For example, the subophitic Apollo 16 impact melt rocks likely crystallized from ~10 m thick melt volumes (Deutsch and Stöffler 1987), and Apollo 17 poikilitic impact melt breccias have textural equivalents in impact melt rocks from an 80 m thick outcrop at Lake Mistastin crater in Labrador, whose anorthositic target rock sequence is regarded as a good analogue to the lunar highlands (Grieve 1975). In contrast, terrestrial impact craters that approach 1 km thick melt volumes produced fractionally differentiated cumulates that are reminiscent of plutonic rocks (Therriault et al. 2002). The ancient 45 multiring impact basins ≥300 km in diameter on the surface of the Moon are stratigraphic markers (Wilhelms et al. 1987) and formed enormous volumes of impact melt (Cintala and Grieve 1998a, b). Rocks that resulted from crystallization of these voluminous melts are expected to be cumulates (Morrison 1998; Vaughan et al. 2013). Recently, Norman and Nemchin (2014) suggested that Apollo melt rock 67955, which displays a similar texture than the Shişr 161 cumulate clasts, originated from the melt sheet of a lunar impact basin. These authors suggest that the on average 100 µm wide plagioclase crystals in 67955 record a crystallization interval that lasted for 10 to

100 days. The size range of plagioclase crystals in 67955 falls within the range observed in the Shisr 161 cumulate clasts of 10 to 500 µm (Fig. 4), while the average sizes of plagioclase crystals in Shişr 161 cumulate clasts is more variable (Fig. 5).

### The petrogenesis of Shişr 161 cumulate clasts

We identified the cumulate clasts in Shişr 161 as impact melts based on the presence of FeNi metal particles that cluster around the chondritic ratio of Ni:Co, grain sizes that are smaller than what is expected for pristine plutonic lunar rocks (Warren 1993), relict igneous zoning (Fig. 5c; cf. Norman and Nemchin 2014) that distinguishes them from possible metamorphic lunar rocks, and the occasional presence of xenoliths. Fractional crystallization is implicated for the formation of cumulate rocks (Irvine 1982), and this process is expected to characteristically affect the trace element inventory of such rocks, especially the abundances of incompatible trace elements.

**Progenitor lithologies.** To test the fractional crystallization hypothesis, we analyzed the concentrations of selected trace elements that are commonly used as petrogenetic indicators in lunar plutonic rocks. In the Mg# versus Ti/Sm and Mg# versus Sc/Sm diagrams (Fig. 21a–b) that were used as fractionation indexes for pyroxene and ilmenite in lunar rocks (Norman and Ryder 1980), the Shişr 161 cumulate clast data indicates affinities with the “primitive” lunar plagioclase and olivine cumulates as represented by ferroan anorthosites (Papike et al. 1998 and references therein), Apollo 17 dunite 72415/7 (Dymek et al. 1975; Laul and Schmitt 1975), and some gabbronorites (James and Flohr 1983). Moreover, except for the four KREEPy spherules, all other melt clasts share this affinity in that they also plot apart from the fields of Apollo norites, troctolites and KREEP basalts. Thus, although slightly enriched in incompatible elements compared to typical ferroan anorthosites and dunite 72415/7 (Figs. 18–19), the Shişr 161 cumulate clasts are unlikely to have been sourced from typical Apollo magnesian-suite rocks such as norites, troctolites and KREEP basalts that indicate crystallization from magmas that had previously fractionated pyroxene and ilmenite (Norman and Ryder 1980).

**Dimension of the cratering event.** What size constraints can be inferred from cumulate melt rocks for the impacts that formed them? On Earth, minimum impact melt volume thicknesses of ~1 km are required to crystallize cumulate melt rocks (Therriault et al. 2002). Using scaling relationships of (Cintala and Grieve 1998a, b) and an average crustal thickness of 50 km for the feldspathic highlands (Wieczorek et al. 2013), we can constrain the size of the source crater for the magnesian cumulate impact melt clasts in Shişr 161. An impact melt zone with a maximum depth of 50 km that reaches the bottom of the feldspathic highlands crust requires a transient cavity diameter of 200 km, which corresponds to a final crater diameter on the order of 300 to 500 km (Petro and Pieters 2008). This impact event would form a melt volume on the order of $10^5$ $km^3$, 40 % of which was ejected (Cintala and Grieve 1998a). Neglecting crater floor topography, the melt volume retained in the transient crater region could form a layer with an average thickness of 1.9 km. Geometric relationships of the spherical melt zone suggest that on the order of 3 % of this melt volume would have been derived from the upper mantle below the on average 50 km thick lunar crust. This example for the smallest basin-size impacts is a minimum case. Smaller craters are unlikely for two reasons. First, such craters would not form melt zones that reach the lower crust or upper mantle. Next, their melt sheets are unlikely to be thick enough to form the medium to coarse, granular textures that have to relate to km-thick melt volumes (Warren et al. 1996). Lunar craters between 100–200 km in diameter form from transient crater diameters on the order of 60 to 100 km with melt zones <25 km deep, and retain about $5\times10^3$ $km^3$ of impact melt that could amount to a 0.7 km thick layer across the area of the transient crater. It seems implausible that these scenarios can account for the chemical and textural characteristics of the magnesian cumulate clasts in Shişr 161. On the other hand, lunar impact basins with diameters >500 km would have formed from transient craters >330 km in diameter with melt zones down to at least 110 km and associated melt volumes of ~$10^6$ $km^3$ (Cintala and Grieve 1998a, b; Petro and Pieters 2008). On the order of 60 to 70 % of these impact-melt volumes would have been generated from the upper lunar mantle and could form 7 km thick melt sheets in the region of the transient crater. If vaporization and ejection of the upper target section is taken into account (Cintala and Grieve 1998) and assimilation of crustal material that slumps back into the crater is disregarded (a process that is poorly constrained, cf. Melosh et al. 2013; Potter et al. 2013), almost all impact melt retained in the region of the transient crater could have formed from upper mantle material in these scenarios. Compared to Shişr 161, we would expect to find much higher MgO and FeO contents in melt clasts and possibly clasts of ultramafic rocks in a breccia that was generated from the upper few km of such a >500 km diameter lunar impact basin (Hess 1994; Vaughan et al. 2013).

**Petrologic modeling**. In order to test the petrogenesis of the Shişr 161 cumulate clasts from the melt zone of a 300–500 km diameter lunar impact basin in the feldspathic highlands, we modeled their compositions as mineral assemblages that would result from the crystallization of impact melts using the MELTS code (Ghiorso and Sack 1995). As input compositions, we used various proportions of feldspathic crust mixed with magnesium-rich rocks that indicate similar primitive trace element characteristics as the Shişr 161 cumulate clasts (Fig. 21). We chose the approximate composition of the typical feldspathic crust (FC) that is based on feldspathic lunar meteorites (Korotev et al. 2003), and dunite (DU) 74215/7 (Gast et al. 1973) and gabbronorite (GN) 61224 (Marvin and Warren 1980) as admixed, MgO-rich upper-mantle components (modeled compositions: FC + 5, 10, and 15 % DU; FC + 5, 10, and 15 % GN; 100 % FC; and 34 % FC, 33 % DU, and 33 % GN). Petrologic models were done at 50 bar pressure that corresponds to a depth of 1 km on the Moon, $fO_2$ of iron-wüstite, and the starting temperature of 1700 °C that is estimated as the temperature of the Sudbury basin's impact melt sheet after initial equilibration with entrained clasts (Zieg and Marsh 2005).

Our simulated equilibrium crystallization over the temperature range of 1700–~1100 °C for the model composition of FC + 10 % DU yields an assemblage that most closely resembles the mineralogy of magnesian cumulate clasts in Shişr 161 (Table 7). This simulation reproduces proportions and compositions of olivine and plagioclase within their observed ranges. Pyroxene compositions are poor matches, likely because crystallization temperatures were above the subsolidus equilibration temperatures of the orthopyroxene–augite assemblages of the Shişr 161 magnesian cumulate clasts. Nonetheless, pyroxene Mg/Fe molar ratios are reasonably close to the observed range (Table 7). Spinel abundances are noticeably larger, and their compositions do not resemble those in Shişr 161 magnesian cumulate clasts. Model runs of pure FC and mixtures of FC with gabbronorite fail to produce Mg/Fe molar ratios for pyroxenes or olivine compositions and abundances close to the ranges observed for the Shişr 161 magnesian and ferroan cumulate clasts (Table 7).

Our simulations of the fractional crystallization of an impact melt volume dominated by FC over the temperature interval of 1700–1000 °C using MELTS produced crystallization sequences that mainly reproduce the petrographically observed assemblages in the magnesian and ferroan cumulate clasts in Shişr 161 (Fig. 22). These crystallization sequences are characterized by initial fractions of <1 wt% spinel that is more dense than its parent melt but crystallizes with ~neutral buoyant plagioclase (Table 8). Next, olivine co-crystallizes with plagioclase. This olivine typically has a higher density than its parent melt and is, thus, likely to fractionate. However, plagioclase has a density contrast less than 0.04 g/cm$^3$, which suggests it is unlikely to fractionate from the melt. Moreover, all FC-dominated melt compositions crystallize 70 to 55 wt% plagioclase before the onset of pyroxene crystallization. This means that only early crystallizing spinel and olivine could fractionate from the melt and form cumulate layers. However, because olivine co-precipitates with plagioclase, the neutral buoyant plagioclase first impedes the settling of olivine and ultimately freezes the melt body when it reaches ~50 % crystallinity (Marsh 1981). Thus, fractional crystallization of FC + 5 to 15 % DU or GN is arrested before pyroxene replaces olivine on the liquidus, suggesting pyroxene crystallizes from interstitial melt in a troctolitic cumulate. This prediction is in good agreement with the petrographic evidence from the Shişr 161 magnesian cumulate clasts. The three ferroan cumulate clasts in Shişr 161, on the other hand, may be products of poorly homogenized portions of a melt sheet that was mainly composed of feldspathic crust. The sequence of crystallization and compositions of crystallized major mineral phases is similar to the mineralogy of the three ferroan cumulate clasts. However, the diversity of modal and crystal-chemical compositions among these ferroan clasts precludes conclusive statements about their origins.

### Petrogenesis of the clast assemblage in Shişr 161

Although a random nature of the clast assemblage in Shişr 161 can not be ruled out completely, we want to explore possible petrogenetic links between the major clast types, which could provide evidence for a shared petrogenesis. This is supported by grossly similar chemical characteristics of these impact melt clasts (Figs. 9, 18, 19, 21).

**Comparison with terrestrial impactite assemblages.** On Earth, only the 1.85 Ga old, ~200 km final rim diameter Sudbury impact structure in Canada (e.g., Grieve et al. 1991; Deutsch 1994; Therriault et al. 2002; Grieve 2006) has the full range of impactites exposed from its sub-crater floor to post-impact sedimentary regolith (Grieve 2006; Fig. 23) and scales to the size of a ~300 km diameter lunar impact basin (Simonds et al. 1976). Under lunar conditions, the ~$10^5$ $km^3$ impact melt volume expected to form in such an event (Cintala and Grieve 1998a) would spread out over a much larger region due to more extensive crater modification in the low gravity environment (e. g., Warren et al. 1996). Nonetheless, scaling relationships of Cintala and Grieve (1998a, b) infer that sufficient melt would be retained in such a crater to form a continuous melt sheet that is >1 km thick, which is deemed necessary to induce fractional crystallization (Therriault et al. 2002). Comparison with the stratigraphic succession that is to be expected for an impactite deposit in such a 300–500 km diameter lunar impact basin reveals that the fractionally differentiated cumulate rocks are overlain by a decameter-thick succession of crystallized and partly assimilated melt rocks that represent a quenched layer. Fallback breccia on this layer was likely much thinner than at Sudbury (Settle 1980), where the equivalent Onaping breccia is interpreted as excessively thick due to impact melt interacting with water (Kieffer and Simonds 1980; Grieve et al. 2010). Nonetheless, a breccia deposit of quenched fallback debris, possibly on the order of ~100 m thick, appears probable. This breccia would form a chilled, insulating lid on top of the massive melt sheet that would begin to fractionally crystallize. The chilled layer may be texturally variable and contain abundant fragments of undigested target rock clasts and intrusions from the underlying melt sheet (Ames et al. 2002). Moreover, extensive heating from the cooling impact melt sheet below would lead to partial assimilation, the formation of intrusive melt pods, and possibly some contact-metamorphism. The uppermost portion of this fallback breccia would contain late fallback materials such as glassy spherules (Fig. 3) that could become devitrified due to heating from below. Examples for such deposits are known from the 10.5 km diameter Bosumtwi crater in Ghana (Koeberl et al. 2007) and the 18 km diameter El'gygytgyn crater in Siberia (Goderis et al. 2013; Wittmann et al. 2013), where glassy impact melt spherules form fallback layers within the craters. These spherules indicate formation as melt droplets sourced from the uppermost target rocks and impactor material and occasionally contain accreted lithic debris. Most of these spherules do not indicate formation as impact vapor condensates such as the lunar HASP and GASP (Warren 2008; Fig. 3a) because they do not display relative enrichments or depletions in refractory components, which characterize HASP and GASP.

**Implications for the excavation of Shişr 161 cumulates.** Constraints for the approximate volumes of impact melt associated with melt rock textures outlined above

(Grieve 1975; Deutsch and Stöffler 1987) suggest that the crystallized melt rocks that were cooled too rapidly to fractionally differentiate were sourced from melt volumes between ~0.01 and 1 km thick (Fig. 23). In order to excavate cumulate melt rocks from a depth of ~1 km on the Moon, scaling relationships of Melosh (1989) suggest an impact event is required that produces a transient crater ~10 km in diameter, which scales to a final crater on the order of 15 km in diameter (Simonds et al. 1976). However, in order to attain a high proportion of cumulate rocks from a depth of ~1 km, much larger events are favorable, and deposition within ~1 radius around the crater rim appears to be required in order to avoid excessive dilution of primary ejecta (Morrison and Oberbeck 1978; Hörz et al. 1983). This excavation event furthermore could account for the production of rapidly quenched glassy melts, ropy glasses, and maskelynite (Fig. 7). Ejecta from such an impact would be mixed with surficial debris according to the theory of ballistic sedimentation (Oberbeck 1975; Oberbeck et al. 1975). The presence of impact melt spherules, GASP, and ropy glass, the scarcity / absence of agglutinates, and the relatively low concentrations of siderophile elements in Shişr 161 support this interpretation and are characteristic of immature regolith breccias (McKay and Basu 1983; McKay et al. 1986; Foreman et al. 2009; Korotev 2012) that could have been deposited in proximal ejecta deposits of mid-size impact craters (Fruland et al. 1977; Warren 2008). A third impact would then be required to launch Shişr 161 from the Moon.

**Provenance of Shişr 161**

In order to constrain the provenance of Shişr 161 on the surface of the Moon, we did least squares modeling of its bulk rock composition (Korotev 2012) with the Lunar

Prospector's 5° gamma-ray spectrometer data (Fig. 24; Prettyman et al. 2006). This technique has previously been used to constrain the provenances of regolith breccias on the Moon's surface (e.g., Jolliff et al. 2009; Joy et al. 2010, 2011; Zeigler et al. 2013).

Further constraints for the provenance of Shişr 161 can be deduced from its petrography. First, basalt is not a significant component. This inference derives from the bulk rock chemistry (Korotev 2012) and the lack of any basaltic clasts >~0.5 mm in size. Therefore, impact basins that contain substantial mare-infill are unlikely source craters for Shişr 161, of course given the caveat that the impact that excavated the cumulate melt sheet and crystallized melt rocks in Shişr 161 may have happened before its parent basin was flooded with mare lava. Then, because ballistic sedimentation excessively dilutes the more distal portions of the continuous ejecta blankets of complex impact craters (Oberbeck 1975; Oberbeck et al. 1975; Morrison and Oberbeck 1978; Hörz et al. 1983), the cumulate clast assemblage in Shişr 161 likely indicates deposition in the proximal ejecta blanket of a >>15 km crater that formed on the impact melt sheet of a 300–500 km impact basin in the feldspathic highlands. Therefore, the provenance of Shişr 161 – if this breccia represents a petrogenetically linked mixture of impact melt rocks sourced from a 300 to 500 km lunar impact basin – would likely be in or very near to that basin.

Currently, 28 impact basins with rim diameters between 300 and 500 km are known on the Moon (Wilhelms et al. 1987; Cook et al. 2002; Wood 2004). Of these, only Riemann-Fabry basin lies close to a 5°-region on the lunar surface that compositionally matches Shişr 161.

Centered at 41N, 99E (Cook et al. 2002) on the Moon's western farside, pre-Nectarian Riemann-Fabry basin is heavily degraded (Fig. 24a–b). About 50% of its area is occupied by 184 km Ø Fabry crater (centered at 43N, 101E; Bussey and Spudis 2004) in the NE quadrant of Riemann-Fabry basin and 237 km Ø Harkhebi crater (centered at 38N 98E; Bussey and Spudis 2004) near the center. The 163 km Ø Riemann crater (centered at 40N 87E; Bussey and Spudis 2004) lies to the SW. Fabry crater likely excavated large portions of the (cumulate?) melt sheet of Riemann-Fabry basin and could have deposited ejecta at the compositionally matching surface unit to Shişr 161 on the Moon's western farside. However, Riemann-Fabry basin has so far only been proposed as a possible degraded basin based on a Clementine stereo digital terrain model (Cook et al. 2002); its existence could not be confirmed by analysis of the digital terrain model derived from the wide-angle camera of the Lunar Reconnaissance Orbiter (Oberst et al. 2011). Also, it is unclear, if 237 km diameter Harkhebi crater that partly underlies Fabry crater is a separate feature or corresponds to the central part of Riemann-Fabry basin as defined by Cook et al. (2002). A comparison with the gravity model that is based on GRAIL mission data (Zuber et al. 2013; Fig. 24c) is also inconclusive, although the projected 237 km diameter of Harkhebi crater appears too small for the gravity deficiency associated with this structure. Yamamoto et al. (2012) report spectroscopic identification of "purest anorthosite" on the rim of Harkhebi crater / Riemann-Fabry basin at 36.3N, 102.4E (Fig. 24b), close to Giordano Bruno crater and the compositionally matching surface unit with Shişr 161. However, we found that none of the clasts >0.5 mm$^2$ in Shişr 161 are "purest anorthosite" composed of >98 % plagioclase and none of these clasts could conceivably represent pristine lunar plutonic rocks according to the definitions summarized by Warren (1993).

## Implications

Our quantitative characterization of clast components in a lunar regolith breccia meteorite allows the formulation of a hypothesis of its petrogenesis. We suggest that the magnesian cumulate clasts in Shişr 161 and similar lithologies in meteorites and Apollo samples are recorders of the lunar basin-forming eon that concluded with the formation of Orientale basin ca. 3.8 Ga ago (Wilhelms et al. 1987). The textural, compositional and petrologic evidence that characterizes these clasts in Shişr 161 may also apply to some lunar poikilitic granulite rocks (Lindstrom and Lindstrom 1986; Cushing et al. 1999; Norman and Nemchin 2014). Consequently, some of the anomalously magnesium-rich rocks of the lunar highlands that are currently regarded as metamorphic rocks (Korotev and Jolliff 2001; Treiman et al. 2010) could instead be impact melt rocks that contain mantle components.

Our hypothesis for the impact melt clast assemblage in Shişr 161 suggests it could represent ejecta from one of the ~45 lunar impact basins >300 km in diameter. We found that the region around possible Riemann-Fabry basin best matches petrological, and chemical constraints from the composition of Shişr 161, its clast components, and the comparison with the composition of the lunar surface. However, Riemann-Fabry basin needs to be confirmed as a basin, and not a mere superposition of Fabry crater on larger Harkhebi crater. Further tests for the petrogenesis of Shişr 161 require radioisotopic age dating of cumulate clasts that would test the hypothesis of an origin in a pre-Nectarian lunar impact basin in the Moon's feldspathic highlands. Ultimately, the identification of such impact basin rock samples can unravel the inner solar system's collisional history until ~3.8 Ga ago.

## ACKNOWLEDGMENTS

Andrew Foreman and Ryan Zeigler (Washington University in St. Louis and NASA Johnson Space Center, Houston) for preliminary data, David Kring (Lunar and Planetary Institute), and Timothy Swindle (Lunar and Planetary Laboratory) for related work on Shişr 161, Barry Shaulis (University of Houston) for assistance with the LA-ICP-MS work, Paul Carpenter for assistance with the EMPA work, Joshua Snape (Open University, Milton Keynes) and Vera Fernandes (Museum für Naturkunde, Berlin) for their helpful reviews, and associate editor Rachel Klima for handling the manuscript. We gratefully acknowledge funding by the NASA Cosmochemistry and LASER programs for this study.

## REFERENCES CITED

Afiattalab, F., and Wasson, J.T. (1980) Composition of the metal phases in ordinary chondrites: implications regarding classification and metamorphism. Geochimica et Cosmochimica Acta, 44, 431–446.

Ames, D.E., Golightly, J.P., Lightfoot, P.C., and Gibson, H.L. (2002) Vitric compositions in the Onaping formation and their relationship to the Sudbury igneous complex, Sudbury structure. Economic Geology, 97, 1541–1562.

Anders, E., and Grevesse, N. (1989) Abundance of the elements: Meteoritic and solar. Geochimica et Cosmochimica Acta, 53, 197–214.

Andersen, D.J., Lindsley, D.H., and Davidson, P.M. (1993) QUILF: A Pascal program to assess equilibria among Fe-Mg-Mn-Ti oxides, pyroxenes, olivine, and quartz.

 

Computers and Geosciences, 19, 1333–1350.

Ashwal, L.D. (1975) Petrologic evidence for a plutonic igneous origin of anorthositic norite clasts in 67955 and 77017. Proceedings of the Lunar Science Conference, 6, p. 221–230. Pergamon Press, Inc., New York, Houston, TX.

Axon, H.J., and Goldstein, J.I. (1973) Metallic particles of high cobalt content in Apollo 15 soil samples. Earth and Planetary Science Letters, 18, 173–180.

Berlin, J. (2009) Mineralogy and bulk chemistry of chondrules and matrix in petrologic Type 3 chondrites: Implications for early solar system processes. Earth and Planetary Sciences, p. 217. University of New Mexico, Albuquerque. (PhD Thesis).

Bussey, B., and Spudis, P.D. (2004) The Clementine Atlas of the Moon. 380 p. Cambridge University Press, Cambridge.

Carter, J.L., Clanton, U.S., Fuhrman, R., Laughon, R.B., McKay, D.S., and Usselman, T.M. (1975) Morphology and composition of chalcopyrite, chromite, Cu, Ni-Fe, pentlandite, and troilite in vugs of 76015 and 76215. Proceedings of the Lunar Science Conference, 6, p. 719–728. Pergamon Press, Inc., New York.

Cintala, M.J., and Grieve, R.A.F. (1998a) Scaling impact melting and crater dimensions: Implications for the lunar cratering record. Meteoritics and Planetary Science, 33, 889–912.

Cintala, M.J., and Grieve, R.A.F. (1998b) Scaling impact melting and crater dimensions: Implications for the lunar cratering record - Errata. Meteoritics and Planetary Science, 33, 1343.

Clarke, R.S.J., and Scott, E.R.D. (1980) Tetrataenite-ordered FeNi, a new mineral in meteorites. American Mineralogist, 65, 624–630.

Cook, A.C., Spudis, P.D., Robinson, M.S., and Watters, T.R. (2002) Lunar Topography and Basins Mapped Using a Clementine Stereo Digital Elevation Model. Lunar and Planetary Science Conference, 33, abstract #1281. Lunar and Planetary Institute, Houston, TX.

Cushing, J.A., Taylor, G.J., Norman, M.D., and Keil, K. (1999) The granulitic impactite suite: Impact melts and metamorphic breccias of the early lunar crust. Meteoritics and Planetary Science, 34(2), 185–195.

Delano, J.W. (1986) Lunar volcanic glasses and their constraints on mare petrogenesis. Proceedings of the Lunar and Planetary Science Conference, 16, D201-D213.

Deutsch, A., and Stöffler, D. (1987) Rb-Sr-analyses of Apollo 16 melt rocks and a new age estimate for the Imbrium basin: Lunar basin chronology and the early heavy bombardment of the moon. Geochimica et Cosmochimica Acta, 51, 1951–1964.

Deutsch, A. (1994) Isotope systematics support the impact origin of the Sudbury structure (Ontario, Canada). In B.O. Dressler, R.A.F. Grieve, and V.L. Sharpton, Eds. Large Meteorite Impact and Planetary Evolution, 293, p. 289–302. Geological Society of America, Boulder, Colorado.

Dymek, R.F., Albee, A.L., and Chodos, A.A. (1975) Comparative petrology of lunar cumulate rocks of possible primary origin - Dunite 72415, troctolite 76535, norite 78235, and anorthosite 62237. Proceedings of the Lunar Science Conference, 6, p. 301–341. Pergamon Press, Inc., New York.

Foreman, A.B., Korotev, R.L., Zeigler, R.A., Wittmann, A., Kring, D.A., Irving, A.J., and Kuehner, S.M. (2009) Petrographic and geochemical analysis of feldspathic lunar meteorite Shişr 161. Lunar and Planetary Science Conference, 40, abstract #2304. Lunar and Planetary Institute, Houston, TX.

Fruland, R.M., Morris, R.V., McKay, D.S., and Clanton, U.S. (1977) Apollo 17 ropy glasses. Proceedings of the Lunar Science Conference, 8, p. 3095–3111. Pergamon Press, Inc.

Gast, P.W., Phinney, W.C., Duke, M.B. and 51 co-authors (1973) Apollo 17 lunar samples: Chemical and petrographic description. Science, 182, 659–672.

Ghiorso, M.S., and Sack, R.O. (1995) Chemical mass transfer in magmatic processes. IV. A revised and internally consistent thermodynamic model for the interpolation and extrapolation of liquid-solid equilibria in magmatic systems at elevated temperatures and pressures. Contributions to Mineralogy and Petrology, 119, 197–212.

Goderis, S., Wittmann, A., Zaiss, J., Elburg, M., Ravizza, G., Vanhaecke, F., Deutsch, A., and Claeys, P. (2013) Testing the ureilite projectile hypothesis for the El'gygytgyn impact: Determination of siderophile element abundances and Os isotope ratios in ICDP drill core samples and melt rocks. Meteoritics and Planetary Science, 48, 1296–1324.

Goldstein, J.I., and Yakowitz, H. (1971) Metallic inclusions and metal particles in the Apollo 12 lunar soil. Proceedings of the Lunar Science Conference, 1, p. 177–191. M.I.T. Press, Cambridge.

Grieve, R.A.F. (1975) Petrology and chemistry of the impact melt at Mistastin Lake crater, Labrador. Geological Society of America Bulletin, 86, 1617–1629.

Grieve, R.A.F., Stöffler, D., and Deutsch, A. (1991) The Sudbury structure: Controversial or misunderstood? Journal of Geophysical Research, 96(E5), 22753–22764.

Grieve, R.A.F. (2006) Impact structures in Canada. 210 p. Geological Association of Canada, St. John.

Grieve, R.A.F., Ames, D.E., Morgan, J.V., and Artemieva, N.A. (2010) The evolution of the Onaping formation at the Sudbury impact structure. Meteoritics and Planetary Science, 45(5), 759–782.

Hawke, B.R., Peterson, C.A., Blewett, D.T., Bussey, D.B.J., Lucey, P.G., Taylor, G.J., and Spudis, P.D. (2003) Distribution and modes of occurrence of lunar anorthosite. Journal of Geophysical Research Planets, 108(E6).

Heiken, G.H., McKay, D.S., and Brown, R.W. (1974) Lunar deposits of possible pyroclastic origin. Geochimica et Cosmochimica Acta, 38, 1703–1718.

Hess, P.C. (1994) Petrogenesis of lunar troctolites. Journal of Geophysical Research, 99(E9), 19083–19093.

Hollister, L.S. (1973) Sample 67955: A description and a problem. Proceedings of the Lunar Science Conference, 4, p. 633–641.

Hörz, F., Ostertag, R., and Rainey, D.A. (1983) Bunte breccia of the Ries: continuous deposits of large impact craters. Reviews in Geophysics and Space Physics, 21, 1667–1725.

Irvine, T.N. (1982) Terminology for layered intrusions. Journal of Petrology, 23, 127–162.

James, O.B., and Flohr, M.K. (1983) Subdivision of the Mg-suite noritic rocks into Mg-gabbronorites and Mg-norites. Proceedings of the Thirteenth Lunar and Planetary Science Conference, Supplement, Journal of Geophysical Research, 88, A603–

A614.

Jolliff, B.L., Gillis, J.J., Haskin, L.A., Korotev, R.L., and Wieczorek, M.A. (2000) Major lunar crustal terranes: Surface expressions and crust-mantle origins. Journal of Geophysical Research, 105(E2), 4197–4216.

Jolliff, B.L., Korotev, R.L., Zeigler, R.A., and Prettyman, T.H. (2009) Connecting lunar meteorite Dhofar 961 to the South Pole-Aitken Basin through Lunar Prospector gamma-ray data. Lunar and Planetary Science Conference, 40, abstract #2555. Lunar and Planetary Institute, Houston, TX.

Joy, K.H., Crawford, I.A., Russell, S.S., and Kearsley, A.T. (2010) Lunar meteorite regolith breccias: An in situ study of impact melt composition using LA-ICP-MS with implications for the composition of the lunar crust. Meteoritics and Planetary Science, 45, 917–946.

Joy, K.H., Burgess, R., Hinton, R., Fernandes, V.A., Crawford, I.A., Kearsley, A.T., Irving, A.J., and EIMF. (2011) Petrogenesis and chronology of lunar meteorite Northwest Africa 4472: A KREEPy regolith breccia from the Moon. Geochimica et Cosmochimica Acta, 75, 2420–2452.

Kieffer, S.W., and Simonds, C.H. (1980) The role of volatiles and lithology in the impact cratering process. Review of Geophysics and Space Physics, 18, 143–181.

Koeberl, C., Brandstätter, F., Glass, B.P., Hecht, L., Mader, D., and Reimold, W.U. (2007) Uppermost impact fallback layer in the Bosumtwi crater (Ghana): Mineralogy, geochemistry, and comparison with Ivory Coast tektites. Meteoritics and Planetary Science, 42, 709–729.

Korotev, R.L. (2012) Lunar meteorites from Oman. Meteoritics and Planetary Science, 47(8), 1365–1402.

Korotev, R.L., and Jolliff, B.L. (2001) The curious case of the lunar magnesian granulitic breccias. Lunar and Planetary Science Conference, 32, abstract #1455. Lunar and Planetary Institute, Houston, TX.

Korotev, R.L., Jolliff, B.L., Zeigler, R.A., Gillis, J.J., and Haskin, L.A. (2003) Feldspathic lunar meteorites and their implications for compositional remote sensing of the lunar surface and the composition of the lunar crust. Geochimica et Cosmochimica Acta, 67(24), 4895–4923.

Korotev, R. L., Zeigler, R. A., and Jolliff, B. L. (2006) Feldspathic lunar meteorites Pecora Escarpment 02007 and Dhofar 489: Contamination of the surface of the lunar highlands by post-basin impacts. Geochimica et Cosmochimica Acta, 70, 5935–5956.

Kuehner, S.M., Irving, A.J., Rumble, D., III, Hupé, A.C., and Hupé, G.M. (2005) Mineralogy and petrology of lunar meteorite NWA 3136: A glass-welded mare regolith breccia of mixed heritage. Lunar and Planetary Science Conference, 36, p. abstract #1228. Lunar and Planetary Institute, Houston, TX.

Laul, J.C., and Schmitt, R.A. (1975) Dunite 72417: A chemical study and interpretation. Proceedings of the Lunar and Planetary Science Conference, 6, 1231–1254.

Lindstrom, M.M., and Lindstrom, D.J. (1986) Lunar granulites and their precursor anorthositic norites of the early lunar crust. Journal of Geophysical Research, 91(B4), D263–D276.

Lucey, P., Korotev, R.L., Gillis, J.J., Taylor, L.A., Lawrence, D., Campbell, B.A., Elphic, R., Feldman, B., Hood, L.L., Hunten, D., Mendillo, M., Noble, S., Papike, J.J., Reedy, R.C., Lawson, S., Prettyman, T., Gasnault, O., and Maurice, S. (2006) Understanding the lunar surface and space-Moon interactions. In B.L. Jolliff, M.A. Wieczorek, C.K. Shearer, and C.R. Neal, Eds. New Views of the Moon, Reviews in Mineralogy and Geochemistry 60, p. 83–219. Mineralogical Society of America, Washington, DC.

Marsh, B.D. (1981) On the crystallinity, probability of occurrence, and rheology of lava and magma. Contributions to Mineralogy and Petrology, 78, 85–98.

Marvin, U.B., and Warren, P.H. (1980) A pristine eucritic gabbro from Descartes and its exotic kindred. Proceedings of the Lunar and Planetary Science Conference, 11, 507–521.

McKay, D.S., and Basu, A. (1983) The production curve for agglutinates in planetary regoliths. Proceedings of the Fourteenth Lunar and Planetary Science Conference, Supplement, Journal of Geophysical Research, 88, B193–B199.

McKay, D.S., Bogard, D.D., Morris, R.V., Korotev, R.L., Johnson, P., and Wentworth, S.J. (1986) Apollo 16 regolith breccias: Characterization and evidence for early formation in the mega-regolith. Proceedings of the Sixteenth Lunar and Planetary Science Conference, part 2, Journal of Geophysical Research, 91(B4), D277–D303.

Melosh, H.J. (1989) Impact Cratering: A geological process. 245 p. Oxford University Press, New York.

Melosh, H.J., Freed, A.M., Johnson, B.C., Blair, D.M., Andrews-Hanna, J.C., Neumann, G.A., Phillips, R.J., Smith, D.E., Solomon, S.C., Wieczorek, M.A., and Zuber, M.T. (2013) The Origin of Lunar Mascon Basins. Science, 340, 1552-1555.

Morrison, R.H., and Oberbeck, V.R. (1978) A composition and thickness model for lunar impact crater and basin deposits. Lunar and Planetary Science Conference, 9, 3763–3785. Pergamon Press, Inc., New York.

Morrison, D.A. (1998) Did a thick South Pole-Aitken Basin melt sheet differentiate to form cumulates? Lunar and Planetary Science Conference, 29, abstract #1657. Lunar and Planetary Institute, Houston, TX.

Nazarov, M.A., Tarasov, L.S., and Shevaleevsky, I.D. (1980) The occurrence of pentlandite and the geochemistry of Ni in Luna 24 basalts. Lunar and Planetary Science Conference, 9, p. 800–802, abstract. Lunar and Planetary Institute, Houston, TX.

Norman, M.D., and Ryder, G. (1980) Geochemical constraints on the igneous evolution of the lunar crust. Proceedings of the Lunar and Planetary Science Conference, 11, 317–331.

Norman, M.D., and Nemchin, A.A. (2014) A 4.2 billion year old impact basin on the Moon: U-Pb dating of zirconolite and apatite in lunar melt rock 67955. Earth and Planetary Science Letters, 388, 387-398.

Oberbeck, V.R. (1975) The role of ballistic erosion and sedimentation in lunar stratigraphy. Reviews in Geophysics and Space Physics, 13, 337–362.

Oberbeck, V.R., Morrison, R.H., and Hörz, F. (1975) Transport and emplacement of crater and basin deposits. The Moon, 13, 9–26.

Oberst, J., Unbekannt, H., Scholten, F., Haase, I., Hiesinger, H., and Robinson, M. (2011) A search for degraded lunar basins using the LROC-WAC digital terrain model (GLD100). Lunar and Planetary Science Conference, 42, abstract #1992. Lunar and Planetary Institute, Houston, TX.

Papike, J.J., Ryder, G., and Shearer, C.K. (1998) Lunar Samples. In J.J. Papike, Ed. Planetary Materials, 36, p. 234. Mineralogical Society of America, Washington, DC.

Papike, J.J. (1998) Comparative planetary mineralogy: Chemistry of melt-derived pyroxene, feldspar, and olivine. In J.J. Papike, Ed. Planetary Materials, 36, p. 11 (chapter 7). Mineralogical Society of America, Washington, DC.

Petro, N.E., and Pieters, C.M. (2008) The lunar-wide effects of basin ejecta distribution on the early megaregolith. Meteoritics and Planetary Science, 43, 1517–1529.

Potter, R.W.K., Kring, D.A., Collins, G.S., Kiefer, W.S., and McGovern, P.J. (2013) Numerical modeling of the formation and structure of the Orientale impact basin. Journal of Geophysical Research, 118, 963-979.

Prettyman, T.H., Hagerty, J.J., Elphic, R.C., Feldman, W.C., Lawrence, D.J., McKinney, G.W., and Vaniman, D.T. (2006) Elemental composition of the lunar surface: Analysis of gamma ray spectroscopy data from Lunar Prospector. Journal of Geophysical Research, 111, E12007.

Ramdohr, P. (1972) Lunar pentlandite and sulfidization reactions in microbreccia 14315,9. Earth and Planetary Science Letters, 5, 113–115.

Robinson, M.S., Brylow, S.M., Tschimmel, M., Humm, D., Lawrence, S.J., Thomas, P.C., Denevi, B.W., Bowman-Cisneros, E., Zerr, J., Ravine, M.A., Caplinger, M.A., Ghaemi, F.T., Schaffner, J.A., Malin, M.C., Mahanti, P., Bartels, A., Anderson, J., Tran, T.N., Eliason, E.M., McEwen, A.S., Turtle, E., Jolliff, B.L., and Hiesinger, H. (2010) Lunar Reconnaissance Orbiter Camera (LROC)

Instrument Overview, Space Science Reviews, 150, 81-124.

Reid, A.M., Meyer Jr., C., Harmon, R.S., and Brett, R. (1970) Metal grains in Apollo 12 rocks. Earth and Planetary Science Letters, 9, 1–5.

Ryder, G., Norman, M.D., and Score, R.A. (1980) The distinction of pristine from meteorite-contaminated highlands rocks using metal compositions. Proceedings of the Lunar and Planetary Science Conference, 11, 471–479.

Settle, M. (1980) The role of fallback ejecta in the modification of impact craters. Icarus, 42, 1-19.

Shearer, C.K., and Papike, J.J. (2005) Early crustal building processes on the Moon: Models for the petrogenesis of the magnesian suite. Geochimica et Cosmochimica Acta, 69, 3445–3461.

Simonds, C.H., Warner, J.L., and Phinney, W.C. (1976) Thermal regimes in cratered terrain with emphasis on the role of impact melt. American Mineralogist, 61, 569–577.

Stöffler, D., Knöll, H.-D., Marvin, U.B., Simonds, C.H., and Warren, P.H. (1980) Recommended classification and nomenclature of lunar highland rocks - a committee report. In J.J. Papike, and R.B. Merrill, Eds. Conference on the Lunar Highlands Crust, p. 51–70. New York and Oxford, Pergamon Press, Houston.

Taylor, S.R., Gorton, M.P., Muir, P., Nance, W.B., Rudowski, R., and Ware, N. (1973) Composition of the Descartes region, lunar highlands. Geochimica et Cosmochimica Acta, 37, 2665–2683.

Therriault, A.M., Fowler, A.D., and Grieve, R.A.F. (2002) The Sudbury Igneous Complex: A differentiated impact melt sheet. Economic Geology, 97, 1521–1540.

Treiman, A.H., Maloy, A.K., Shearer, C.K., and Gross, J. (2010) Magnesian anorthositic granulites in lunar meteorites Allan Hills A81005 and Dhofar 309: Geochemistry and global significance. Meteoritics and Planetary Science, 45, 163–180.

Vaughan, W.M., Head, J.W., Wilson, L., and Hess, P.C. (2013) Geology and petrology of enormous volumes of impact melt on the Moon: A case study of the Orientale basin impact melt sea. Icarus, 223, 749–765.

Warren, P.H., and Wasson, J.T. (1979) The compositional-petrographic search for pristine nonmare rocks: Third foray. Proceedings of the Lunar and Planetary Science Conference, 10, 583–610.

Warren, P.H. (1985) The magma ocean concept and lunar evolution. Annual Review of Earth and Planetary Sciences, 13, 201–240.

Warren, P.H. (1986) Anorthosite assimilation and the origin of the Mg/Fe-related bimodality of pristine Moon rocks: Support for the magmasphere hypothesis. Proceedings of the Lunar and Planetary Science Conference, 16, D331–D343.

Warren, P.H. (1990) Lunar anorthosites and the magma-ocean plagioclase-flotation hypothesis: Importance of FeO enrichment in the parent magma. American Mineralogist, 75, 46–58.

Warren, P.H. (1993) A concise compilation of petrologic information on possibly pristine nonmare Moon rocks. American Mineralogist, 78, 360–376.

Warren, P.H., Claeys, P., and Cedillo-Pardo, E. (1996) Mega-impact melt petrology (Chicxulub, Sudbury, and the Moon): Effects of scale and other factors on potential for fractional crystallization and development of cumulates. In G. Ryder, and D. Fastovsky, Eds. The Cretaceous-Tertiary Event and other Catastrophes in

Earth History, 307, p. 105–124. Geological Society of America, Boulder, Colorado.

Warren, P.H. (2008) Lunar rock-rain: Diverse silicate impact-vapor condensates in an Apollo-14 regolith breccia. Geochimica et Cosmochimica Acta, 72, 3562–3585.

Wood, C.A. (2004) Impact basin database: http://www.lpod.org/cwm/DataStuff/Lunar%20Basins.htm last accessed Dec. 6, 2013.

Wieczorek, M.A., Jolliff, B.L., Khan, A., Pritchard, M.E., Weiss, B.P., Williams, J.G., Hood, L.L., Righter, K., Neal, C.R., Shearer, C.K., McCallum, I.S., Tompkins, S., Hawke, B.R., Peterson, C., Gillis, J.J., and Bussey, B. (2006) The constitution and structure of the lunar interior. In B.L. Jolliff, M.A. Wieczorek, C.K. Shearer, and C.R. Neal, Eds. New Views of the Moon, 60, p. 221–364. Mineralogical Society of America, Washington, DC.

Wieczorek, M.A., Neumann, G.A., Nimmo, F., Kiefer, W.S., Taylor, G.J., Melosh, H.J., Phillips, R.J., Solomon, S.C., Andrews-Hanna, J.C., Asmar, S.W., Konopliv, A.S., Lemoine, F.G., Smith, D.E., Watkins, M.W., Williams, J.G., and Zuber, M.T. (2013) The Crust of the Moon as Seen by GRAIL. Science, 339, 671–675.

Wilhelms, D.E., McCauley, J.F., and Trask, N.J. (1987) The Geologic History of the Moon. USGS Professional Paper, 1348, 302.

Wittmann, A., Goderis, S., Claeys, P., Vanhaecke, F., Deutsch, A., and Adolph, L. (2013) Petrology of impactites from El'gygytgyn crater: Breccias in ICDP-drill core 1C, glassy impact melt rocks and spherules. Meteoritics and Planetary Science, 48, 1199–1235.

Yamamoto, S., Nakamura, R., Matsunaga, T., Ogawa, Y., Ishihara, Y., Morota, T., Hirata, N., Ohtake, M., Hiroi, T., Yokota, Y., and Haruyama, J. (2012) Massive layer of pure anorthosite on the Moon. Geophysical Research Letters, 39, L13201.

Zeigler, R.A., Jolliff, B.L., and Korotev, R.L. (2013) Lunar Meteorites Sayh al Uhaymir 449 and Dhofar 925, 960, and 961: Windows into South Pole Aitken Basin? Lunar and Planetary Science Conference, 44, p. abstract #2437. Lunar and Planetary Institute, Houston, TX.

Zieg, M.J., and Marsh, B.D. (2005) The Sudbury Igneous Complex: Viscous emulsion differentiation of a superheated impact melt sheet. Geological Society of America Bulletin, 117, 1427–1450.

Zuber, M.T., Smith, D.E., Watkins, M.W., Asmar, S.W., Konopliv, A.S., Lemoine, F.G., Melosh, H.J., Neumann, G.A., Phillips, R.J., Solomon, S.C., Wieczorek, M.A., Williams, J.G., Goossens, S.J., Kruizinga, G., Mazarico, E., Park, R.S., and Yuan, D.-N. (2013) Gravity field of the Moon from the Gravity Recovery and Interior Laboratory (GRAIL) mission. Science, 339, 668–671.

## LIST OF FIGURE CAPTIONS

Figure 1 (a) – (b). Shişr 161 specimen photographs. (Courtesy of P. Mani and G. Hupé). Cube with 1 cm long sides for scale.

Figure 2. Shişr 161 thin section. Back-scattered electron (BSE) image with white outlines of 91 clasts characterized in this study; the prefix g indicates holohyaline glass clasts, the prefix s indicates spherules.

Figure 3. Spherules in Shişr 161. BSE images. (a) Spherule 9, a cryptocrystalline spherule with a composition similar to gas-associated spheroidal precipitates (Warren 2008); (b) vitrophyre spherule 1, note troilite and FeNi metal particles concentrated near the rim; (c) crystallized spherule 3, note diffuse troilite and FeNi metal particles near the rim; (d) vitrophyre spherule 2 with ferroan olivine crystals in a hyalophitic groundmass and accreted feldspathic vitrophyre debris (arrow); (e) hyalophitic spherule 7 with assimilated xenolith crystals and mesostasis domains enriched in incompatible elements; (f) anorthositic troctolite clast that has a spherule inclusion with an ophitic texture (white dotted outline indicates spherule).

Figure 4. Typical crystal size variations of major mineral components in Shişr 161 clast lithologies (excluding clasts that did not undergo impact-induced melting or recrystallization). Crosses mark estimated average grain sizes.

Figure 5. Cumulate clasts.

(a) plane polarized light (ppl) micrograph of glass coated magnesian cumulate clast 54 with cumulus plagioclase (white) and olivine (orange), and grey intercumulus pyroxene;
(b) BSE image of subhedral cumulate plagioclase (pl) and olivine (ol) and intercumulus oikocrysts of augite (cpx) and orthopyroxene (opx) in magnesian cumulate clast 5;
(c) cathodoluminescence false-color image of magnesian cumulate clast 34 showing concentric igneous zoning in cumulate plagioclase (arrows); note that mafic silicates are non-luminescent.

Figure 6. BSE images of crystallized melt clasts.

(a) Subophitic texture of tabular plagioclase (pl) with interstitial pyroxene (px) and olivine (ol) and minor troilite, ilmenite, and chromite (brightest phases) in clast 18.
(b) Poikilitic texture of pyroxene and olivine oikocrysts that incorporate chadacrysts of plagioclase, troilite and FeNi metal (brightest phases) in clast 8;
(c) Intergranular texture of subhedral plagioclase, olivine and pyroxene of clast 43;
(d) Granular texture of anhedral plagioclase and euhedral pyroxene and olivine in clast 118; note large plagioclase xenocryst in lower left corner.
(e) Coalescent texture of anhedral maskelynite, pyroxene and olivine in clast 63.
(f) Variolitic texture of plagioclase intergrown with zoned, skeletal pyroxene in clast 23; note domains of tiny FeS and fayalitic olivine crystals (arrow).

Figure 7. Vitrophyres.

(a) Angular, hyalophitic clast 11, ppl image;

(b) BSE image of clast 11 shows tabular plagioclase with interstitial mesostasis that contains quenched crystals of chain-link pyroxene and skeletal olivine.

(c) Clast 33 has a hyalophitic texture of flow-aligned plagioclase crystals in a melt mesostasis that engulfs coarse grained (possible) basalt clasts (B), BSE image;

(d) BSE image of ropy glass clast 37 that has an ameboid shape and accreted fine debris.

(e) BSE image of ameboid, inhomogeneous, clast-rich glass clast 13 that contains abundant FeS-FeNi inclusions (brightest phases).

(f) BSE image of hyalophitic shard glass 1.

Figure 8. Polymict breccia clast 1.

Dotted white line approximates limits of the clast in this ppl image; A indicates cataclastic anorthosite sub-clast.

Figure 9. Shişr 161 plagioclase per electron microprobe analysis.

Histogram of anorthite numbers of plagioclase crystals. Note that three data points at An 67 and 75 are not shown. For details of lithological contexts, see text.

Figure 10. Shişr 161 olivine per electron microprobe analysis.

Histogram of mol% Mg/(Mg+Fe) of olivine crystals.

Figure 11. Molar Fe versus Mn for olivine in planetary melt rocks.

Electron microprobe analyses of Shişr 161 olivine with approximate trendlines redrawn after Papike (1998).

Figure 12. Shişr 161 pyroxene per electron microprobe analysis.
Quadrilateral of enstatite, ferrosilite and wollastonite components of pyroxene. Average values for our repeat analyses on pyroxene crystals in mono- and polymineralic clasts are displayed.

Figure 13. Molar Fe versus Mn for pyroxene in planetary melt rocks.
Electron microprobe analyses of Shişr 161 pyroxene with approximate trendlines redrawn after Papike (1998).

Figure 14. Compositions of spinel in Shişr 161.
(a) Iron number versus chromium number, data for cumulate clast spinel, same symbols as in (b);
(b) Iron number versus titanium number.

Figure 15. Compositions of FeNi metal particles in Shişr 161.
Field for metal particles in pristine dunite 72415/17 after Dymek et al. (1975) and Ryder et al. (1980); field for “probably pristine” troctolite clast 73235,136 after Warren and Wasson (1979); field for “high cobalt α and γ structures in Apollo 15 soils” after Axon and Goldstein (1973); fields for Apollo 17 basalts and Apollo polymict rocks (”range of metal compositions in most polymict rocks”) after Ryder et al. (1980); “meteoritic” field

 

after Goldstein and Yakowitz (1971), range of Apollo 12 olivine basalts after Reid et al. (1970).

Figure 16. Normative mineralogies of Shişr 161 clasts.

Rock designations after the classification scheme for lunar highlands rocks of Stöffler et al. (1980); average composition of the lunar crust from Korotev et al. (2003); bulk composition of Shişr 161 from Korotev (2012); symbol sizes reflect the sizes of the clasts they represent: The smallest symbols represent clasts <0.5 $mm^2$, medium symbols clasts 0.5–1 $mm^2$, and large symbols clasts >1 $mm^2$.

Figure 17. $Al_2O_3$ vs. magnesium number of Shişr 161 clasts.

Reconstructed bulk compositions of clasts in $Al_2O_3$ versus Mg/(Mg+Fe) space. Clast sizes correspond to the relative sizes of clasts. Smallest symbols represent clasts <0.5 $mm^2$, medium symbols clasts 0.5–1 $mm^2$, and large symbols clasts >1 $mm^2$. Diagram modified after Korotev et al. (2003), fields for pristine troctolites, norites, dunite, KREEP basalts and gabbronorites after Warren (1985), bulk composition of Shişr 161 from Korotev (2012), feldspathic upper crust after Korotev et al. (2003). The field for feldspathic meteorites has been updated with the currently available data for feldspathic meteorites.

Figure 18. Diagram modified after Figure 2.5 of Lucey et al. (2006).

Feldspathic upper crust after Korotev et al. (2003); bulk Shişr 161 composition after Korotev (2012); average CI-chondrite composition after Anders and Grevesse (1989).

Figure 19. Rare Earth Element patterns.
CI normalized (Anders and Grevesse 1989) Rare Earth Element (REE) patterns for bulk clasts in Shişr 161 compared to literature values for Apollo magnesian suite rocks and ferroan anorthosites (Papike et al. 1998 and references therein), dunite 72417 (Laul and Schmitt 1975) and the feldspathic upper crust (FC; Korotev et al. 2003).

Figure 20. Normative plagioclase and $Al_2O_3$ content in Shişr 161 clast components compared to the model mineralogy of the lunar crust after Wieczorek et al. (2006) and the bulk rock composition of Shişr 161 (Korotev (2012); [a]all 38 clasts >0.5 mm, excluding a polymict breccia and a variolitic melt clast; [b]normative plagioclase content from bulk rock composition (Korotev 2012).

Figure 21. Shişr 161 impact melts in the fractionation index diagrams after Norman and Ryder (1980).
a) Ti/Sm is sensitive to the fractionation of ilmenite, and b) Sc/Sm indicates pyroxene fractionation in pristine lunar rocks. These diagrams distinguish pristine Mg-suite rocks from primary products of magma ocean fractionation. CI-chondrite after Anders and Grevesse (1989), Mg gabbronorites 67667, 73255,27,45, 61224 after James and Flohr (1983); dunite 74215/7 after Laul and Schmitt (1975) and Dymek et al. (1975). Feldspathic upper crust (FC) after Korotev et al. (2003); same legend for both diagrams.

 

Figure 22. Results of MELTS modeling of the fractional crystallization of an impact melt composed of 90 % feldspathic upper crust (Korotev et al. 2003) and 10 % dunite 72415 (Papike et al. 1998) at an oxygen fugacity buffer of iron-wüstite and a pressure of 50 bar (~1 km depth on the Moon).

The crystallization sequence of mineral phases is characterized by four stages that are labeled with the rock type that would be constituted by the crystallized mineral phases. Note that at 1240 °C, >50 g neutrally buoyant plagioclase has crystallized, which suggests fractional crystallization ceases.

Figure 23. Impact basin impactite stratigraphy.

Schematic comparison of impactite lithologies between observed conditions at the Sudbury basin, modified after Grieve (2006), with petrologic constraints for lunar impactites (see text).

Figure 24. Provenance of Shişr 161 on the Moon.

Lunar Reconnaissance Orbiter wide-angle camera image mosaic (NASA/GSFC/ASU-ACT-REACT QuickMap; Robinson et al. 2010) showing the global morphology of the lunar surface. White outlines show the approximate traces of the outer rims of 26 impact basins between 300 and 500 km in diameter (Wilhelms et al. 1987; Cook et al. 2002; Bussey and Spudis 2004). White squares indicate matches of the bulk composition of Shişr 161 with Lunar Prospector gamma-ray spectrometer data, no matches occur in polar regions >75°N or >75°S.

b) Lunar Reconnaissance Orbiter wide-angle camera image (Robinson et al. 2010) of the Riemann-Fabry basin region that is indicated as a black rectangle in a); dotted lines trace the approximate positions of craters: RF – 320 km Ø Riemann-Fabry basin; F – 174 km Ø Fabry crater; H – 237 km Ø Harkhebi crater; R – 163 km Ø Riemann crater, GB – 22 km Ø Giordano Bruno crater; black rectangle indicates approximate position of 5° Lunar Prospector gamma ray spectrometer region that matches the bulk composition of Shişr 161; PAN - spectroscopically pure anorthosite outcrop after Yamamoto et al. (2012).

c) Grail gravity map of the Riemann-Fabry basin region (NASA/JPL-Caltech/GSFC/MIT; Zuber et al. 2013).

# APPENDIX

## Appendix Figure Captions

Figure A1. Planar deformation features in Shişr 161 plagioclase.

a) and b) planar deformation features (PDF) in plagioclase crystals of clast 54; black arrows show traces of PDF orientations; plane polarized light images.

Figure A2. Maskelynite in Shişr 161.

a) Maskelynite (m), fractured pyroxene (px), and olivine (ol) assemblage, plane polarized light image;

b) cross polarized light image of the same clast as in (a) shows isotropic property of the diaplectic plagioclase glass;

c) rotated BSE image of the same grain, note characteristic smooth surface of the glass.

Figure A3. Barred chondrule-like clast.

a) Reflected light micrograph, ol-olivine, pl-plagioclase;

b) slightly rotated BSE image with approximate outline of clast as a white, dotted line.

Table 1. Modal mineralogy of spherules in Shişr 161.

| Clast number | plagioclase [vol%] | mesostasis [vol%] | pyroxene [vol%] | olivine [vol%] | opaques [vol%] | void space [vol%] | CIPW modal mineralogy | size [$mm^2$] |
|---|---|---|---|---|---|---|---|---|
| Sph1 | 33.2 | 24.9 | 41.5 | n.d. | 0.4 | 1.5 | norite | 0.013 |
| Sph2[a] | 24.7 | n.d. | n.d. | 74.0 | 1.3 | 3.4 | troctolite | 0.029 |
| Sph2[b] | 79.9 | 20.0 | n.d. | n.d. | 0.1 | 2.6 | troctolitic anorthosite | 0.005 |
| Sph3 | 56.5 | n.d. | 41.6 | n.d. | 1.9 | 1.2 | norite | 0.163 |
| Sph4 | 61.8 | n.d. | 30.9 | 7.2 | 0.1 | 4.0 | anorthositic norite | 0.010 |
| Sph5 | 54.9 | n.d. | n.d. | 44.0 | 1.1 | 3.3 | troctolite | 0.019 |
| Sph6 | 15.0 | 81.8 | 3.2 | n.d. | n.d. | 1.2 | noritic anorthosite | 0.004 |
| Sph7 | 53.8 | 26.9 | 8.9 | 8.9 | 1.5 | 7.5 | anorthositic norite | 0.013 |
| Sph8 | 30.5 | 68.9 | n.d. | n.d. | 0.6 | 0.8 | anorthositic norite | 0.002 |
| Sph9[c] | n.d. | 100.0 | n.d. | n.d. | n.d. | n.d. | pyroxenite | 0.004 |
| Sph10 | 78.0 | 22.0 | n.d. | n.d. | n.d. | 2.9 | anorthosite | 0.035 |
| Sph13 | 82.7 | 17.3 | n.d. | n.d. | n.d. | 2.4 | troctolitic anorthosite | 0.004 |
| Sph15 | 75.3 | 23.9 | n.d. | 0.7 | 0.1 | 6.4 | noritic anorthosite | 0.004 |
| Sph17 | 69.4 | n.d. | 29.7 | 0.9 | n.d. | 6.3 | gabbroic norite | 0.011 |

n.d.-none detected; [a]main part of a composite spherule; [b]minor/accreted part of a composite particle; [c]gas-associated spheroidal particle.

| texture |
| --- |
| |
| hyalophitic |
| hyalophitic-accretionary |
| hyalophitic-accretionary |
| subophitic |
| subophitic-accretionary |
| subophitic |
| cryptocrystalline |
| hyalophitic-accretionary |
| cryptocrystalline |
| cryptocrystalline-accretionary |
| hyalophitic |
| hyalophitic |
| hyalophitic |
| subophitic |

Table 2. Modal mineralogy of crystallized melt clasts in Shişr 161.

| clast | plagioclase [vol%] | low-Ca pyroxene [vol%] | high-Ca pyroxene [vol%] | olivine [vol%] | ilmenite [vol%] | chromite [vol%] | FeS + FeNi [vol%] | void space [vol%] | modal lithology[a] | size [mm$^2$] | texture |
|---|---|---|---|---|---|---|---|---|---|---|---|
| 3 | 78.2 | n.d. | 17.1 | 4.4 | 0.3 | n.d. | n.d. | n.d. | noritic anorthosite | 1.91 | poikilitic |
| 4 | 79.7 | n.d. | 16 | 3.9 | 0.2 | 0.2 | n.d. | n.d. | noritic anorthosite | 1.237 | intergranular |
| 8 | 77.1 | n.d. | 17.1 | 5.6 | n.d. | 0.2 | n.d. | n.d. | anorthositic troctolite | 2.517 | poikilitic |
| 18 | 70.8 | 7.4 | 11.1 | 10.3 | 0.1 | 0.2 | 0.1 | n.d. | anorthositic norite | 1.192 | subophitic |
| 23 | 42.8 | 25.8 | 30.6 | 0.5 | n.d. | 0.2 | 0.1 | 1.2 | noritic gabbro | 18.263 | variolitic |
| 27 | 72.6 | 12.2 | n.d. | 15.1 | n.d. | 0.1 | n.d. | 6.3 | anorthositic troctolite | 0.892 | intergranular |
| 36 | 64.9 | n.d. | 2.4 | 32.6 | n.d. | 0.1 | n.d. | 11 | anorthositic troctolite | 1.039 | coalescent |
| 43 | 66 | 17.2 | n.d. | 16 | 0.3 | 0.4 | 0.1 | 13.1 | anorthositic norite | 2.295 | intergranular |
| 46 | 79.2 | n.d. | 14.4 | 6.1 | n.d. | n.d. | 0.3 | 7.4 | noritic anorthosite | 0.988 | poikilitic |
| 50 | 83.9 | n.d. | 13.5 | 2.4 | n.d. | 0.2 | n.d. | 9.5 | noritic anorthosite | 2.914 | intergranular |
| 63 | 60.1 | 13 | 25.4 | n.d. | 0.5 | 0.5 | 0.5 | 4.9 | anorthositic gabbro | 1.031 | coalescent |
| 74 | 51.6 | 23.1 | 24.9 | n.d. | n.d. | 0.2 | 0.2 | 5.2 | noritic gabbro | 0.174 | poikilitic |
| 115 | 63.4 | 27.8 | 3.8 | 4.5 | 0.2 | n.d. | 0.3 | 6.1 | anorthositic norite | 0.426 | poikilitic |
| 118 | 75.8 | n.d. | 20.2 | 3.4 | 0.3 | 0.3 | n.d. | 10.7 | anorthositic norite | 0.73 | intergranular |
| 126 | 68.9 | n.d. | 26 | 4.6 | n.d. | 0.5 | n.d. | 15.4 | anorthositic norite | 0.409 | intergranular |
| 135 | 82.7 | 11 | 2.3 | 3.7 | n.d. | 0.2 | 0.1 | 7 | noritic anorthosite | 0.374 | intergranular |
| 148 | 81.3 | n.d. | 14.4 | 4 | n.d. | n.d. | 0.3 | 11.4 | noritic anorthosite | 0.587 | poikilitic |
| 156 | 72 | n.d. | 27.9 | n.d. | | 0.1[b] | | 9.3 | anorthositic gabbro | 0.075 | poikilitic |
| 159 | 64.7 | n.d. | 0.6 | 34.7 | n.d. | n.d. | n.d. | 10 | anorthositic troctolite | 0.05 | poikilitic |
| 5 | 72.9 | 15.6 | 6.5 | 4.9 | n.d. | 0.1 | n.d. | 8.6 | anorthositic norite | 6.645 | cumulate |
| 16 | 81.9 | 1.5 | 8.5 | 8.1 | n.d. | n.d. | n.d. | 12.1 | noritic anorthosite[c] | 0.832 | cataclastic cumulate |
| 17 | 80.8 | 6.1 | n.d. | 13 | n.d. | n.d. | 0.1 | 4.9 | troctolitic anorthosite | 0.704 | cumulate |
| 25 | 76.5 | 4.8 | 6.9 | 11.1 | n.d. | 0.6 | 0.1 | 13.8 | anorthositic norite | 1.834 | cumulate |
| 26 | 69.2 | 11.9[d] | 17.1 | 0.6 | 0.7 | 0.4 | 0.1 | 7.4 | anorthositic norite | 6.468 | cumulate |
| 54 | 80.3 | 11.2 | 3.2 | 5.1 | n.d. | 0.1 | 0.1 | 5.3 | noritic anorthosite[e] | 24.847 | cumulate |
| 107 | 70.5 | 19.3 | n.d. | 10.2 | n.d. | n.d. | n.d. | 11.3 | anorthositic norite | 0.275 | cumulate |
| 10 | 78.1 | 14.2 | 3.1 | 4.4 | 0.05 | 0.1 | 0.05 | 3.0 | noritic anorthosite | 3.333 | clast-bearing cumulate |
| 34 | 71.4 | 12.1 | 0.2 | 16 | n.d. | 0.2 | 0.1 | 10.0 | anorthositic troctolite | 5.83 | clast-bearing cumulate |
| 38 | 78 | 7.9 | n.d. | 13.6 | n.d. | 0.5 | n.d. | 8.9 | troctolitic anorthosite | 0.696 | clast-bearing cumulate |

| | | | | | | | | | | | |
|---|---|---|---|---|---|---|---|---|---|---|---|
| 88 | 72.3 | 11.4 | n.d. | 15.9 | n.d. | 0.2 | 0.2 | 17.7 | anorthositic troctolite | 0.413 | cumulate |
| 116 | 94.9 | 1.2 | 2.8 | 1 | 0.1 | n.d. | 0 | 12.1 | anorthosite | 0.567 | cataclastic cumulate |

[a] lithologic designations after Stöffler et al. (1980); [b] undiscriminated opaques; [c] clast is transected by glassy shock melt vein; [d] low-Ca pyroxene is pig

geonite; [e]clast is partially coated with glassy impact melt.

Table 3. Modal mineralogy of vitrophyre clasts in Shişr 161.

| clast | mesostasis / glass[a] | plagioclase | pyroxene | olivine | chromite | FeS + FeNi | void space | modal lithology[b] | size | type |
|---|---|---|---|---|---|---|---|---|---|---|
| | [vol%] | [vol%] | [vol%] | [vol%] | [vol%] | [vol%] | [vol%] | | [mm$^2$] | |
| 2 | 48.8 | 39.4 | n.d. | 11.8 | n.d. | n.d. | 1.4 | anorthositic troctolite | 3.668 | angular, hyalophitic, clast- |
| 6 | 42.4 | 56.5 | n.d. | 1 | n.d. | 0.1 | 4.5 | troctolitic anorthosite | 0.991 | angular, hyalophitic, clast- |
| 7 | 24.4 | 52.6 | 11 | 11.7 | 0.3 | n.d. | 10.1 | anorthositic norite | 0.774 | angular hyalophitic, clast- |
| 11 | 14.3 | 85.7 | n.d. | n.d. | n.d. | n.d. | 8.7 | anorthosite | 0.975 | angular, hyalophitic, clast- |
| 12 | 16 | 39.4 | 26.5 | 18.1 | n.d. | n.d. | 5.8 | olivine norite | 1.251 | ameboid, hyalophitic, clast- |
| 13 | 73.5 | 25.2 | 1.3 | n.d. | n.d. | n.d. | 4.5 | noritic anorthosite | 0.471 | angular, hyalophitic, clast- |
| 15 | 58 | 15.9 | 22.2 | 3.7 | 0.1 | 0.1 | 2.5 | norite | 0.252 | ameboid, hyalophitic, clast-rich (ropy glass) |
| 19 | 38 | 47.7 | 12.9 | 1.2 | 0.1 | 0.1 | 4.7 | anorthositic norite | 0.348 | angular, hyalophitic, clast- |
| 20 | 31.5 | 50.1 | 16.1 | 2.2 | n.d. | 0.1 | 8.1 | olivine norite | 0.708 | angular, hyalophitic, clast- |
| 28 | 54.7 | 43.3 | 1.2 | 0.7 | 0.1 | n.d. | 6 | anorthositic norite | 0.141 | ameboid, hyal-phitic, clast-rich (ropy glass) |
| 30 | n.d. (holohyaline | 62.7 | 34.6 | 2.7 | n.a. | n.a. | n.a. | anorthositic norite | 0.406 | ameboid, ropy glass, clast-rich |
| 33 | 44.2 | 55.8 | n.d. | n.d. | n.d. | n.d. | 6 | anorthositic norite | 0.359 | ameboid, hyalophitic, clast-rich (ropy glass) |
| 37 | n.d. (hypohyaline | 62.6 | 35.0 | 2.4 | n.a. | n.a. | n.a. | anorthositic norite | 0.973 | ameboid, ropy glass, clast-rich |
| 44 | n.d. (hypohyaline ) | 79.1 | 13.0 | 7.9 | n.a. | n.a. | n.a. | noritic anorthosite | 0.238 | glass shard |
| 51 | n.d. (hypohyaline ) | 86.6 | 7.4 | 6.0 | n.a. | n.a. | n.a. | noritic anorthosite | 0.349 | glass shard |
| 52 | n.d. (holohyaline | 65.6 | 30.9 | 3.6 | n.a. | n.a. | n.a. | anorthositic norite | 0.549 | ameboid, ropy glass, clast-rich |
| 53 | n.d. (hypohyaline ) | 64.9 | 31.7 | 3.4 | n.a. | n.a. | n.a. | anorthositic norite | 12.023 | glass coat[b] |
| 58 | 32 | 63.8 | 3.2 | 0.7 | n.d. | 0.3 | 9.5 | troctolitic anorthosite | 1.403 | angular, hyalophitic, clast- |
| 59 | cryptocrystal line | 86.8 | 6.9 | 6.3 | n.a. | n.a. | n.a. | noritic anorthosite | 0.245 | subrounded, clast-free |
| 77 | n.d. (hypohyaline ) | 86.0 | 6.5 | 7.5 | n.a. | n.a. | n.a. | troctolitic anorthosite | 0.089 | glass shard |
| 81 | 64.8 | 33.9 | n.d. | 1.3 | n.d. | n.d. | 6.5 | anorthositic norite | 0.562 | angular, hyalophitic, clast- |
| 95 | 45.1 | 52.5 | n.d. | 2.4 | n.d. | n.d. | 7.4 | anorthositic norite | 0.706 | angular, hyalophitic, clast- |
| 102 | n.d. (hypohyaline | 70.1 | 23.8 | 6.1 | n.a. | n.a. | n.a. | anorthositic norite | 0.276 | ameboid, hyalophitic, clast- |

| | | | | | | | | | | |
|---|---|---|---|---|---|---|---|---|---|---|
| 123 | 36.4 | 63.1 | n.d. | 0.3 | n.d. | 0.2 | 7.1 | anorthositic norite | 0.946 | ameboid, hyalophitic, clast-bearing |
| 136 | 43.3 | 55.1 | n.d. | 1.5 | 0.1 | n.d. | 13.3 | anorthositic norite | 0.555 | angular, hyalophitic, clast- |
| g-1 | n.d. (holohyaline ) | 59.3 | 40.7 | 0.0 | n.a. | n.a. | n.a. | gabbroic norite | 0.077 | glass shard |
| g-3 | n.d. (holohyaline ) | 63.2 | 32.0 | 4.9 | n.a. | n.a. | n.a. | anorthositic norite | 0.052 | glass shard |
| g-4 | n.d. (holohyaline ) | 85.8 | 7.5 | 6.7 | n.a. | n.a. | n.a. | troctolitic anorthosite | 0.02 | glass shard |
| g-5 | n.d. (holohyaline ) | 85.9 | 4.5 | 9.7 | n.a. | n.a. | n.a. | troctolitic anorthosite | 0.028 | glass shard |
| g-6 | n.d. (holohyaline ) | 80.3 | 11.8 | 7.8 | n.a. | n.a. | n.a. | noritic anorthosite | 0.006 | ropy glass shard, clast-bearing |
| g-7 | n.d. (holohyaline ) | 85.5 | 11.0 | 3.5 | n.a. | n.a. | n.a. | noritic anorthosite | 0.008 | glass shard |
| g-8 | n.d. (holohyaline | 62.8 | 37.2 | 0.0 | n.a. | n.a. | n.a. | anorthositic norite | 0.005 | ropy glass shard, clast-bearing |
| g-9 | n.d. (hypohyaline ) | 80.1 | 8.7 | 11.2 | n.a. | n.a. | n.a. | troctolitic anorthosite | 0.015 | glass shard |
| g-10 | n.d. (holohyaline | 100.0 | 0.0 | 0.0 | n.a. | n.a. | n.a. | anorthosite | 0.014 | ropy glass shard, clast-bearing |
| g-11a | n.d. (holohyaline ) | 83.9 | 11.5 | 4.6 | n.a. | n.a. | n.a. | noritic anorthosite | 0.028 | glass shard, clast-free |
| g-11b | n.d. (holohyaline ) | 76.7 | 9.1 | 14.1 | n.a. | n.a. | n.a. | anorthositic troctolite | 0.009 | ropy glass shard |
| g-12 | n.d. (holohyaline | 26.0 | 68.9 | 5.1 | n.a. | n.a. | n.a. | norite | 0.011 | ameboid, ropy glass, clast-rich |
| g-13 | n.d. (holohyaline ) | 75.3 | 10.6 | 14.1 | n.a. | n.a. | n.a. | anorthositic troctolite | 0.07 | ameboid glass, clast- + sulfide melt- rich |

a in clasts that are mostly devitrified, the remaining mesostasis melt was quantified and the modal mineral components were determined by imag

e analysis, in glassy clasts, glass proportions were not determined (n.d.) and melt compositions were determined from glass analyses by calcul

lating the modal mineralogy with the CIPW-norm; b calculated from the modaly reconstituted bulk compositions of mesostasis-bearing vitrop

hyres or or glass analyses in hyaline clasts, lithologic classification after Stöffler et al. (1980); n.a.-not applicable; n.d.-not determined; b part

ticle is a clast-rich glass coat on a cumulate clast.

Table 4. Compositions of glassy phases in Shişr 161.

| clast | melt type[a] | beam Ø [µm] | n | $Na_2O$ [wt%] | MgO [wt%] | $Al_2O_3$ [wt%] | $SiO_2$ [wt%] | $K_2O$ [wt%] | CaO [wt%] | MnO [wt%] | FeO [wt%] | $TiO_2$ [wt%] | $Cr_2O_3$ [wt%] | $P_2O_5$ [wt%] |
|---|---|---|---|---|---|---|---|---|---|---|---|---|---|---|
| 2 | m | 0 | 4 | 0.05 | 14.7 | 14.9 | 44.9 | b.d. | 8.9 | 0.22 | 15.2 | 0.53 | 0.38 | b.d. |
| 6 | m | 0 | 3 | 0.33 | 14.3 | 17.0 | 42.9 | 0.09 | 10.7 | 0.18 | 13.9 | 0.58 | 0.28 | 0.06 |
| 7 | m | 0 | 4 | 0.11 | 13.7 | 13.9 | 45.9 | 0.03 | 10.8 | 0.24 | 14.6 | 0.51 | 0.28 | b.d. |
| 11 | m | 0 | 8 | 0.08 | 3.9 | 11.5 | 52.0 | 0.06 | 12.3 | 0.32 | 16.3 | 1.79 | 0.45 | 0.04 |
| 12 | m | 0/20 | 5 | 0.22 | 9.7 | 19.4 | 46.7 | b.d. | 12.5 | 0.15 | 10.3 | 0.49 | 0.26 | b.d. |
| 13 | m | 0 | 4 | 0.31 | 4.9 | 29.2 | 44.8 | b.d. | 16.6 | 0.06 | 4.3 | 0.12 | 0.07 | b.d. |
| 15 | m | 0 | 4 | 0.21 | 10.9 | 20.0 | 46.4 | b.d. | 12.3 | 0.13 | 9.4 | 0.37 | 0.24 | b.d. |
| 16[c] | g | 0/5 | 4 | 0.38 | 3.5 | 29.6 | 44.7 | b.d. | 17.7 | b.d. | 3.8 | 0.21 | 0.08 | b.d. |
| 19 | m | 0 | 6 | 0.06 | 12.7 | 11.6 | 47.9 | b.d. | 9.5 | 0.25 | 16.8 | 0.56 | 0.36 | b.d. |
| 20 | m | 0 | 1 | 0.10 | 6.2 | 14.3 | 51.3 | 0.03 | 12.4 | 0.28 | 14.3 | 1.15 | 0.35 | b.d. |
| 23[d] | m | 5 | 1 | 0.30 | 13.2 | 17.9 | 49.8 | b.d. | 9.8 | 0.08 | 7.9 | 0.16 | 0.66 | b.d. |
| 28 | m | 0 | 5 | 0.13 | 10.5 | 15.8 | 48.3 | b.d. | 10.9 | 0.20 | 13.1 | 0.66 | 0.35 | b.d. |
| 30 | g | 0/10 | 6 | 0.26 | 8.7 | 19.9 | 46.3 | b.d. | 12.5 | 0.16 | 10.1 | 0.48 | 0.26 | b.d. |
| 33 | m | 0 | 9 | 0.16 | 11.4 | 17.4 | 46.7 | b.d. | 10.7 | 0.19 | 12.0 | 0.50 | 0.33 | b.d. |
| 37 | g | 10 | 4 | 0.26 | 8.9 | 19.8 | 46.6 | b.d. | 12.4 | 0.10 | 10.1 | 0.43 | 0.27 | b.d. |
| 44 | g | 0/10 | 4 | 0.28 | 7.1 | 26.5 | 44.1 | b.d. | 15.0 | b.d. | 5.4 | 0.20 | 0.16 | b.d. |
| 51 | g | 10 | 7 | 0.17 | 5.3 | 29.9 | 43.6 | b.d. | 16.4 | b.d. | 3.2 | 0.12 | b.d. | b.d. |
| 52 | g | 0 | 4 | 0.28 | 8.9 | 21.5 | 45.9 | b.d. | 12.9 | 0.12 | 8.9 | 0.39 | 0.22 | b.d. |
| 53 | g | 20 | 10 | 0.28 | 9.0 | 21.1 | 46.7 | b.d. | 13.0 | 0.14 | 9.0 | 0.41 | 0.25 | b.d. |
| 58 | m | 0 | 6 | 0.20 | 15.9 | 17.4 | 44.4 | b.d. | 10.5 | 0.14 | 10.4 | 0.35 | 0.27 | b.d. |
| 59 | g | 10 | 12 | 0.23 | 5.2 | 30.2 | 44.0 | b.d. | 16.6 | b.d. | 3.1 | 0.12 | 0.06 | b.d. |
| 77 | g | 10 | 14 | 0.38 | 5.4 | 29.7 | 44.2 | b.d. | 16.5 | b.d. | 3.2 | 0.12 | b.d. | b.d. |
| 81 | m | 5 | 6 | 0.21 | 13.1 | 17.8 | 47.2 | b.d. | 11.4 | 0.16 | 9.0 | 0.41 | 0.23 | b.d. |
| 95 | m | 0 | 5 | 0.15 | 10.9 | 17.1 | 46.5 | b.d. | 11.6 | 0.19 | 12.0 | 0.53 | 0.28 | b.d. |
| 102 | g | 0 | 5 | 0.25 | 8.4 | 23.0 | 45.5 | b.d. | 13.7 | 0.13 | 7.7 | 0.30 | 0.25 | b.d. |
| 123 | m | 0 | 2 | b.d. | 19.6 | 10.8 | 46.5 | b.d. | 7.6 | 0.22 | 13.2 | 0.90 | 0.58 | 0.10 |
| 136 | m | 0 | 3 | 0.10 | 17.5 | 8.77 | 46.7 | b.d. | 9.0 | 0.27 | 16.9 | 0.63 | 0.37 | b.d. |
| g-1 | g | 20 | 5 | 0.04 | 8.5 | 16.5 | 51.5 | 0.03 | 11.5 | 0.13 | 7.9 | 1.46 | 0.19 | b.d. |
| g-3 | g | 20 | 5 | 0.26 | 8.6 | 19.9 | 45.4 | b.d. | 12.7 | 0.15 | 10.0 | 0.46 | 0.31 | b.d. |
| g-4 | g | 20 | 5 | 0.08 | 4.5 | 29.6 | 43.0 | b.d. | 16.9 | 0.07 | 4.2 | 0.20 | 0.08 | b.d. |
| g-5 | g | 20 | 4 | 0.36 | 5.4 | 29.3 | 43.3 | b.d. | 16.9 | b.d. | 3.3 | 0.13 | 0.07 | b.d. |
| g-6 | g | 20 | 3 | 0.05 | 6.6 | 27.4 | 43.4 | b.d. | 16.4 | 0.07 | 4.0 | 0.22 | 0.20 | b.d. |
| g-7 | g | 20 | 3 | 0.15 | 3.4 | 28.8 | 43.0 | b.d. | 16.5 | 0.07 | 5.0 | 0.18 | 0.14 | b.d. |
| g-8 | g | 20 | 3 | 1.90 | 6.0 | 13.3 | 44.5 | 0.77 | 10.4 | 0.16 | 12.8 | 4.14 | 0.17 | 2.49 |
| g-9 | g | 20 | 4 | 0.37 | 6.3 | 26.7 | 43.4 | b.d. | 16.1 | 0.08 | 5.4 | 0.27 | 0.13 | b.d. |
| g-10 | g | 20 | 3 | 0.15 | 4.4 | 33.5 | 38.6 | b.d. | 19.5 | b.d. | 2.0 | 0.19 | 0.11 | b.d. |
| g-11a | g | 20 | 4 | 0.32 | 4.4 | 28.5 | 44.2 | b.d. | 16.6 | 0.07 | 4.6 | 0.23 | 0.14 | b.d. |
| g-11b | g | 20 | 4 | 0.20 | 9.6 | 25.7 | 43.3 | 0.05 | 14.5 | 0.06 | 4.8 | 0.19 | 0.13 | b.d. |
| g-12 | g | 20 | 4 | 0.09 | 4.8 | 7.04 | 44.3 | b.d. | 10.5 | 0.39 | 29.3 | 1.68 | 0.25 | b.d. |
| g-13 | g | 20 | 1 | 0.22 | 7.6 | 24.8 | 42.9 | b.d. | 14.4 | 0.10 | 8.2 | 0.24 | 0.15 | b.d. |
| Sph1 | m | 0 | 4 | 0.15 | 13.9 | 19.6 | 49.0 | b.d. | 10.7 | 0.11 | 5.8 | 0.57 | 0.33 | b.d. |
| Sph2 | m | 0 | 2 | 0.12 | 28.4 | 6.14 | 41.9 | 0.06 | 4.5 | 0.17 | 20.3 | 0.28 | 0.09 | 0.11 |
| Sph6 | m | 0 | 3 | 0.20 | 7.3 | 26.36 | 43.9 | 0.04 | 14.6 | 0.10 | 6.7 | 0.30 | 0.06 | 0.06 |
| Sph7 | m | 0 | 4 | 0.39 | 2.5 | 12.6 | 58.9 | 3.60 | 6.6 | 0.12 | 6.1 | 3.84 | 0.09 | 2.87 |
| Sph8 | m | 0 | 4 | 0.22 | 6.2 | 24.8 | 45.1 | 0.05 | 15.0 | 0.12 | 7.3 | 0.42 | 0.11 | 0.05 |
| Sph9[e] | g | 0 | 6 | 1.07 | 2.3 | 0.17 | 64.2 | 0.07 | 2.6 | 0.35 | 27.8 | b.d. | 0.21 | b.d. |
| Sph10 | m | 0 | 5 | 0.19 | 11.1 | 17.8 | 43.5 | 0.06 | 13.0 | 0.21 | 13.2 | 0.55 | 0.22 | 0.09 |
| Sph13 | m | 0 | 4 | 0.39 | 3.4 | 30.4 | 43.6 | b.d. | 16.8 | 0.07 | 3.9 | 0.15 | 0.09 | b.d. |
| Sph15 | m | 0 | 4 | 0.20 | 9.3 | 19.9 | 46.9 | 0.03 | 13.3 | 0.15 | 10.4 | 0.40 | 0.30 | b.d. |

n-number of averaged analyses; b.d.-below detection; [a] melt types are m-mesostasis or g-glass, see text for details; [b] Mg# is 100×molar Mg/(Mg+Fe

| $SO_3$ [wt%] | total [wt%] | total [afu] | Mg#[b] [mol%] | Ca[b] [mol%] | Na[b] [mol%] | K[b] [mol%] | Mg/Al [wt%] |
|---|---|---|---|---|---|---|---|
| 0.15 | 100.0 | 16.0 | 63.2 | 98.5 | 1.2 | b.d. | 1.1 |
| 0.32 | 100.5 | 16.1 | 64.7 | 93.9 | 5.2 | 0.9 | 1.0 |
| 0.17 | 100.3 | 15.9 | 62.6 | 97.9 | 1.8 | 0.3 | 1.1 |
| 0.23 | 99.0 | 15.0 | 30.3 | 98.3 | 1.2 | 0.5 | 0.4 |
| 0.12 | 99.8 | 15.5 | 63.0 | 96.7 | 3.1 | b.d. | 0.6 |
| 0.07 | 100.6 | 15.3 | 67.0 | 96.6 | 3.3 | b.d. | 0.2 |
| 0.13 | 100.2 | 15.6 | 67.4 | 97.0 | 2.9 | b.d. | 0.6 |
| b.d. | 100.0 | 15.2 | 62.1 | 96.1 | 3.8 | b.d. | **0.1** |
| 0.07 | 99.8 | 15.8 | 57.1 | 98.6 | 1.1 | b.d. | 1.2 |
| 0.29 | 100.8 | 15.1 | 43.7 | 98.2 | 1.4 | 0.3 | 0.5 |
| 0.03 | 99.9 | 15.4 | 74.8 | 94.6 | 5.2 | b.d. | 0.8 |
| 0.16 | 100.0 | 15.5 | 58.8 | 97.9 | 2.1 | b.d. | 0.8 |
| 0.13 | 98.9 | 15.5 | 60.5 | 96.3 | 3.6 | b.d. | **0.5** |
| 0.09 | 99.6 | 15.6 | 63.1 | 97.3 | 2.5 | b.d. | 0.7 |
| 0.11 | 99.1 | 15.5 | 61.1 | 96.2 | 3.6 | b.d. | **0.5** |
| 0.08 | 98.9 | 15.4 | 70.0 | 96.6 | 3.3 | b.d. | **0.3** |
| b.d. | 98.9 | 15.3 | 74.9 | 98.1 | 1.8 | b.d. | **0.2** |
| 0.09 | 99.2 | 15.5 | 64.1 | 96.2 | 3.7 | b.d. | **0.5** |
| 0.13 | 100.1 | 15.5 | 63.9 | 96.2 | 3.7 | b.d. | **0.5** |
| 0.15 | 99.7 | 16.0 | 73.2 | 96.6 | 3.3 | b.d. | 1.0 |
| b.d. | 99.6 | 15.3 | 75.1 | 97.5 | 2.5 | b.d. | **0.2** |
| 0.07 | 99.7 | 15.3 | 75.3 | 95.9 | 4.0 | b.d. | **0.2** |
| 0.07 | 99.7 | 15.6 | 72.1 | 96.6 | 3.2 | b.d. | 0.8 |
| 0.15 | 99.5 | 15.6 | 61.4 | 97.5 | 2.3 | b.d. | 0.7 |
| b.d. | 99.2 | 15.5 | 66.1 | 96.7 | 3.2 | b.d. | **0.4** |
| 0.14 | 99.7 | 16.0 | 72.5 | 99.3 | 0.5 | b.d. | 2.1 |
| 0.05 | 100.3 | 16.2 | 65.0 | 97.7 | 2.1 | b.d. | 2.3 |
| b.d. | 97.7 | 15.0 | 45.7 | 99.3 | 0.4 | 0.3 | **0.6** |
| 0.09 | 97.9 | 15.5 | 40.1 | 97.8 | 2.1 | b.d. | **0.5** |
| b.d. | 98.7 | 15.3 | 45.5 | 99.4 | 0.5 | b.d. | **0.2** |
| 0.06 | 98.9 | 15.4 | 56.4 | 97.7 | 2.2 | b.d. | **0.2** |
| b.d. | 98.5 | 15.4 | 56.0 | 99.7 | 0.3 | b.d. | **0.3** |
| b.d. | 97.4 | 15.2 | 34.3 | 98.9 | 0.9 | b.d. | **0.1** |
| b.d. | 96.6 | 15.4 | 26.8 | 78.3 | 14.9 | 6.8 | **0.5** |
| 0.14 | 99.0 | 15.5 | 47.6 | 97.6 | 2.3 | b.d. | **0.3** |
| b.d. | 98.6 | 15.6 | 62.4 | 99.1 | 0.8 | b.d. | **0.1** |
| b.d. | 99.1 | 15.3 | 42.3 | 98.0 | 2.0 | b.d. | **0.2** |
| 0.05 | 98.5 | 15.6 | 60.9 | 98.2 | 1.4 | 0.4 | **0.4** |
| 0.36 | 98.7 | 15.8 | 11.2 | 99.1 | 0.9 | b.d. | **0.8** |
| 0.08 | 99.2 | 15.6 | 62.3 | 97.2 | 2.6 | b.d. | **0.4** |
| b.d. | 100.1 | 15.5 | 81.0 | 97.3 | 2.5 | b.d. | 0.8 |
| 0.05 | 102.1 | 17.1 | 71.2 | 94.3 | 4.6 | 1.1 | 5.3 |
| 0.02 | 99.6 | 15.5 | 66.1 | 97.3 | 2.4 | 0.3 | 0.3 |
| 0.14 | 97.8 | 14.1 | 42.6 | 57.2 | 6.1 | 36.7 | 0.2 |
| 0.37 | 99.7 | 7.7 | 61.0 | 97.0 | 2.6 | 0.4 | 0.3 |
| 0.98 | 99.8 | 14.4 | 12.7 | 55.1 | 43.1 | 1.8 | **15.2** |
| 0.26 | 100.2 | 15.9 | 60.6 | 96.9 | 2.6 | 0.6 | 0.7 |
| b.d. | 98.9 | 12.7 | 61.2 | 95.8 | 4.1 | b.d. | 0.1 |
| 0.05 | 101.0 | 15.5 | 61.1 | 97.1 | 2.7 | 0.2 | 0.5 |

e), Ca is 100×molar Ca/(Ca+Na+K), Na is 100×molar Na/(Na+Ca+K), and K is 100*molar K/(Ca+Na+K); [c] analyses on glassy shock melt vein that t transsects cumulate clast 16; [d] analyses on scarce domains of mesostasis in the crystallized melt clast; afu is atoms per formula unit; [e]composition is nearly identical to the Al- and Ca-depleted (Fe-)GASP particles of Warren (2008), except for an enrichment in $Na_2O$; the composition of all anal yses were below the detection limit for NiO except clast g-13 (0.34 wt%).

Table 5. Modaly recombined bulk compositions of melt clasts in Shişr 161.

| clast | type[a] | $SiO_2$ [wt%] | $TiO_2$ [wt%] | $Al_2O_3$ [wt%] | $Cr_2O_3$ [wt%] | FeO[b] [wt%] | MnO [wt%] | MgO [wt%] | CaO [wt%] | $Na_2O$ [wt%] | $K_2O$ [wt%] | $P_2O_5$ [wt%] |
|---|---|---|---|---|---|---|---|---|---|---|---|---|
| 2 | vi | 43.4 | 0.3 | 20.4 | 0.2 | 10.7 | 0.2 | 13.0 | 11.5 | 0.2 | 0.0 | 0.0 |
| 6 | vi | 43.3 | 0.3 | 26.6 | 0.1 | 6.8 | 0.1 | 6.9 | 15.3 | 0.4 | 0.0 | 0.0 |
| 7 | vi | 44.2 | 0.3 | 21.1 | 0.3 | 9.5 | 0.1 | 10.8 | 13.4 | 0.2 | 0.0 | 0.0 |
| 11 | vi | 45.1 | 0.3 | 32.1 | 0.1 | 2.8 | 0.1 | 0.9 | 18.3 | 0.2 | 0.0 | 0.0 |
| 12 | vi | 46.3 | 0.3 | 16.4 | 0.2 | 9.6 | 0.1 | 17.4 | 9.4 | 0.2 | 0.0 | 0.0 |
| 13 | vi | 44.5 | 0.1 | 30.2 | 0.1 | 3.5 | 0.1 | 4.0 | 17.2 | 0.3 | 0.0 | 0.0 |
| 15 | vi | 47.5 | 0.4 | 16.9 | 0.3 | 9.3 | 0.1 | 14.7 | 10.3 | 0.2 | 0.0 | 0.0 |
| 19 | vi | 46.5 | 0.3 | 20.5 | 0.3 | 10.3 | 0.2 | 9.0 | 12.6 | 0.2 | 0.0 | 0.0 |
| 20 | vi | 45.1 | 0.3 | 18.2 | 0.2 | 10.1 | 0.1 | 15.1 | 10.5 | 0.2 | 0.0 | 0.0 |
| 28 | vi | 46.5 | 0.4 | 23.3 | 0.3 | 8.3 | 0.1 | 6.7 | 14.0 | 0.2 | 0.0 | 0.0 |
| 33 | vi | 46.4 | 0.3 | 25.4 | 0.2 | 6.6 | 0.1 | 5.9 | 14.7 | 0.4 | 0.0 | 0.0 |
| 58 | vi | 44.0 | 0.2 | 27.9 | 0.1 | 4.8 | 0.1 | 7.0 | 15.4 | 0.3 | 0.0 | 0.0 |
| 81 | vi | 46.5 | 0.3 | 22.6 | 0.2 | 6.8 | 0.1 | 9.6 | 13.5 | 0.3 | 0.0 | 0.0 |
| 95 | vi | 44.9 | 0.3 | 26.0 | 0.1 | 6.9 | 0.1 | 6.6 | 14.7 | 0.2 | 0.0 | 0.0 |
| 123 | vi | 44.2 | 0.4 | 25.6 | 0.2 | 6.8 | 0.1 | 7.6 | 14.6 | 0.2 | 0.0 | 0.0 |
| 136 | vi | 44.9 | 0.3 | 22.5 | 0.2 | 8.7 | 0.1 | 8.9 | 13.9 | 0.2 | 0.0 | 0.0 |
| Sph1 | vi | 49.9 | 0.7 | 15.5 | 0.2 | 8.8 | 0.2 | 13.4 | 10.6 | 0.3 | 0.0 | 0.1 |
| Sph2-main | vi | 37.3 | 0.1 | 7.4 | 0.5 | 27.3 | 0.2 | 23.2 | 3.9 | 0.1 | 0.0 | 0.0 |
| Sph2-accreted | vi | 43.2 | 0.1 | 28.8 | 0.0 | 5.0 | 0.0 | 6.5 | 15.9 | 0.3 | 0.0 | 0.0 |
| Sph6 | vi | 44.2 | 0.3 | 26.8 | 0.1 | 5.7 | 0.1 | 6.6 | 15.9 | 0.2 | 0.0 | 0.0 |
| Sph7 | vi | 48.8 | 1.4 | 20.4 | 0.2 | 7.4 | 0.1 | 6.5 | 11.7 | 0.6 | 1.2 | 1.0 |
| Sph8 | vi | 44.4 | 0.5 | 25.6 | 0.1 | 6.9 | 0.1 | 7.0 | 14.6 | 0.3 | 0.1 | 0.0 |
| Sph10 | vi | 43.3 | 0.1 | 32.6 | 0.0 | 2.4 | 0.0 | 2.2 | 18.9 | 0.3 | 0.0 | 0.0 |
| Sph13 | vi | 42.0 | 0.1 | 30.4 | 0.0 | 5.7 | 0.1 | 4.7 | 16.5 | 0.3 | 0.0 | 0.0 |
| Sph15 | vi | 44.2 | 0.2 | 30.8 | 0.1 | 3.5 | 0.0 | 3.1 | 17.7 | 0.3 | 0.0 | 0.0 |
| 3 | cm | 44.6 | 0.30 | 27.1 | 0.20 | 5.66 | 0.10 | 5.89 | 15.7 | 0.35 | 0.04 | 0.02 |
| 4 | cm | 44.3 | 0.42 | 27.9 | 0.19 | 4.98 | 0.08 | 6.02 | 15.7 | 0.28 | 0.03 | 0.02 |
| 8 | cm | 44.3 | 0.24 | 27.1 | 0.25 | 5.27 | 0.10 | 5.77 | 16.6 | 0.26 | 0.01 | 0.01 |
| 18 | cm | 44.7 | 0.33 | 24.1 | 0.23 | 6.87 | 0.10 | 9.10 | 14.2 | 0.24 | 0.02 | 0.01 |
| 23 | cm | 48.8 | 0.28 | 14.6 | 0.66 | 14.33 | 0.24 | 10.68 | 10.2 | 0.20 | 0.01 | 0.01 |
| 27 | cm | 44.1 | 0.14 | 24.9 | 0.15 | 5.99 | 0.09 | 10.96 | 13.4 | 0.29 | 0.01 | 0.01 |
| 36 | cm | 42.3 | 0.10 | 21.6 | 0.17 | 7.06 | 0.09 | 16.20 | 12.2 | 0.20 | 0.01 | 0.02 |
| 43 | cm | 44.4 | 0.43 | 22.5 | 0.37 | 6.15 | 0.09 | 13.46 | 12.2 | 0.21 | 0.01 | 0.01 |
| 46 | cm | 44.7 | 0.12 | 27.7 | 0.11 | 4.90 | 0.08 | 6.52 | 15.4 | 0.25 | 0.01 | 0.02 |
| 50 | cm | 44.6 | 0.22 | 29.8 | 0.16 | 3.92 | 0.07 | 4.46 | 16.5 | 0.26 | 0.02 | 0.02 |
| 63 | cm | 46.2 | 0.74 | 20.6 | 0.56 | 8.99 | 0.14 | 6.54 | 15.5 | 0.33 | 0.02 | 0.01 |
| 74 | cm | 48.2 | 0.50 | 17.6 | 0.31 | 7.88 | 0.15 | 10.02 | 14.9 | 0.24 | 0.02 | 0.01 |
| 115 | cm | 45.5 | 0.50 | 22.4 | 0.28 | 8.42 | 0.14 | 8.65 | 13.7 | 0.26 | 0.01 | 0.01 |
| 118 | cm | 45.4 | 0.47 | 26.2 | 0.25 | 6.12 | 0.09 | 6.33 | 14.6 | 0.41 | 0.02 | 0.02 |

| | | | | | | | | | | | | |
|---|---|---|---|---|---|---|---|---|---|---|---|---|
| 126 | cm | 45.9 | 0.41 | 23.6 | 0.38 | 6.58 | 0.11 | 7.33 | 15.3 | 0.35 | 0.02 | 0.01 |
| 135 | cm | 44.3 | 0.19 | 29.4 | 0.18 | 4.58 | 0.07 | 4.94 | 16.0 | 0.27 | 0.01 | 0.02 |
| 148 | cm | 44.5 | 0.13 | 28.6 | 0.07 | 4.70 | 0.07 | 4.87 | 16.5 | 0.29 | 0.02 | 0.03 |
| 156 | cm | 46.7 | 0.41 | 24.9 | 0.23 | 3.26 | 0.08 | 5.50 | 18.4 | 0.41 | 0.01 | 0.02 |
| 159 | cm | 41.3 | 0.04 | 21.5 | 0.07 | 8.20 | 0.10 | 16.55 | 11.8 | 0.21 | 0.01 | 0.02 |
| Sph3 | cm | 47.5 | 0.43 | 18.7 | 0.24 | 9.88 | 0.13 | 10.34 | 10.9 | 0.41 | 0.07 | 0.06 |
| Sph4 | cm | 45.0 | 0.22 | 23.0 | 0.28 | 8.00 | 0.13 | 9.36 | 13.7 | 0.19 | 0.01 | 0.03 |
| Sph5 | cm | 40.9 | 0.10 | 17.1 | 0.12 | 11.40 | 0.12 | 19.99 | 9.2 | 0.34 | 0.07 | 0.14 |
| Sph17 | cm | 45.9 | 0.25 | 25.2 | 0.35 | 5.79 | 0.13 | 5.87 | 16.1 | 0.22 | 0.02 | 0.01 |
| 5 | mg-cu | 45.60 | 0.25 | 25.50 | 0.21 | 3.97 | 0.07 | 8.72 | 15.37 | 0.25 | 0.01 | 0.01 |
| 54 | mg-cu | 45.02 | 0.13 | 28.35 | 0.12 | 3.24 | 0.06 | 6.85 | 15.79 | 0.29 | 0.01 | 0.02 |
| 17 | mg-cu | 43.51 | 0.15 | 28.02 | 0.06 | 3.85 | 0.05 | 7.52 | 16.39 | 0.32 | 0.01 | 0.02 |
| 25 | mg-cu | 43.67 | 0.21 | 26.54 | 0.53 | 4.43 | 0.07 | 8.26 | 15.87 | 0.29 | 0.01 | 0.02 |
| 107 | mg-cu | 45.67 | 0.17 | 24.03 | 0.12 | 5.22 | 0.08 | 11.21 | 13.20 | 0.24 | 0.01 | 0.03 |
| 16 | fe-cu | 43.91 | 0.15 | 28.47 | 0.06 | 5.44 | 0.08 | 4.67 | 16.83 | 0.34 | 0.01 | 0.03 |
| 116 | fe-cu | 43.88 | 0.13 | 34.09 | 0.02 | 1.41 | 0.03 | 1.12 | 18.90 | 0.37 | 0.01 | 0.01 |
| 10 | mg-cu | 45.47 | 0.22 | 27.15 | 0.16 | 3.84 | 0.07 | 7.17 | 15.54 | 0.29 | 0.01 | 0.02 |
| 34 | mg-cu | 44.25 | 0.14 | 24.29 | 0.21 | 5.64 | 0.09 | 11.75 | 13.21 | 0.29 | 0.01 | 0.02 |
| 38 | mg-cu | 43.54 | 0.12 | 27.17 | 0.43 | 4.51 | 0.07 | 9.26 | 14.61 | 0.24 | 0.01 | 0.02 |
| 88 | mg-cu | 43.80 | 0.12 | 24.71 | 0.31 | 5.72 | 0.08 | 11.28 | 13.58 | 0.24 | 0.01 | 0.01 |
| 26 | fe-cu | 45.59 | 0.94 | 23.88 | 0.29 | 7.18 | 0.11 | 5.30 | 16.29 | 0.30 | 0.02 | 0.02 |

[a]vi are vitrophyres, cm are crystallized melts, mg-cu are magnesian cumulates, fe-cu are ferroan cumulates; clasts3-Sph17 are crystallized melts; [b]all iron as FeO; [c]magnesium number is molar 100×[Mg/(Mg+Fe)]

| total | Mg#[c] | An#[d] | plagioclase content[e] |
|---|---|---|---|
| [wt%] | [mol%] | [mol%] | [vol%] |
| 99.9 | 68.3 | 97.4 | 62.8 |
| 99.8 | 64.3 | 95.4 | 79.3 |
| 99.9 | 67.2 | 97.3 | 64.4 |
| 99.9 | 37.0 | 98.5 | 92.6 |
| 100.0 | 76.3 | 96.8 | 51.2 |
| 99.9 | 66.8 | 96.7 | 86.7 |
| 99.8 | 73.9 | 96.9 | 52.8 |
| 99.9 | 60.9 | 97.0 | 62.8 |
| 99.9 | 72.6 | 96.7 | 56.6 |
| 99.9 | 59.0 | 97.2 | 70.2 |
| 99.9 | 61.6 | 95.0 | 75.9 |
| 99.8 | 72.2 | 96.7 | 81.5 |
| 99.9 | 71.4 | 96.3 | 68.0 |
| 99.9 | 62.9 | 97.1 | 76.9 |
| 99.7 | 66.6 | 97.0 | 76.2 |
| 100.0 | 64.5 | 97.1 | 68.0 |
| 100.0 | 73.0 | 94.3 | 49.7 |
| 100.0 | 60.3 | 95.6 | 24.8 |
| 100.0 | 69.6 | 96.2 | 83.9 |
| 100.0 | 67.5 | 97.4 | 78.6 |
| 100.0 | 61.2 | 82.3 | 70.7 |
| 100.0 | 64.6 | 95.6 | 76.9 |
| 100.0 | 62.7 | 97.3 | 91.6 |
| 100.0 | 59.5 | 97.1 | 87.1 |
| 100.0 | 61.4 | 97.4 | 88.0 |
| 100.0 | 65.0 | 95.8 | 79.9 |
| 100.0 | 68.3 | 96.6 | 81.9 |
| 100.0 | 66.1 | 97.2 | 79.2 |
| 99.9 | 70.2 | 96.9 | 72.0 |
| 100.0 | 57.0 | 96.3 | 47.1 |
| 100.0 | 76.5 | 96.0 | 69.3 |
| 100.0 | 80.3 | 97.0 | 65.3 |
| 99.8 | 79.6 | 96.8 | 68.0 |
| 99.8 | 70.4 | 97.1 | 80.8 |
| 100.0 | 67.0 | 97.0 | 85.9 |
| 99.7 | 56.5 | 96.1 | 63.6 |
| 99.9 | 69.4 | 97.1 | 53.9 |
| 99.9 | 64.7 | 96.6 | 68.0 |
| 100.0 | 64.8 | 95.0 | 78.4 |

| | | | |
|---|---|---|---|
| 100.0 | 66.5 | 95.9 | 70.8 |
| 100.0 | 65.8 | 96.9 | 85.2 |
| 99.8 | 64.9 | 96.8 | 83.0 |
| 100.0 | 75.0 | 96.1 | 73.2 |
| 99.9 | 78.2 | 96.8 | 64.1 |
| 100.0 | 65.1 | 93.1 | 59.6 |
| 100.0 | 67.6 | 97.5 | 69.1 |
| 100.0 | 75.7 | 92.8 | 54.0 |
| 100.0 | 64.4 | 97.5 | 74.3 |
| 100.0 | 79.7 | 97.0 | 74.8 |
| 100.0 | 79.0 | 96.7 | 82.1 |
| 100.0 | 77.7 | 96.5 | 81.4 |
| 100.0 | 76.9 | 96.7 | 78.1 |
| 100.0 | 79.3 | 96.7 | 71.4 |
| 100.0 | 60.5 | 96.4 | 82.9 |
| 100.0 | 58.5 | 96.5 | 95.8 |
| 100.0 | 76.9 | 96.7 | 79.2 |
| 100.0 | 78.8 | 96.0 | 72.5 |
| 100.0 | 78.5 | 97.0 | 79.1 |
| 100.0 | 77.9 | 96.8 | 73.5 |
| 99.9 | 56.8 | 96.6 | 71.9 |

; [d]anorthite number is molar 100×[Ca/(Ca+Na+K)]; [e]Plagioclase content from CIPW normalization, normalized to 100 vol% plagioclase + olivine + pyroxene.

Table 6. LA-ICP-MS trace element compositions of Shişr 161 clasts.

| clast | Sph1 | Sph2-accret | Sph2-main | Sph3 | Sph5 | Sph7 | Sph9 | Sph10 |
|---|---|---|---|---|---|---|---|---|
| Lithology | spherule | spherule | spherule | spherule | spherule | spherule | spherule | spherule |
| Na | 2780±192 | 2866±253 | 629±43 | 4341±300 | 4188±289 | 9403±831 | 11853±1047 | 3208±221 |
| K | 858±77 | 49±0.8 | 165±15 | 830±74 | 6020±537 | 9457±158 | 789±13 | 129±12 |
| Sc | 16.9±0.2 | 8.7±0.2 | 9.4±0.1 | 20.2±0.3 | 16.6±0.2 | 25.7±0.6 | 6±0.1 | 9.2±0.13 |
| Ti | 5345±85 | 1121±27 | 592±9 | 5536±88 | 5533±88 | 9985±243 | 638±16 | 1248±20 |
| V | 33.5±0.4 | 13.4±0.2 | 10.2±0.1 | 44.7±0.6 | 32.1±0.4 | 45.3±0.6 | 48.7±0.6 | 14.7±0.2 |
| Cr | 1253±22 | 391±14 | 303±5 | 1614±28 | 1081±19 | 1544±56 | 1438±52 | 503±9 |
| Mn | 859±0.5 | 605±7 | 1756±1 | 1197±0.7 | 809±0.4 | 1134±12 | 1972±22 | 441±0.2 |
| Co | 11.8±0.002 | 13.7±0.4 | 55.7±0.01 | 32.7±0.004 | 10.58±0.001 | 8.4±0.2 | 128±4 | 9.7±0.001 |
| Ni | 6.38±0.03 | 51.7±1.7 | 119±0.5 | 322±1.3 | 68±0.3 | 106±3 | 375±12 | 40±0.2 |
| Cu | 1.65±0.03 | <2.63 | 2.11±0.03 | 14.7±0.2 | 1.62±0.02 | 7.5±0.2 | 10.6±0.3 | 1.89±0.03 |
| Zn | 1.64±0.07 | <2.19 | 8.5±0.3 | 12.3±0.5 | 1.9±0.08 | 6.3±0.2 | <0.71 | 1.74±0.07 |
| Ga | 0.74±0.04 | <1.76 | <0.37 | 4.3±0.3 | 3.55±0.19 | 6.6±0.5 | 7.1±0.5 | 3.5±0.2 |
| Sr | 138±3.8 | 257±9 | 133±4 | 397±11 | 134±4 | 290±10 | 41.1±1.4 | 181±5 |
| Y | 188±12 | 5.2±0.3 | 2.53±0.16 | 151±10 | 183±12 | 289±15 | 2.06±0.11 | 6.6±0.4 |
| Zr | 757±24 | 16.7±0.7 | 3.82±0.12 | 432±14 | 824±26 | 1363±56 | 4.42±0.18 | 19.8±0.6 |
| Nb | 50±1.6 | 0.96±0.02 | 0.61±0.02 | 34.7±1.1 | 49.3±1.6 | 93±2 | 0.25±0.01 | 1.34±0.04 |
| Ba | 475±31 | 23.7±3.1 | 12.8±0.9 | 441±29 | 513±34 | 971±125 | 4.9±0.6 | 19.6±1.3 |
| La | 54±1.6 | 1.25±0.01 | 0.59±0.02 | 43.8±1.3 | 51.8±1.6 | 85.4±0.3 | 0.289±0.001 | 1.5±0.05 |
| Ce | 137±1 | 3.6±0.1 | 1.49±0.01 | 113±1 | 133±1 | 222±6 | 0.96±0.03 | 3.66±0.03 |
| Pr | 19.3±0.2 | 0.43±0.01 | 0.171±0.00 | 15.3±0.1 | 18±0.2 | 30.3±0.9 | 0.108±0.003 | 0.51±0.005 |
| Nd | 84±2 | 2.17±0.01 | 0.78±0.02 | 67.7±1.6 | 79±2 | 128±0.8 | 0.521±0.003 | 2.6±0.1 |
| Sm | 24.4±0.6 | 0.62±0.01 | 0.171±0.00 | 19.3±0.5 | 24±0.6 | 37.5±0.7 | 0.226±0.004 | 0.68±0.02 |
| Eu | 1.64±0.03 | 0.66±0.01 | 0.187±0.00 | 1.69±0.03 | 1.63±0.03 | 2.17±0.03 | 0.181±0.002 | 0.92±0.02 |
| Gd | 29.2±2.1 | 0.73±0.04 | 0.27±0.02 | 22.6±1.6 | 28±2 | 43.8±2.6 | 0.24±0.01 | 0.95±0.07 |
| Tb | 5±0.3 | 0.16±0.01 | 0.045±0.00 | 4.04±0.26 | 4.9±0.3 | 7.6±0.3 | 0.049±0.002 | 0.16±0.01 |
| Dy | 33.4±1.1 | 0.66±0.02 | 0.39±0.01 | 26.4±0.8 | 32.8±1 | 50.6±1.4 | 0.46±0.01 | 1.32±0.04 |
| Ho | 6.9±0.4 | 0.18±0.01 | 0.087±0.00 | 5.6±0.3 | 6.7±0.4 | 11±0.3 | 0.071±0.002 | 0.27±0.02 |
| Er | 20.5±0.5 | 0.76±0.01 | 0.27±0.01 | 16.6±0.4 | 19.7±0.5 | 31.3±0.5 | 0.236±0.004 | 0.7±0.02 |
| Tm | 3±0.1 | 0.111±0.00 | 0.05±0.002 | 2.44±0.08 | 2.88±0.09 | 4.54±0.09 | 0.039±0.001 | 0.099±0.003 |
| Yb | 18.5±0.2 | 0.6±0.01 | 0.4±0.01 | 15.6±0.2 | 18.6±0.2 | 29.4±0.7 | 0.275±0.006 | 0.76±0.01 |
| Lu | 2.58±0.11 | 0.09±0.01 | 0.068±0.00 | 2.2±0.1 | 2.6±0.1 | 4.28±0.32 | 0.034±0.003 | 0.099±0.004 |
| Hf | 18.3±1.3 | 0.3±0.01 | 0.12±0.01 | 11.6±0.8 | 20.2±1.5 | 30.7±1.3 | 0.162±0.01 | 0.51±0.04 |
| Ta | 2.2±0.03 | 0.054±0.00 | 0.016±0.00 | 1.42±0.02 | 2.22±0.03 | 3.72±0.13 | 0.03±0.001 | 0.081±0.001 |
| Pb | 2.2±0.3 | 0.47±0.01 | 0.83±0.11 | 1.92±0.25 | 2.34±0.31 | 5.17±0.16 | 0.033±0.001 | 0.18±0.02 |
| Th | 10.6±1.2 | 0.16±0.01 | 0.08±0.01 | 6.36±0.69 | n.d. | 17.3±1.4 | 0.038±0.003 | 0.21±0.02 |
| beam Ø [µm] | 90 | 50 | 90 | 90 | 90 | 50 | 50 | 90 |
| n analyses | 1 | 1 | 1 | 3 | 1 | 1 | 1 | 1 |

All concentrations in ppm; 1-sigma errors given as relative standard deviations of the average of repeated analyses of USGS standard BIR-1

This is a preprint, the final version is subject to change, of the American Mineralogist (MSA)
Cite as Authors (Year) Title. American Mineralogist, in press.
(DOI will not work until issue is live.) DOI: http://dx.doi.org/10.2138/am.2014.4837 

| | | | | | | | | | |
|---|---|---|---|---|---|---|---|---|---|
| 160 | 8 | 18 | 23 | 27 | 36 | 43 | 50 | 63 | 74 |
| mono-crystalline | crystallized melt | crystallized melt | crystallized melt | crystallized melt | crystallized melt | crystallized melt | crystallized melt | crystallized melt | crystallized melt |
| 29822±2850 | 2729±261 | 2233±213 | 1986±190 | 1771±169 | 2145±205 | 1976±189 | 2883±276 | 2590±248 | 1724±165 |
| 2226±600 | 90±24 | 143±39 | 111±30 | 49.2±13.3 | 84±23 | 86±23 | 139±38 | 235±63 | 152±41 |
| 0.51±0.02 | 17.8±0.7 | 16.1±0.6 | 35.7±1.4 | 6.8±0.3 | 11.8±0.5 | 9.2±0.4 | 9.2±0.4 | 41±1.6 | 43.2±1.7 |
| 499±2 | 1192±6 | 2012±10 | 1999±10 | 745±4 | 1142±5 | 995±5 | 1087±5 | 3207±15 | 3779±18 |
| 4.18±0.04 | 36.5±0.4 | 40.7±0.4 | 134±1 | 17.4±0.2 | 27.5±0.3 | 21.5±0.2 | 22.5±0.2 | 83±1 | 75±1 |
| 13.3±0.4 | 1004±33 | 1158±38 | 2667±88 | 580±19 | 955±31 | 580±19 | 666±22 | 1515±50 | 2081±68 |
| 313±1 | 1468±3 | 836±2 | 1506±3 | 472±1 | 491±1 | 557±1 | 522±1 | 1763±4 | 1389±3 |
| 1.05±0.02 | 35.1±0.5 | 17.3±0.3 | 21.3±0.3 | 14.1±0.2 | 10.5±0.2 | 18.1±0.3 | 10.6±0.2 | 18±0.3 | 24.5±0.4 |
| 9.3±0.1 | 63.9±0.7 | 89±1 | 7.8±0.1 | 32.3±0.4 | 32±0.4 | 87±1 | 54±1 | 20.1±0.2 | 140±2 |
| <0.87 | 2.44±0.05 | 3.46±0.07 | 2.44±0.05 | 2.62±0.05 | 2.31±0.05 | 3±0.1 | 2.5±0.1 | 3.15±0.06 | 5.3±0.1 |
| 3.4±0.1 | 5.74±0.12 | 5.3±0.1 | 2.55±0.05 | 3.22±0.07 | 2.68±0.06 | 4.1±0.1 | 3.1±0.1 | 4.8±0.1 | 8.3±0.2 |
| 15.5±0.9 | 2.75±0.15 | 2.55±0.14 | 2.08±0.11 | 2.06±0.11 | 2.23±0.12 | 2.21±0.12 | 2.82±0.15 | 3±0.2 | 2.05±0.11 |
| 940±35 | 184±7 | 428±16 | 114±4 | 132±5 | 134±5 | 132±5 | 184±7 | 150±6 | 136±5 |
| 4.94±0.04 | 11.1±0.1 | 9.1±0.1 | 6.8±0.1 | 3.34±0.03 | 5.5±0.1 | 4.42±0.04 | 6.1±0.1 | 17.1±0.1 | 26.2±0.2 |
| 0.8±0.03 | 18.6±0.7 | 26.7±1 | 13.8±0.5 | 8.7±0.3 | 11.8±0.4 | 11.9±0.4 | 19.9±0.7 | 14.2±0.5 | 75±3 |
| 0.01±0.004 | 0.54±0.02 | 1.6±0.1 | 0.63±0.03 | 0.31±0.01 | 0.61±0.03 | 0.56±0.03 | 1.9±0.1 | 1.6±0.1 | 2±0.1 |
| 1741±113 | 29.3±1.9 | 99±6 | 17.2±1.1 | 14.8±1 | 12±1 | 40.3±2.6 | 21.4±1.4 | 28.1±1.8 | 20.4±1.3 |
| 12.9±0.1 | 2.64±0.02 | 1.77±0.01 | 0.88±0.01 | 0.64±0.01 | 0.8±0.01 | 0.62±0.01 | 1.3±0.01 | 1.47±0.01 | 1.65±0.01 |
| 23.7±0.3 | 6.94±0.08 | 4.98±0.06 | 2.29±0.03 | 1.73±0.02 | 2.19±0.02 | 1.69±0.02 | 3.34±0.04 | 4.5±0.1 | 6.39±0.07 |
| 2.77±0.12 | 1.00±0.04 | 0.73±0.03 | 0.33±0.01 | 0.25±0.01 | 0.32±0.01 | 0.26±0.01 | 0.46±0.02 | 0.68±0.03 | 1.15±0.05 |
| 10±0.1 | 4.7±0.1 | 3.31±0.05 | 1.55±0.02 | 1.11±0.02 | 1.6±0.02 | 1.22±0.02 | 2.13±0.03 | 3.6±0.1 | 6.72±0.09 |
| 2.29±0.02 | 1.35±0.01 | 1.04±0.01 | 0.54±0.01 | 0.36±0.004 | 0.6±0.01 | 0.47±0.01 | 0.73±0.01 | 1.3±0.01 | 2.8±0.03 |
| 6.36±0.04 | 0.8±0.01 | 0.71±0.004 | 0.414±0.002 | 0.609±0.004 | 0.557±0.003 | 0.528±0.003 | 0.80±0.01 | 0.67±0.004 | 0.45±0.003 |
| 1.54±0.02 | 1.71±0.03 | 1.33±0.02 | 0.74±0.01 | 0.51±0.01 | 0.71±0.01 | 0.63±0.01 | 0.79±0.01 | 1.91±0.01 | 3.69±0.06 |
| 0.214±0.003 | 0.3±0.004 | 0.24±0.004 | 0.138±0.002 | 0.01±0.001 | 0.135±0.002 | 0.106±0.002 | 0.138±0.00 | 0.37±0.01 | 0.68±0.01 |
| 1.04±0.01 | 1.86±0.01 | 1.58±0.01 | 1.03±0.01 | 0.56±0.004 | 1.02±0.01 | 0.76±0.01 | 1.02±0.02 | 2.79±0.02 | 4.72±0.04 |
| 0.192±0.002 | 0.422±0.005 | 0.35±0.004 | 0.24±0.003 | 0.134±0.001 | 0.205±0.002 | 0.168±0.002 | 0.247±0.00 | 0.6±0.01 | 0.97±0.01 |
| 0.38±0.01 | 1.30±0.03 | 1.00±0.02 | 0.75±0.02 | 0.37±0.01 | 0.58±0.01 | 0.51±0.01 | 0.68±0.02 | 1.94±0.04 | 2.87±0.06 |
| 0.056±0.001 | 0.20±0.004 | 0.16±0.004 | 0.126±0.003 | 0.05±0.001 | 0.09±0.002 | 0.066±0.001 | 0.1±0.002 | 0.3±0.01 | 0.41±0.01 |
| 0.33±0.01 | 1.3±0.04 | 1.04±0.04 | 0.91±0.03 | 0.35±0.01 | 0.6±0.02 | 0.47±0.02 | 0.74±0.03 | 2±0.1 | 2.6±0.1 |
| 0.03±0.001 | 0.18±0.004 | 0.15±0.003 | 0.13±0.003 | 0.054±0.001 | 0.083±0.002 | 0.064±0.001 | 0.093±0.00 | 0.28±0.01 | 0.35±0.01 |
| 0.031±0.002 | 0.55±0.03 | 0.74±0.04 | 0.39±0.02 | 0.24±0.01 | 0.3±0.02 | 0.32±0.02 | 0.58±0.03 | 0.58±0.03 | 1.9±0.1 |
| <0.00095 | 0.05±0.0001 | 0.086±0.0003 | 0.035±0.0001 | 0.02±0.0001 | 0.042±0.000 | 0.032±0.0001 | 0.101±0.00 | 0.073±0.00 | 0.107±0.00 |
| 0.55±0.001 | 0.37±0.001 | 0.45±0.001 | 0.185±0.001 | 0.584±0.002 | 0.086±0.000 | 0.114±0.0003 | 0.155±0.00 | 0.143±0.00 | 0.33±0.001 |
| <0.0153 | 0.43±0.04 | 0.42±0.04 | 0.102±0.009 | 0.09±0.01 | 0.11±0.01 | 0.11±0.01 | 0.26±0.02 | 0.32±0.03 | 0.55±0.05 |
| 90 | 90 | 90 | 90 | 90 | 90 | 90 | 90 | 90 | 90 |
| 1 | 6 | 5 | 4 | 5 | 3 | 3 | 3 | 4 | 3 |

; [a] MR-modaly recombined values, relative standard deviations of measurements on BIR-1 given as 3-sigma errors to reflect reltaively higher uncerta

| 118 | 156 | 2 | 6 | 53 | 59 | 81 | 34 | 5[a] | 54[a] |
|---|---|---|---|---|---|---|---|---|---|
| crystallized melt | crystallized melt | vitrophyre melt | vitrophyre melt | vitrophyre melt | vitrophyre melt | vitrophyre melt | Mg-cumulate | Mg-cumulate | Mg-cumulate |
| 2891±276 | 2508±240 | 2117±202 | 3073±294 | 2229±213 | 1882±180 | 2257±216 | 1860±164 | 2750±729 | 2412±639 |
| 159±43 | 137±37 | 174±47 | 136±37 | 142±38 | 69±19 | 114±31 | 143±2 | 59±3 | 43±2.1 |
| 21.7±0.8 | 47.2±1.8 | 18.2±0.7 | 8.7±0.3 | 24.8±1 | 5.3±0.2 | 23.6±0.9 | 25±0.6 | 8.5±0.6 | 6.3±0.5 |
| 2386±11 | 4601±22 | 1781±9 | 1237±6 | 2502±12 | 800±4 | 2208±11 | 2900±71 | 961±70 | 699±51 |
| 34.5±0.4 | 93.3±1 | 49.3±0.5 | 16.5±0.2 | 72±1 | 13.6±0.1 | 60.4±0.6 | 67±0.9 | 20.8±0.8 | 24.1±1 |
| 748±25 | 2283±75 | 1288±42 | 530±17 | 1761±58 | 472±16 | 1565±51 | 1802±66 | 1007±110 | 749±82 |
| 821±2 | 891±2 | 790±2 | 439±1 | 1194±2 | 389±1 | 990±2 | 1408±15 | 365±12 | 379±12 |
| 14.4±0.2 | 9.7±0.1 | 17.9±0.3 | 10.8±0.2 | 24.7±0.4 | 13.9±0.2 | 18.1±0.3 | 29±0.8 | 8±0.7 | 7.6±0.7 |
| 63±1 | 12.7±0.1 | 62.5±0.7 | 63.3±0.7 | 53.5±0.6 | 58.2±0.7 | 42.2±0.5 | 60±2 | 43±4.2 | 16.3±1.6 |
| 3.2±0.1 | 1.08±0.02 | 3.6±0.1 | 2.74±0.05 | 4.22±0.1 | 1.47±0.03 | 3.5±0.1 | 3±0.1 | 3.32±0.28 | 3.1±0.3 |
| 3.4±0.1 | 4.4±0.1 | 4.1±0.1 | 1.77±0.04 | 4.1±0.1 | 1.39±0.03 | 3.4±0.1 | 11±0.3 | 4.62±0.4 | 4.5±0.4 |
| 3.1±0.2 | 2.66±0.15 | 2.24±0.12 | 4.37±0.24 | 2.58±0.14 | 1.8±0.1 | 2.9±0.2 | 2±0.1 | 3.32±0.68 | 2.7±0.6 |
| 199±7 | 1061±39 | 164±6 | 163±6 | 160±6 | 181±7 | 121±4 | 182±6 | 596±61 | 180±18 |
| 10.1±0.1 | 35.3±0.3 | 6.5±0.1 | 9.4±0.1 | 8.2±0.1 | 3.87±0.03 | 8.4±0.1 | 9.9±0.5 | 3.5±0.5 | 3.3±0.5 |
| 25.2±0.9 | 103±4 | 13.5±0.5 | 34.2±1.3 | 16.5±0.6 | 11.9±0.4 | 17.4±0.7 | 26±1.1 | 8.7±1.1 | 13±1.6 |
| 1.9±0.1 | 0.48±0.02 | 0.68±0.03 | 2.02±0.09 | 0.86±0.04 | 0.69±0.03 | 0.83±0.04 | 0.46±0.01 | 0.28±0.02 | 0.44±0.03 |
| 28.3±1.8 | 62±4 | 18.5±1.2 | 29.8±1.9 | 16.8±1.1 | 16.3±1.1 | 14±10.9 | 23±3 | 23.8±9.2 | 16.7±6.5 |
| 1.21±0.01 | 1.66±0.01 | 0.77±0.01 | 2.37±0.02 | 0.88±0.01 | 0.91±0.01 | 0.97±0.01 | 0.54±0.002 | 0.8±0.01 | 0.81±0.01 |
| 3.36±0.04 | 6.8±0.1 | 1.98±0.02 | 5.9±0.1 | 2.39±0.03 | 2.29±0.03 | 2.4±0.03 | 1.86±0.05 | 2.16±0.18 | 2.31±0.19 |
| 0.49±0.02 | 1.39±0.06 | 0.3±0.01 | 0.85±0.04 | 0.37±0.02 | 0.31±0.01 | 0.35±0.02 | 0.31±0.01 | 0.3±0.03 | 0.32±0.03 |
| 2.57±0.04 | 8.3±0.1 | 1.51±0.02 | 3.85±0.05 | 1.81±0.03 | 1.52±0.02 | 1.92±0.03 | 1.7±0.01 | 1.33±0.03 | 1.53±0.03 |
| 0.92±0.01 | 3.65±0.04 | 0.47±0.01 | 1.11±0.01 | 0.58±0.01 | 0.4±0.004 | 0.55±0.01 | 0.72±0.01 | 0.42±0.02 | 0.43±0.02 |
| 0.81±0.01 | 0.66±0.004 | 0.533±0.00 | 0.84±0.01 | 0.585±0.00 | 0.94±0.01 | 0.62±0.004 | 0.49±0.01 | 0.75±0.03 | 0.63±0.03 |
| 1.2±0.02 | 5.2±0.1 | 0.77±0.01 | 1.4±0.02 | 0.93±0.01 | 0.5±0.01 | 1±0.02 | 1.1±0.07 | 0.57±0.1 | 0.59±0.11 |
| 0.24±0.004 | 0.99±0.02 | 0.148±0.00 | 0.261±0.00 | 0.18±0.003 | 0.1±0.002 | 0.16±0.002 | 0.2±0.01 | 0.1±0.01 | 0.09±0.01 |
| 1.63±0.01 | 6.5±0.05 | 1.06±0.01 | 1.77±0.01 | 1.31±0.01 | 0.69±0.01 | 1.34±0.01 | 1.6±0.05 | 0.64±0.06 | 0.68±0.06 |
| 0.35±0.004 | 1.31±0.01 | 0.234±0.00 | 0.37±0.004 | 0.29±0.003 | 0.14±0.002 | 0.31±0.003 | 0.36±0.01 | 0.15±0.01 | 0.14±0.01 |
| 1.17±0.03 | 3.8±0.1 | 0.73±0.02 | 1.13±0.03 | 0.97±0.02 | 0.37±0.01 | 0.98±0.02 | 1.16±0.02 | 0.46±0.02 | 0.43±0.02 |
| 0.17±0.004 | 0.49±0.01 | 0.109±0.00 | 0.168±0.00 | 0.14±0.003 | 0.06±0.001 | 0.14±0.003 | 0.18±0.004 | 0.07±0.004 | 0.06±0.004 |
| 1.11±0.04 | 3.08±0.12 | 0.8±0.03 | 0.99±0.04 | 0.98±0.04 | 0.45±0.02 | 0.96±0.04 | 1.2±0.03 | 0.46±0.03 | 0.35±0.02 |
| 0.18±0.004 | 0.43±0.01 | 0.116±0.00 | 0.141±0.00 | 0.16±0.004 | 0.06±0.001 | 0.16±0.004 | 0.2±0.02 | 0.08±0.02 | 0.06±0.01 |
| 0.69±0.04 | 2.61±0.15 | 0.4±0.02 | 0.85±0.05 | 0.5±0.03 | 0.29±0.02 | 0.51±0.03 | 0.66±0.03 | 0.3±0.04 | 0.38±0.05 |
| 0.128±0.00 | 0.02±0.000 | 0.036±0.00 | 0.01±0.000 | 0.046±0.00 | 0.04±0.000 | 0.07±0.0002 | 0.05±0.002 | 0.04±0.004 | 0.05±0.01 |
| 0.173±0.00 | 0.25±0.001 | 0.29±0.001 | 0.156±0.00 | 0.14±0.000 | 0.11±0.000 | 0.07±0.0002 | 0.28±0.01 | 0.14±0.01 | 0.14±0.01 |
| 0.25±0.02 | 0.34±0.03 | 0.10±0.01 | 0.41±0.04 | 0.11±0.01 | 0.14±0.01 | 0.13±0.01 | 0.17±0.014 | 0.07±0.017 | 0.1±0.02 |
| 90 | 90 | 90 | 90 | 90 | 90 | 90 | 50 | 50 | 50 |
| 3 | 2 | 3 | 3 | 3 | 3 | 2 | 5 | [a]MR | [a]MR |

ainty; n.d.-not detected.

26[a]

Fe-cumulate

2567±680
146±7
21±1.5
5725±418
34±1.4
1777±194
803±26
7.2±0.6
10.1±1
3±0.3
4.2±0.4
1.71±0.35
460±47
8.8±1.4
11.2±1.4
0.09±0.01
102±39
0.36±0.004
1.3±0.11
0.21±0.02
1.29±0.02
0.58±0.03
0.61±0.03
1.02±0.18
0.21±0.02
1.4±0.1
0.33±0.03
1.12±0.05
0.17±0.01
1.19±0.08
0.18±0.04
0.3±0.04
0.023±0.002
0.54±0.05
0.04±0.01

50
[a]MR

Table 7. Equilibrium crystallization MELTS modeling results.

| Model inputs | | | olivine | | low-Ca pyroxene | | | |
|---|---|---|---|---|---|---|---|---|
| FC % | DU % | GN % | Mg# | wt% | En | Fs | Wo | Mg# |
| 100 | 0 | 0 | 70 | 4.9 | 62 | 25 | 14 | 71 |
| 95 | 5 | 0 | **75** | **9.2** | 65 | 22 | 13 | 75 |
| 90 | 10 | 0 | **77** | **13.8** | 67 | **20** | 13 | 77 |
| 85 | 15 | 0 | 80 | **17.9** | 69 | **19** | 11 | **78** |
| 95 | 0 | 5 | 70 | **5.1** | 61 | 25 | 14 | 71 |
| 90 | 0 | 10 | 69 | 4.6 | 61 | 25 | 14 | 71 |
| 85 | 0 | 15 | 69 | 3.9 | 61 | 25 | 14 | 71 |
| 34 | 33 | 33 | 82 | 32.3 | 70 | **18** | 13 | **80** |
| Shişr 161 Mg-cumulates | | | **74-79** | **5-19** | **74-79** | **17-21** | **2-5** | **78-82** |
| Shişr 161 Fe-cumulates | | | 46-56 | 1-8 | 47-57 | 38-43 | 5-15 | 53-60 |

FC is the average composition of the feldspathic upper crust based on lunar meteorites after Korotev et al. (2003), DU is dunite 72415 (Gast

| | Modeling outputs | | | | | | | |
|---|---|---|---|---|---|---|---|---|
| | | | high-Ca pyroxene | | | feldspar | | final T |
| wt% | En | Fs | Wo | Mg# | wt% | An | wt% | °C |
| **14.8** | **47** | 15 | 38 | 77 | **1.6** | **96** | 77.3 | 1130 |
| **14.5** | **48** | 13 | 39 | 80 | **1.5** | **96** | **73.9** | 1140 |
| **11.1** | **50** | 12 | 39 | 82 | **3** | **96** | **71** | 1140 |
| **12.6** | **49** | **10** | **41** | **83** | **2.1** | **96** | **66.5** | 1130 |
| **15.7** | **47** | 15 | 38 | 76 | **2.8** | **95** | **75.1** | 1130 |
| **18.4** | **47** | 15 | 38 | 76 | **2.5** | **95** | **73.1** | 1130 |
| **20.9** | **47** | 15 | 38 | 76 | **3.1** | **95** | **70.6** | 1130 |
| **21** | 53 | 11 | 37 | **84** | **6** | 90 | 38.7 | 1160 |
| **5-22** | **47-50** | **7-10** | **41-45** | **83-87** | **0-8** | **95-98** | **66-77** | n.a. |
| 1-14 | 39-47 | 17-27 | 30-42 | 59-72 | 3-19 | 95-97 | 65-94 | n.a. |

et al. 1973), GN is gabbronorite 61224,6 (Marvin and Warren 1980); residual is the remaining liquid at the final temperature; Mg# is molar (M

This is a preprint, the final version is subject to change, of the American Mineralogist (MSA)
Cite as Authors (Year) Title. American Mineralogist, in press.
(DOI will not work until issue is live.) DOI: http://dx.doi.org/10.2138/am.2014.4837


| residual |
|---|
| wt% |
| 0.72 |
| 0.25 |
| 0.77 |
| 0.19 |
| 0.88 |
| 0.96 |
| 0.89 |
| 0.86 |
| n.a. |
| n.a. |

Mg/(Mg+Fe))×100; En is molar (Mg/(Mg+Fe+Ca))×100, Fs is molar (Fe/(Fe+Mg+Ca))×100, Wo is molar (Ca/(Ca+Mg+Fe))×100; An is mola ar (Ca/(Ca+Na+K))×100; n.a. is not applicable; bold face fonts indicate values fall within the range observed in Shişr 161 magnesian cumulat e clasts. Spinel is an accessory in all model runs with compositions and abundances that do not match observed values in Shişr 161 magnesia n cumulate clasts.

Table 8. Fractional crystallization MELTS modeling results.

| Model input | | | Spinel anorthosite 1390-1250°C | Anorthositic troctolite 1260-1190°C | Spinel gabbronorite 1190-1020°C | (Olivine) norite 1040-980°C |
|---|---|---|---|---|---|---|
| $FC_{100}$ | mafic phases | wt% | 0.45 | 7.7 | 11 | 0.7 |
| $FC_{100}$ | plagioclase | wt% | 52.7 | 16.7 | 7 | 0.4 |
| $FC_{100}$ | avg. ρ liquid | $g/cm^3$ | 2.69 | 2.74 | 2.77 | 2.64 |
| $FC_{95}DU_5$ | mafic phases | wt% | 0.8 | 11.6 | 10.1 | 1.4 |
| $FC_{95}DU_5$ | plagioclase | wt% | 39 | 26.3 | 6.7 | 0.8 |
| $FC_{95}DU_5$ | avg. ρ liquid | $g/cm^3$ | 2.69 | 2.74 | 2.76 | 2.64 |
| $FC_{90}DU_{10}$ | mafic phases | wt% | 1 | 14.8 | 11.8 | 0.7 |
| $FC_{90}DU_{10}$ | plagioclase | wt% | 24.2 | 36.2 | 7.9 | 0.4 |
| $FC_{90}DU_{10}$ | avg. ρ liquid | $g/cm^3$ | 2.69 | 2.73 | 2.76 | 2.68 |
| $FC_{85}DU_{15}$ | mafic phases | wt% | 1.7 | 18.1 | 12.9 | 0.4 |
| $FC_{85}DU_{15}$ | plagioclase | wt% | 11.4 | 43.8 | 8.4 | 0.3 |
| $FC_{85}DU_{15}$ | avg. ρ liquid | $g/cm^3$ | 2.70 | 2.72 | 2.74 | 2.64 |
| $FC_{95}GN_5$ | mafic phases | wt% | 0.8 | 11.6 | 10.1 | 1.4 |
| $FC_{95}GN_5$ | plagioclase | wt% | 39 | 26.3 | 6.7 | 0.8 |
| $FC_{95}GN_5$ | avg. ρ liquid | $g/cm^3$ | 2.69 | 2.74 | 2.76 | 2.64 |
| $FC_{90}GN_{10}$ | mafic phases | wt% | 0.4 | 7.6 | 13.9 | 1.8 |
| $FC_{90}GN_{10}$ | plagioclase | wt% | 45.3 | 17.5 | 9.7 | 0.8 |
| $FC_{90}GN_{10}$ | avg. ρ liquid | $g/cm^3$ | 2.69 | 2.74 | 2.77 | 2.67 |
| $FC_{85}GN_{15}$ | mafic phases | wt% | 0.3 | 7.8 | 17.3 | 1 |
| $FC_{85}GN_{15}$ | plagioclase | wt% | 41.5 | 18.1 | 11.4 | 2.53 |
| $FC_{85}GN_{15}$ | avg. ρ liquid | $g/cm^3$ | 2.69 | 2.73 | 2.72 | 2.51 |
| $FC_{34}DU_{33}GN_{33}$ | mafic phases | wt% | 0.6* | 35.4† | 18.9# | 1.8 |
| $FC_{34}DU_{33}GN_{33}$ | plagioclase | wt% | – | 24.5§ | 12.9 | 0.8 |
| $FC_{34}DU_{33}GN_{33}$ | avg. ρ liquid | $g/cm^3$ | 2.72 | 2.72 | 2.76 | 2.66 |

Data shows wt% of each phase present at the end of the indicated temperature intervals and the densities of the residual melt at that point. Te emperature ranges vary ~10-30°C for the different melt compositions, except where indicated. *T range is 1400-1250 °C; †T range is 1450-1

200 °C; [§]T range is 1240-1200 °C; [#]T range is 1190-1050 °C; note that the main mass of plagioclase has a density of 2.70 g/cm$^3$, except in F

$C_{34}DU_{33}GN_{33}$, where it has a density of 2.69 g/cm$^3$; 3.3 to 4.7 wt% liquid remained after the model runs stopped at ~1000°C.


Wittmann et al. fig. 1

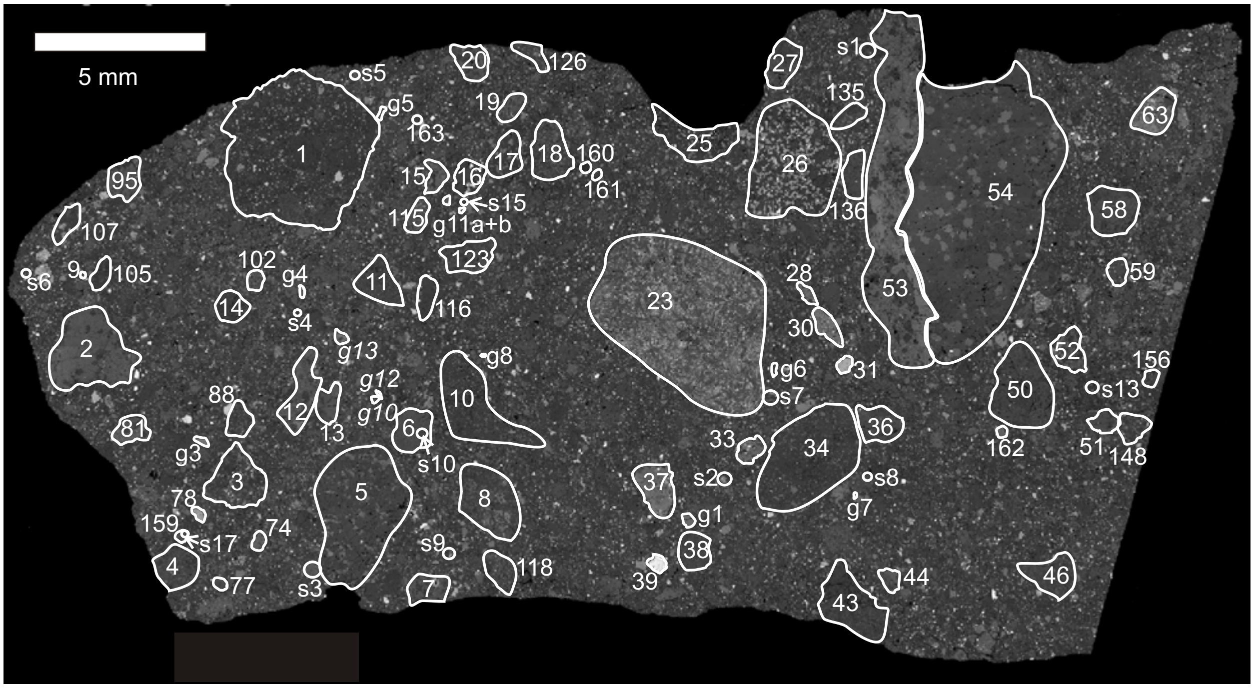


Wittmann et al. fig. 2

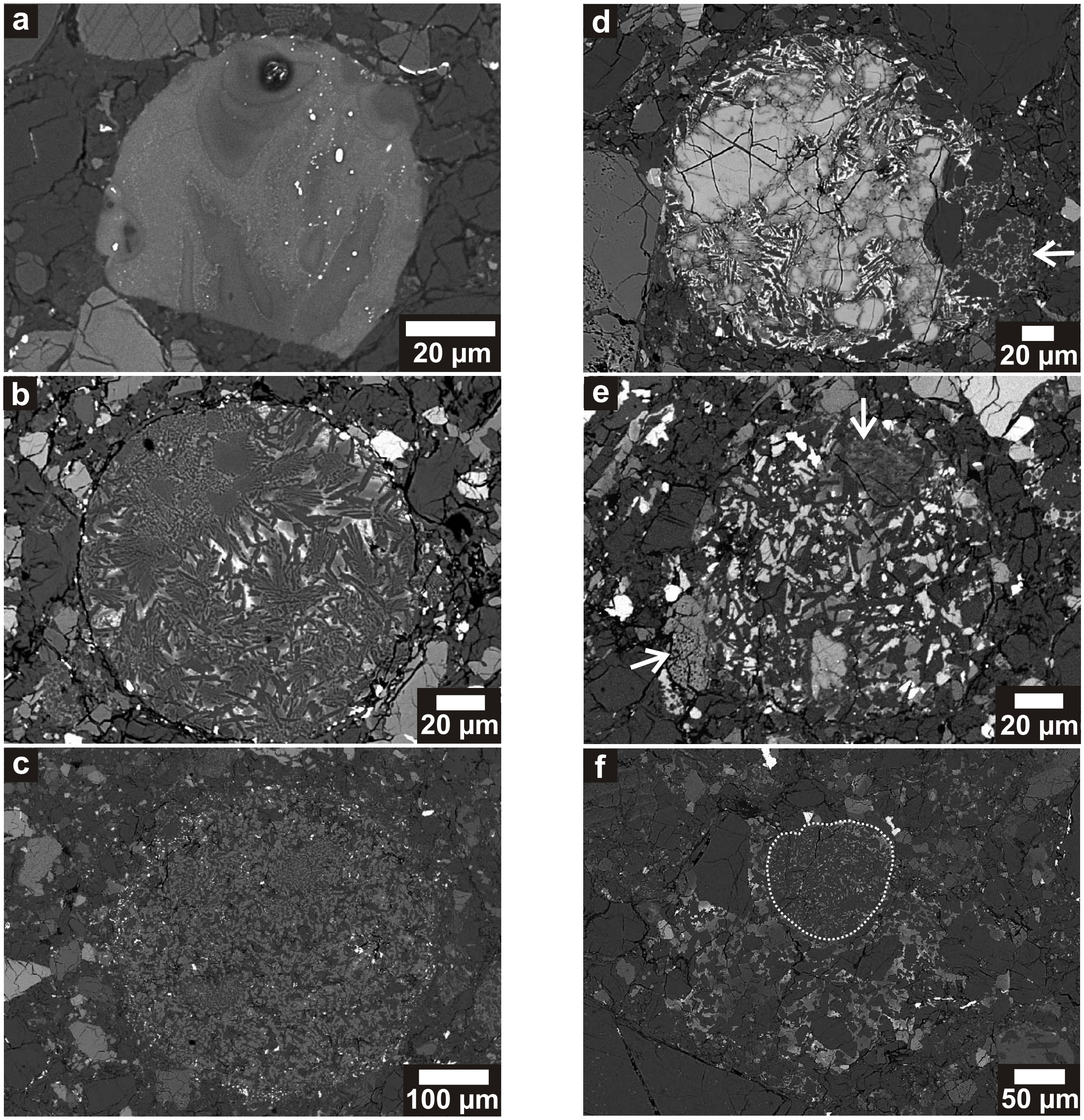


Wittmann et al. fig. 3

This is a preprint, the final version is subject to change, of the American Mineralogist (MSA)
Cite as Authors (Year) Title. American Mineralogist, in press.
(DOI will not work until issue is live.) DOI: http://dx.doi.org/10.2138/am.2014.4837 

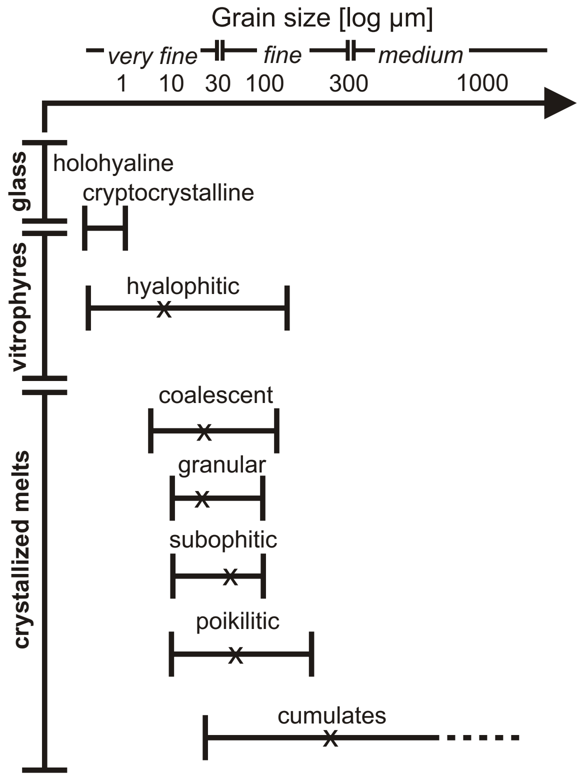


Wittmann et al. fig. 4

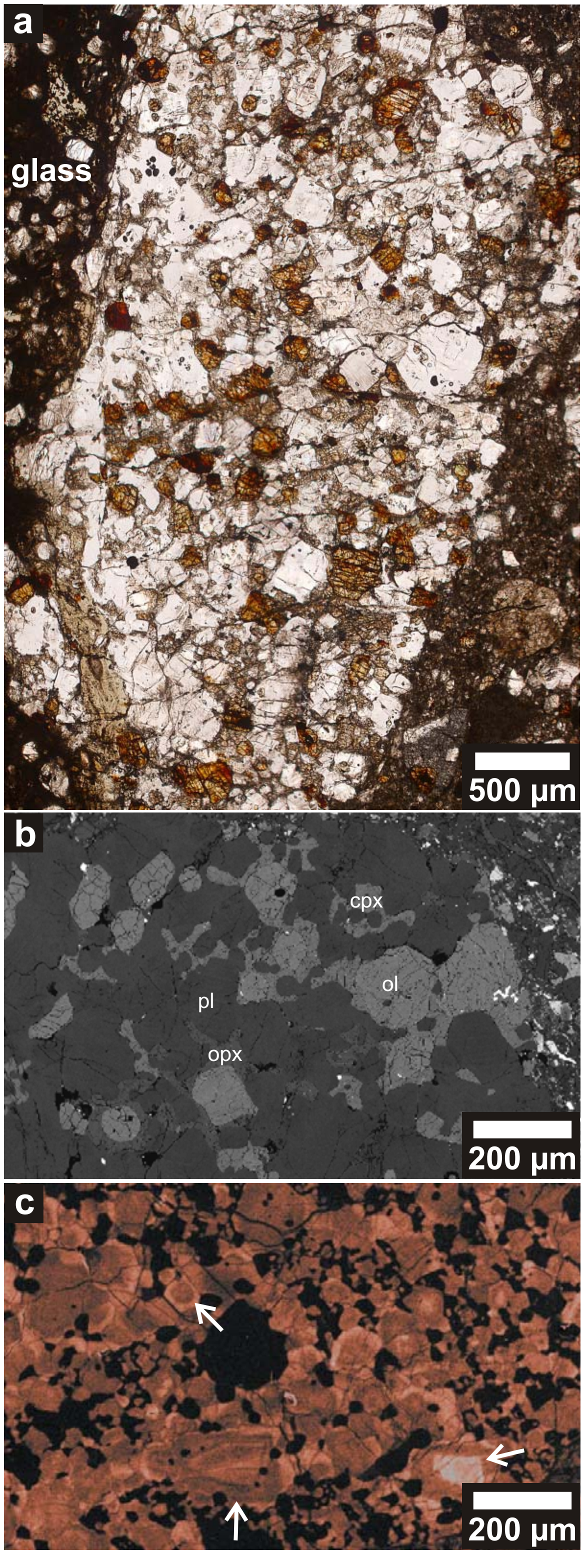


Wittmann et al. fig. 5

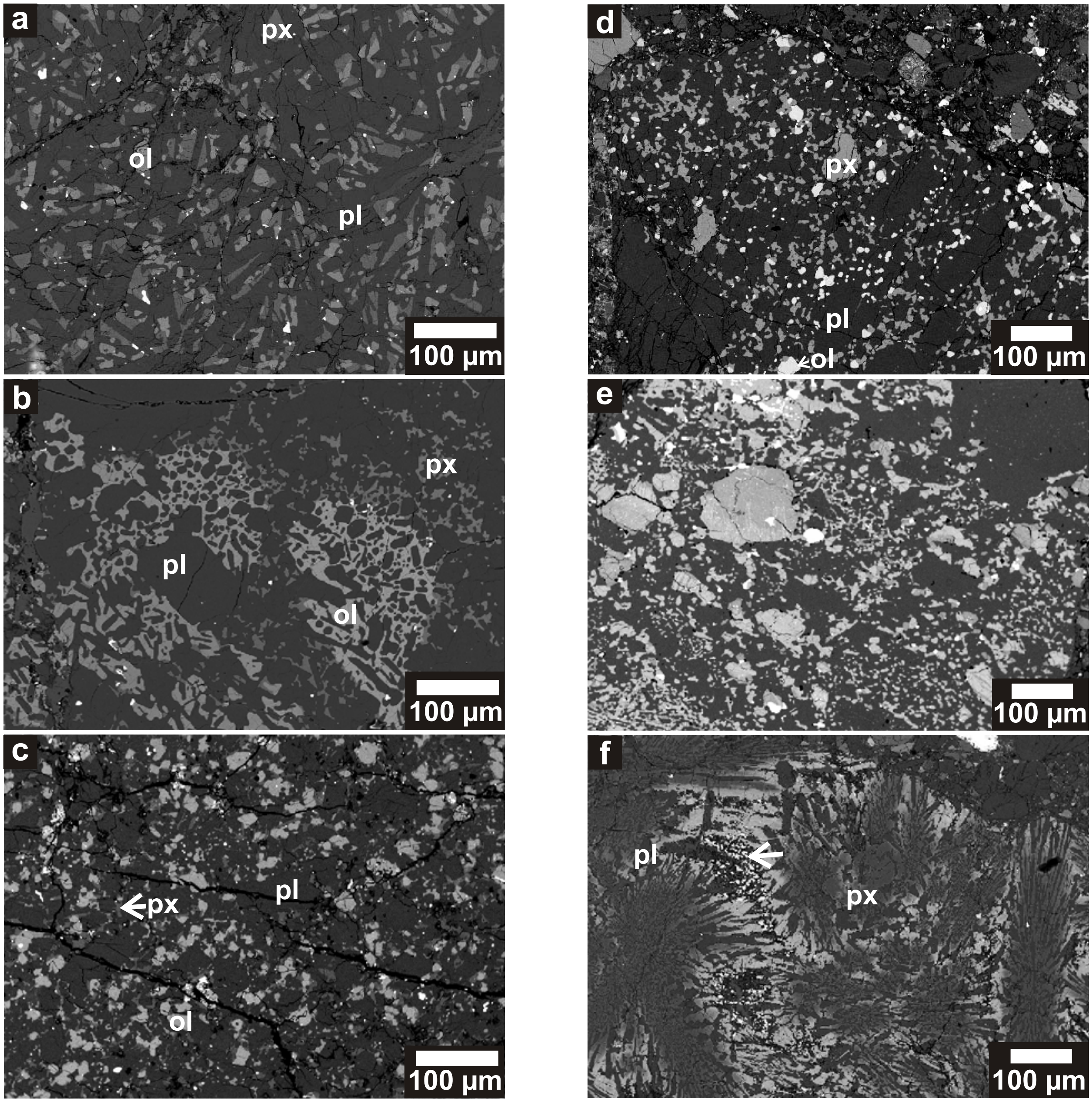


Wittmann et al. fig. 6

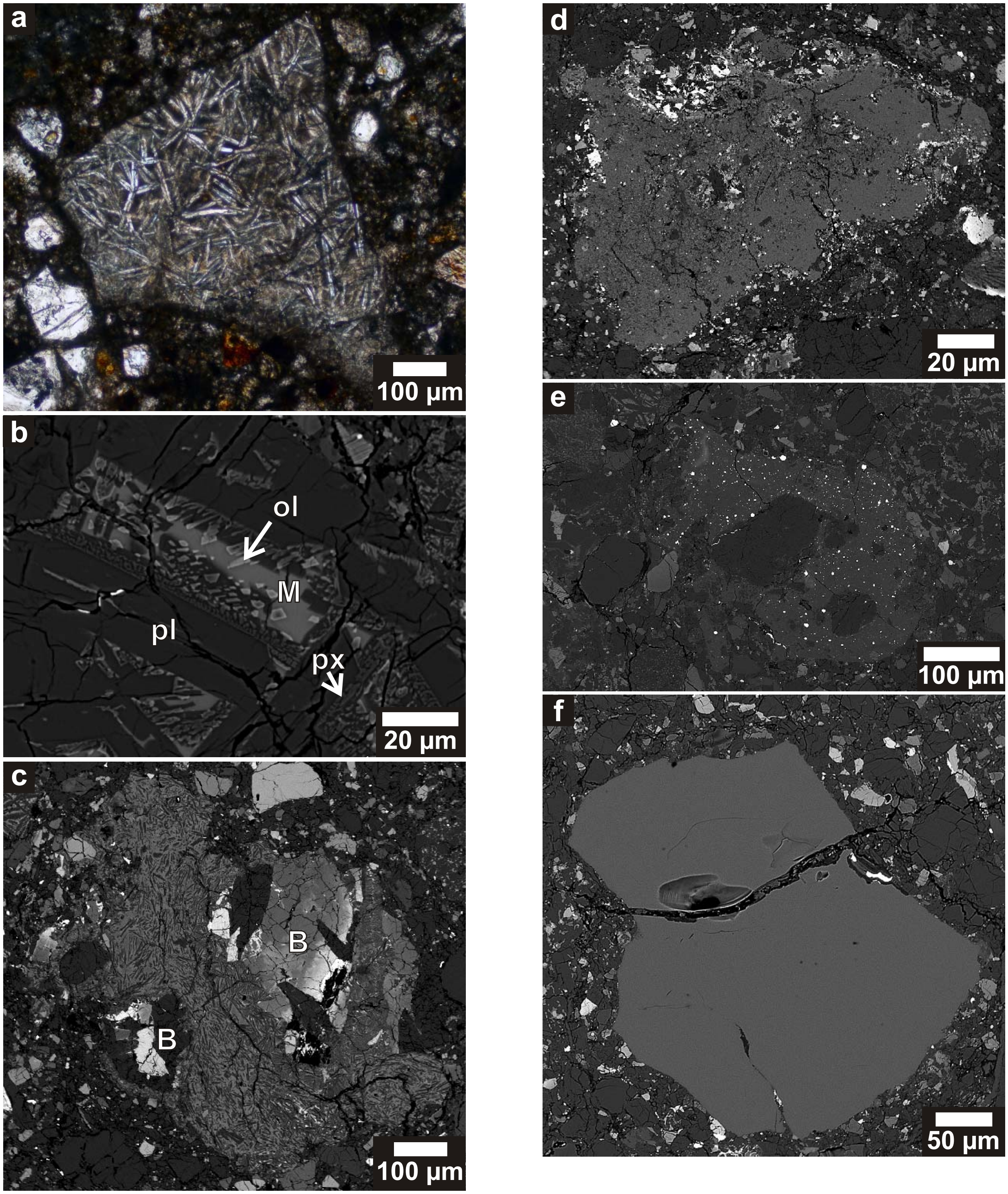


Wittmann et al. fig. 7

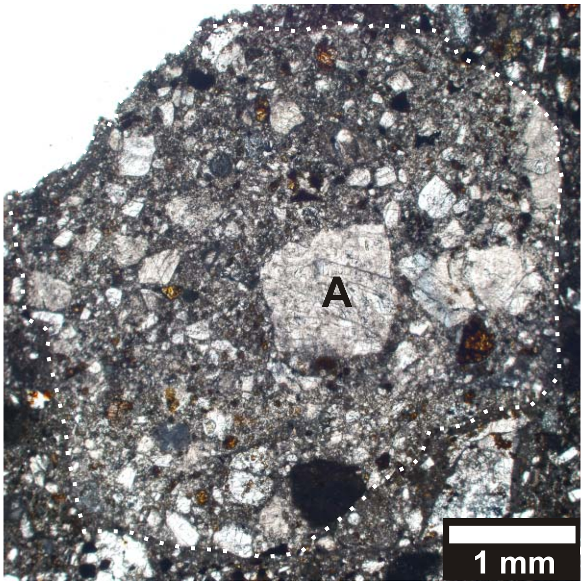


Wittmann et al. fig. 8

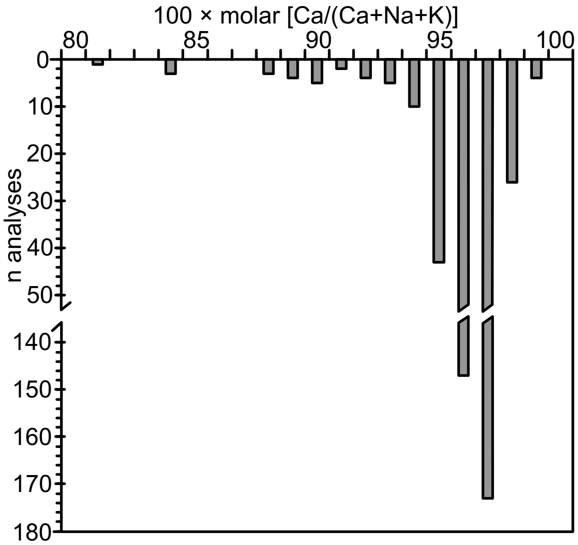


Wittmann et al. fig. 9

This is a preprint, the final version is subject to change, of the American Mineralogist (MSA)
Cite as Authors (Year) Title. American Mineralogist, in press.
(DOI will not work until issue is live.) DOI: http://dx.doi.org/10.2138/am.2014.4837 

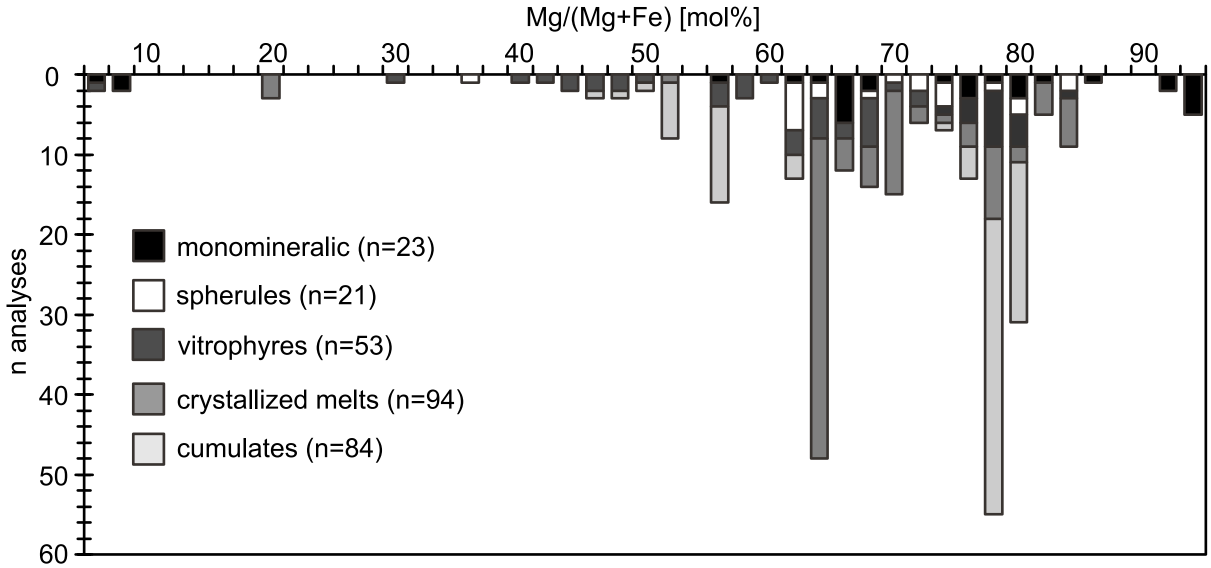


Wittmann et al. fig. 10

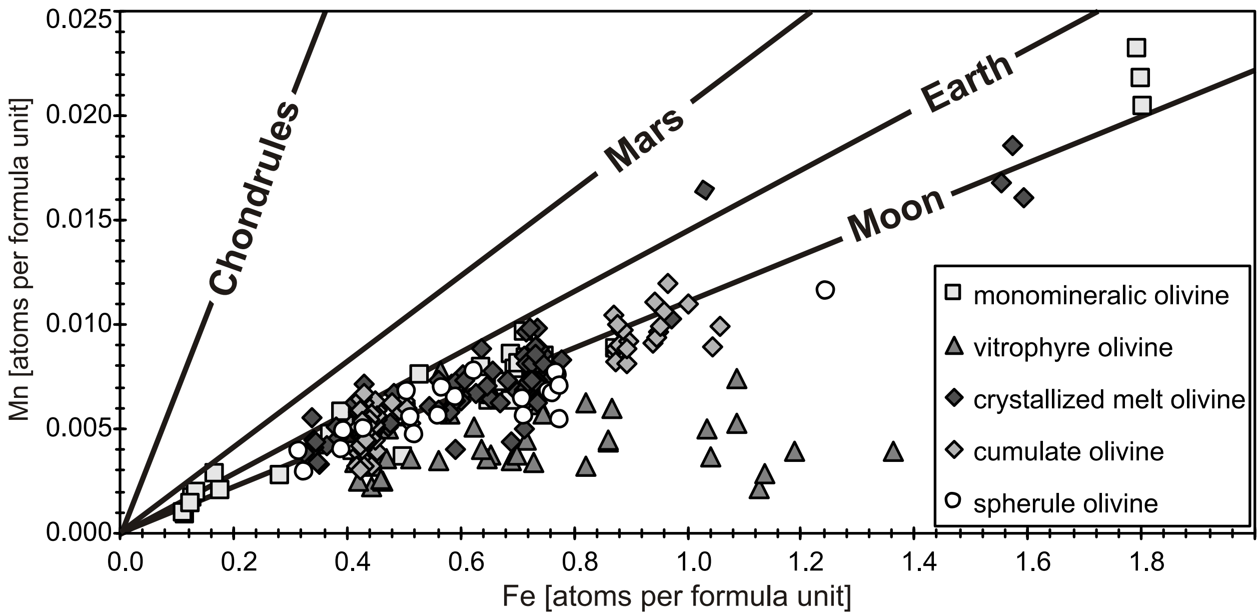


Wittmann et al. fig. 11

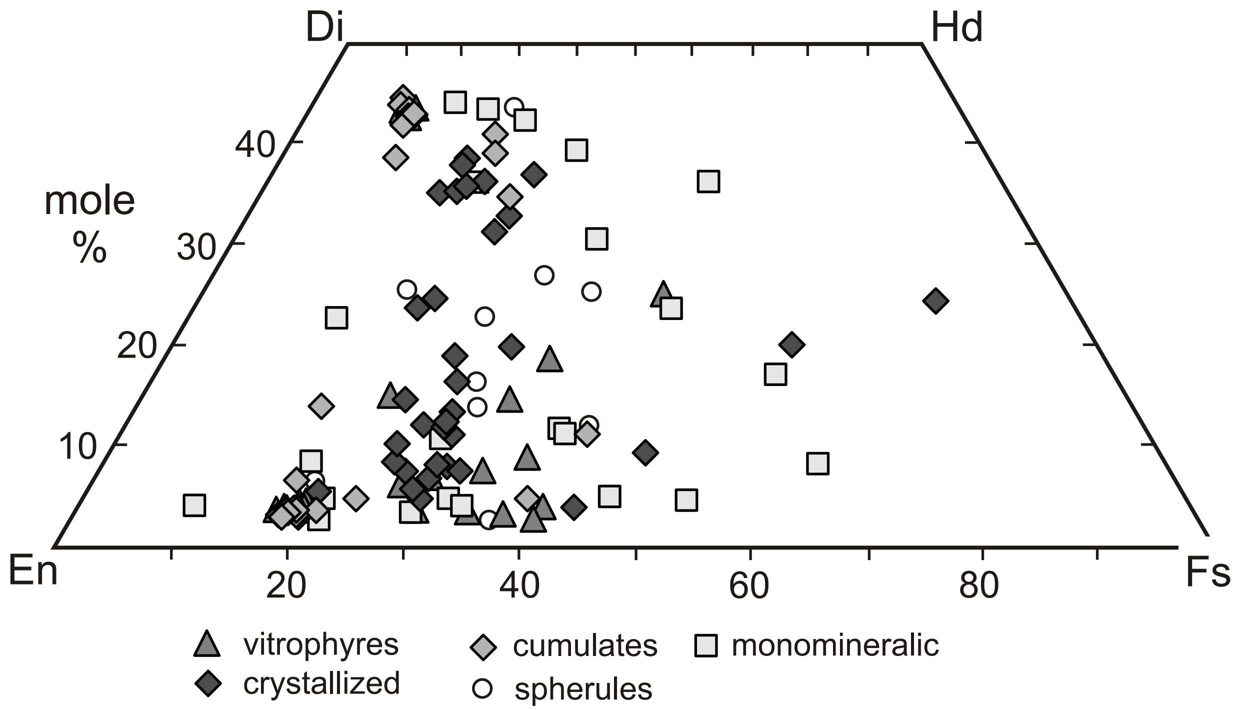


Wittmann et al. fig. 12

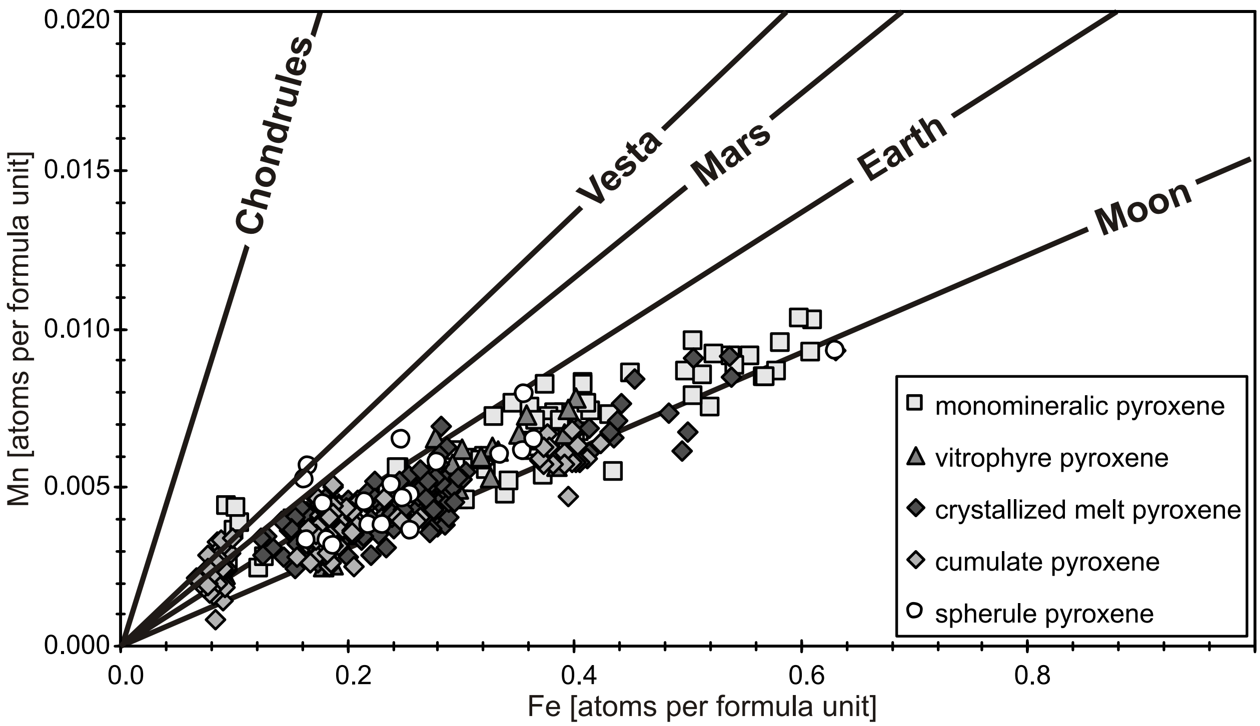


Wittmann et al. fig. 13

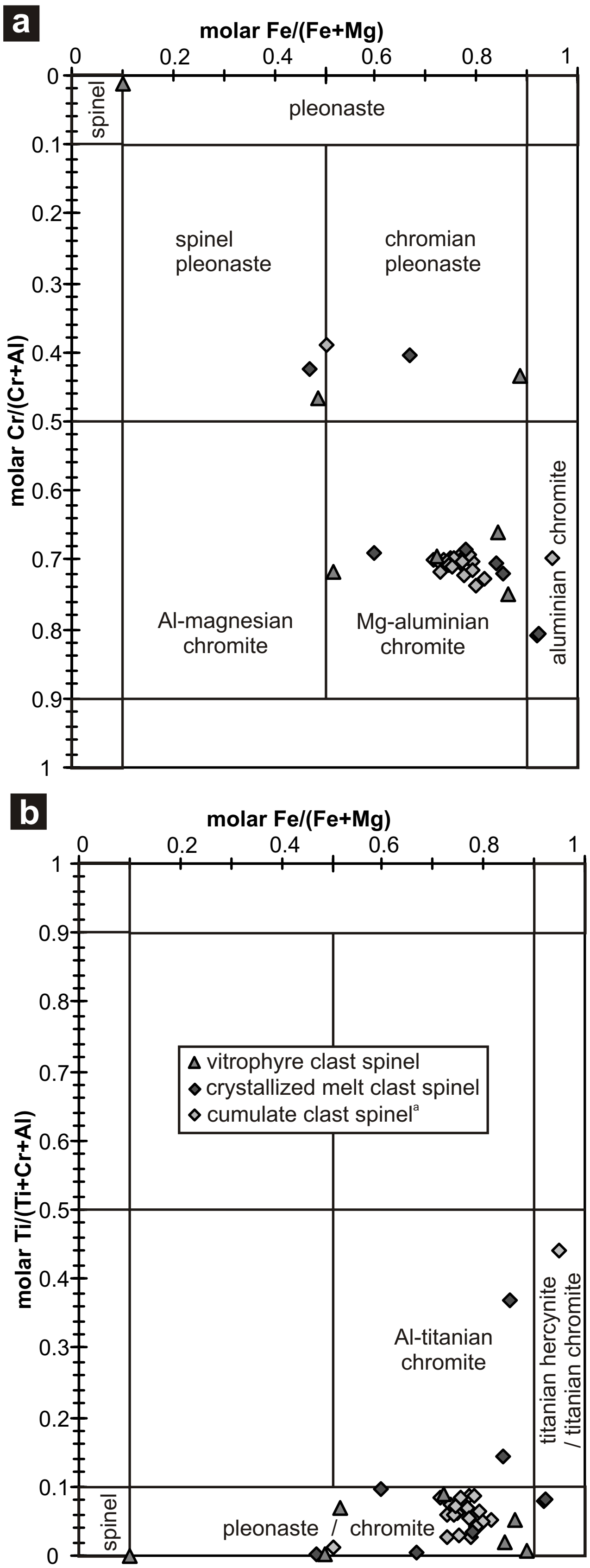


Wittmann et al. fig. 14

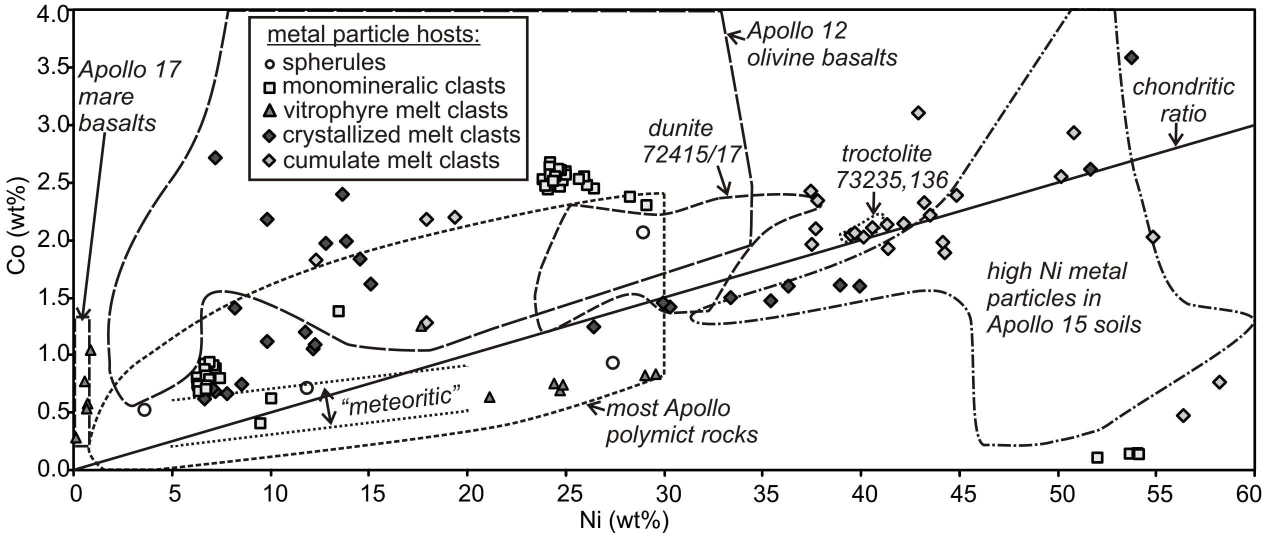


Wittmann et al. fig. 15

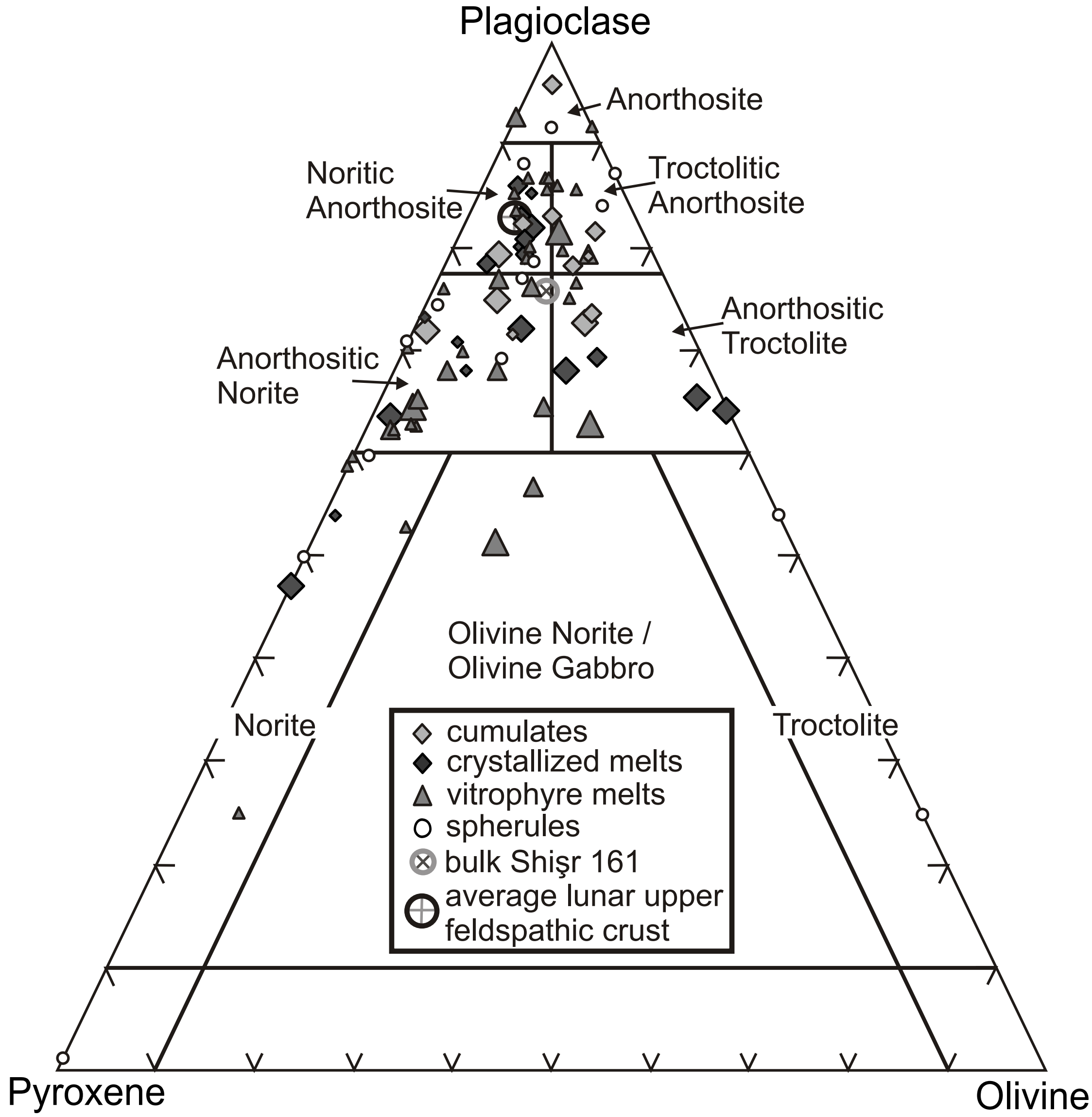


Wittmann et al. fig. 16

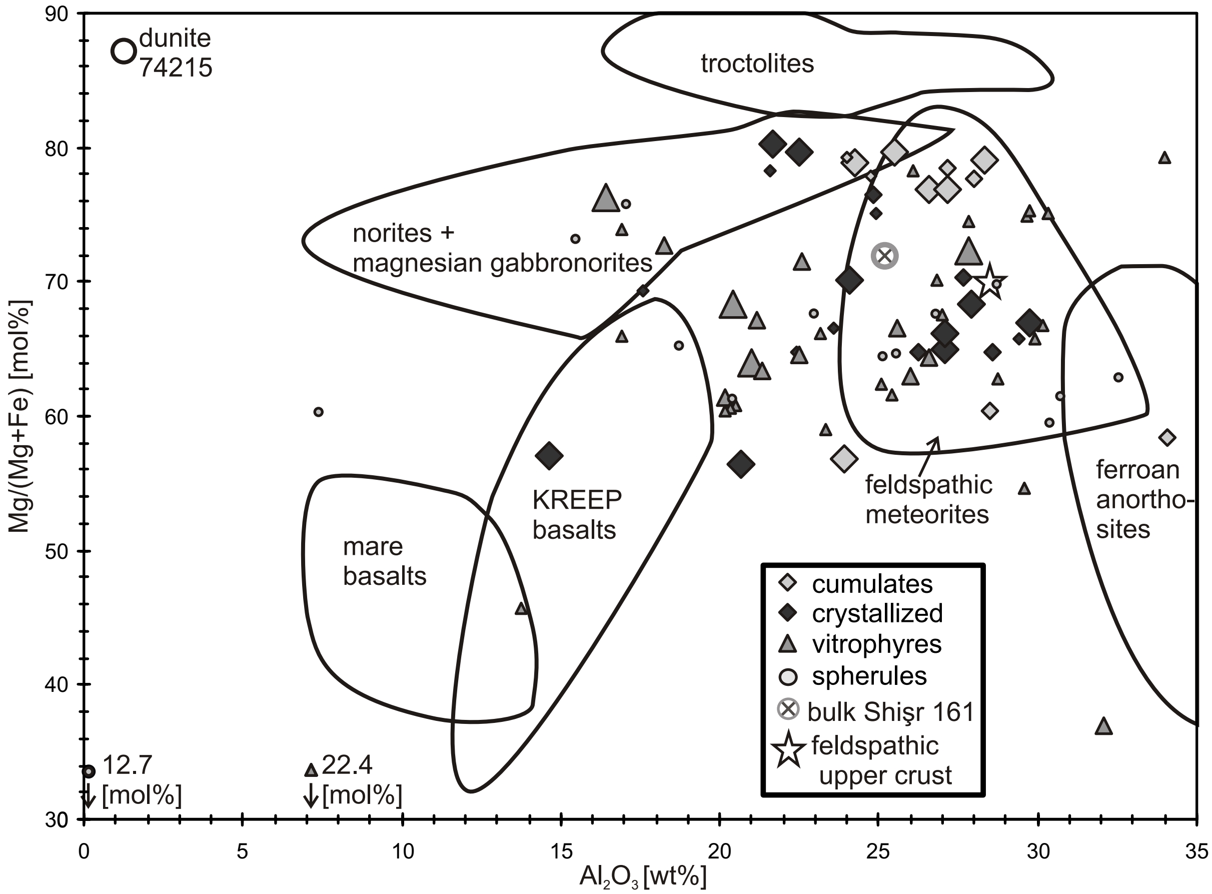


Wittmann et al. fig. 17

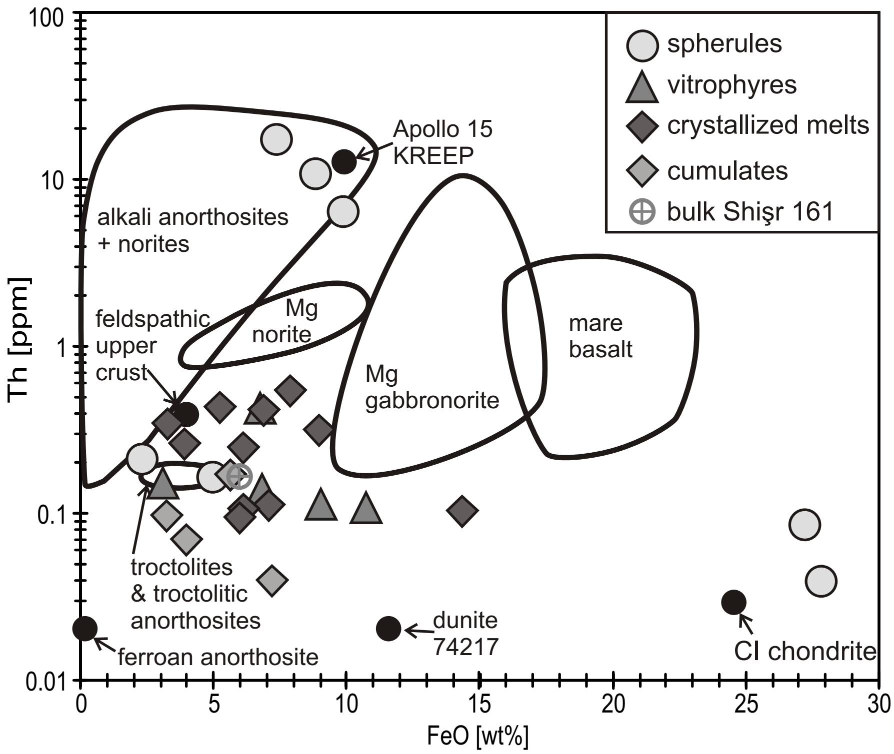


Wittmann et al. fig. 18

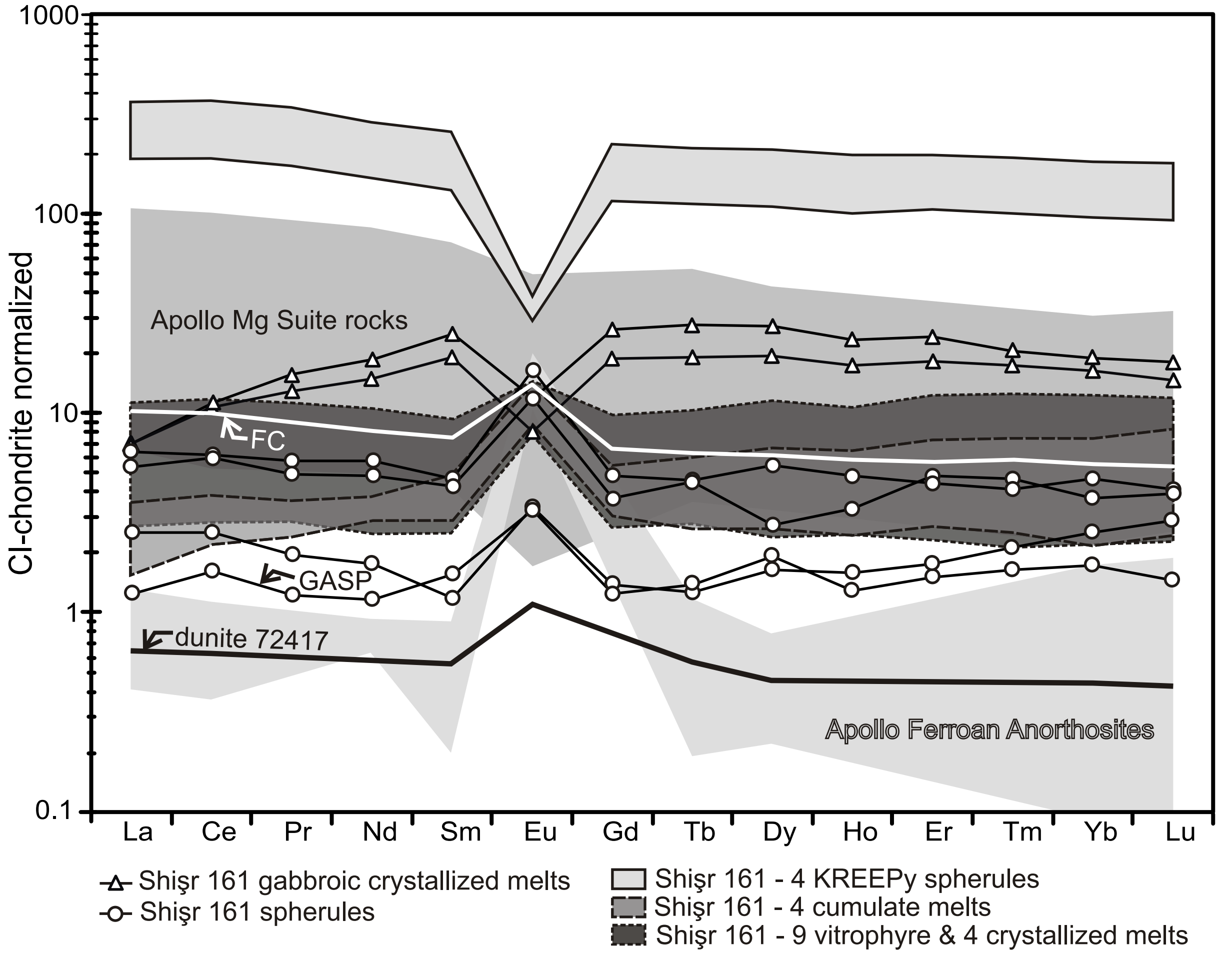


Wittmann et al. fig. 19

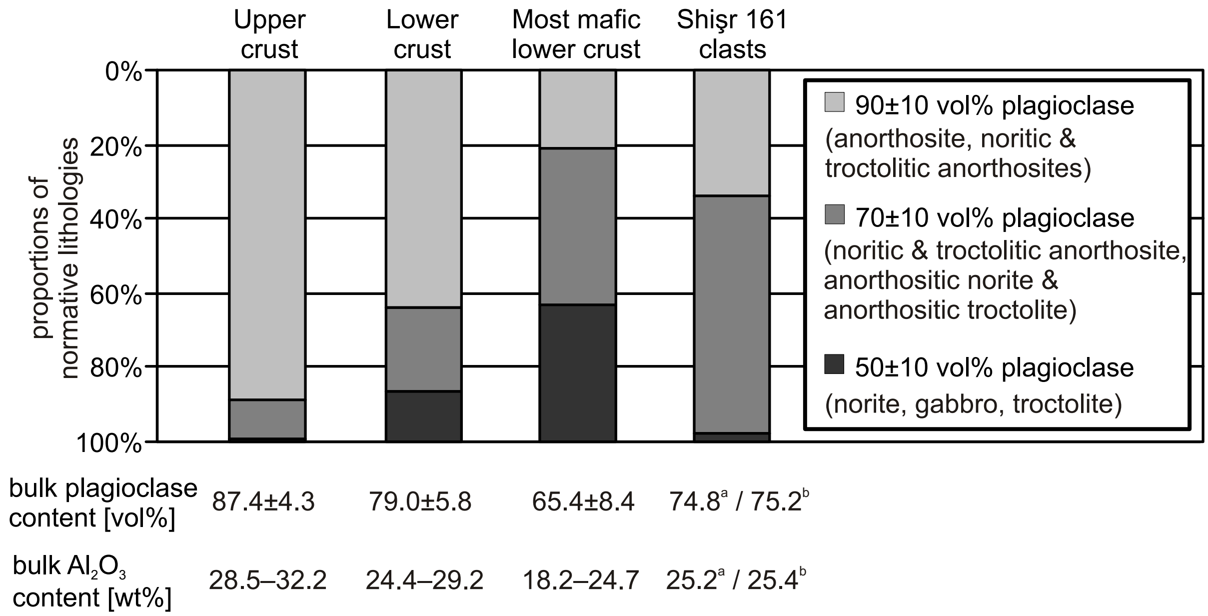


Wittmann et al. fig. 20

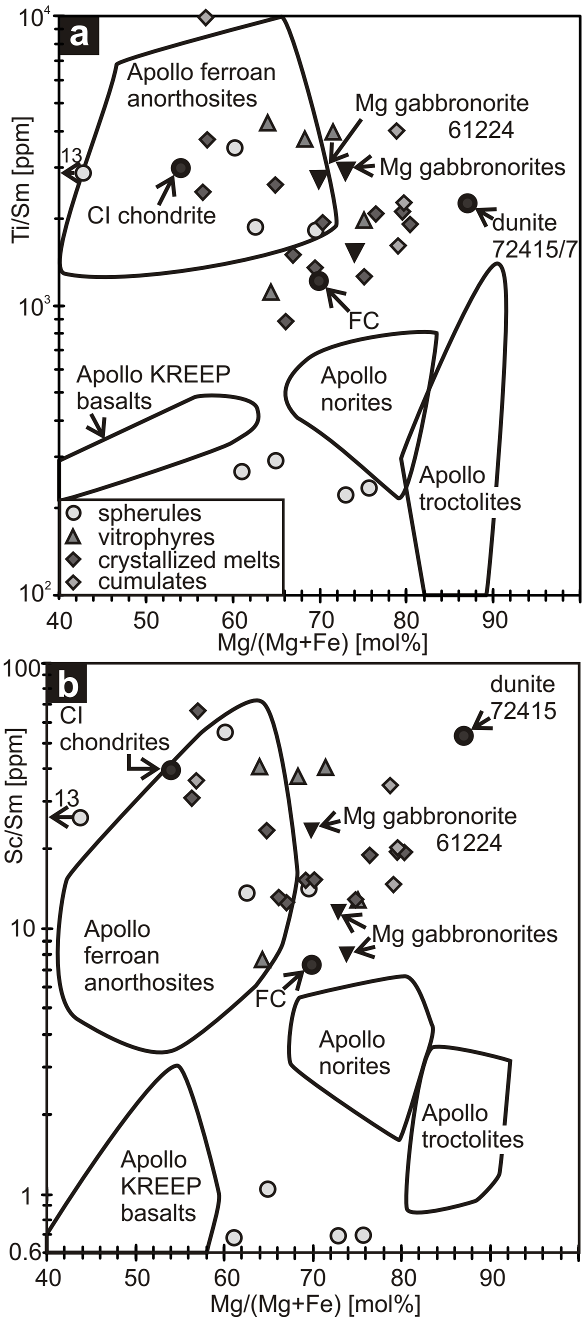


Wittmann et al. fig. 21

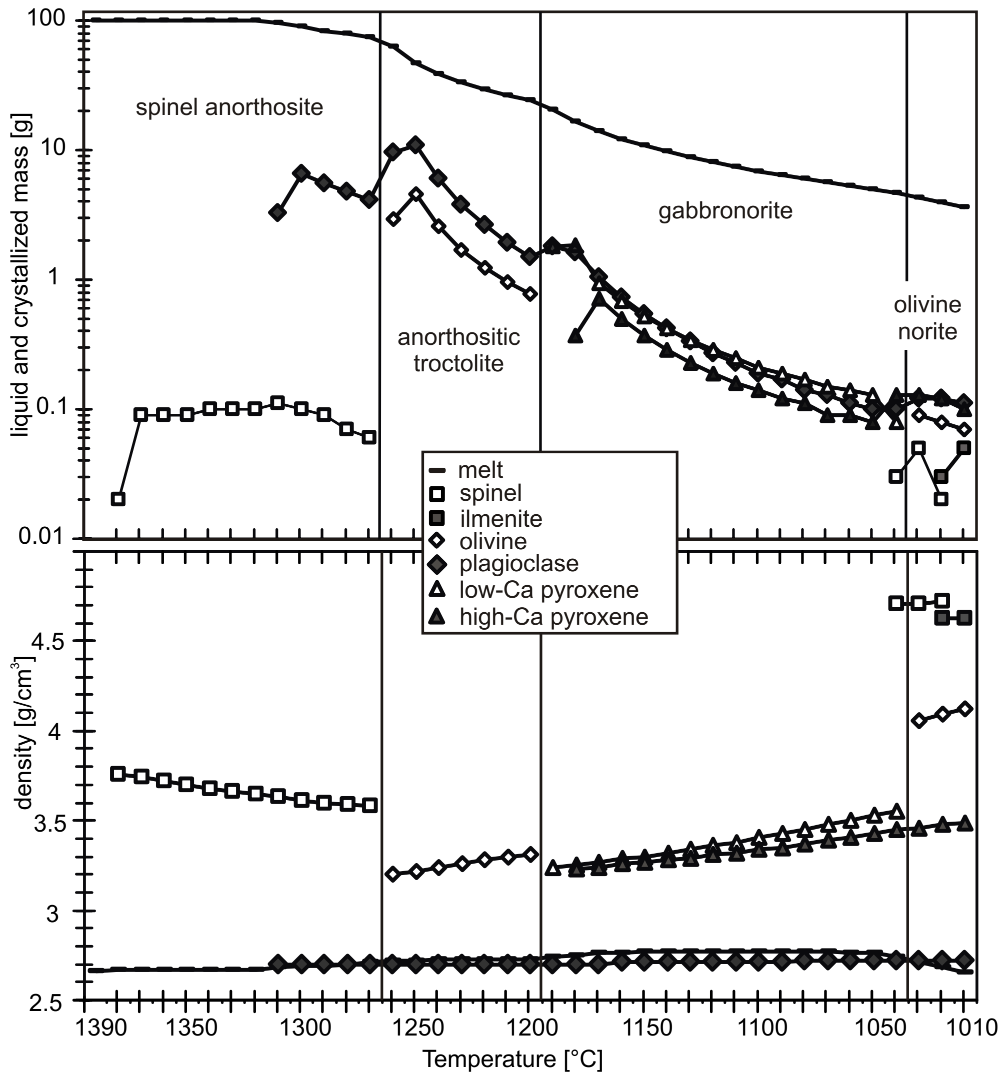


Wittmann et al. fig. 22

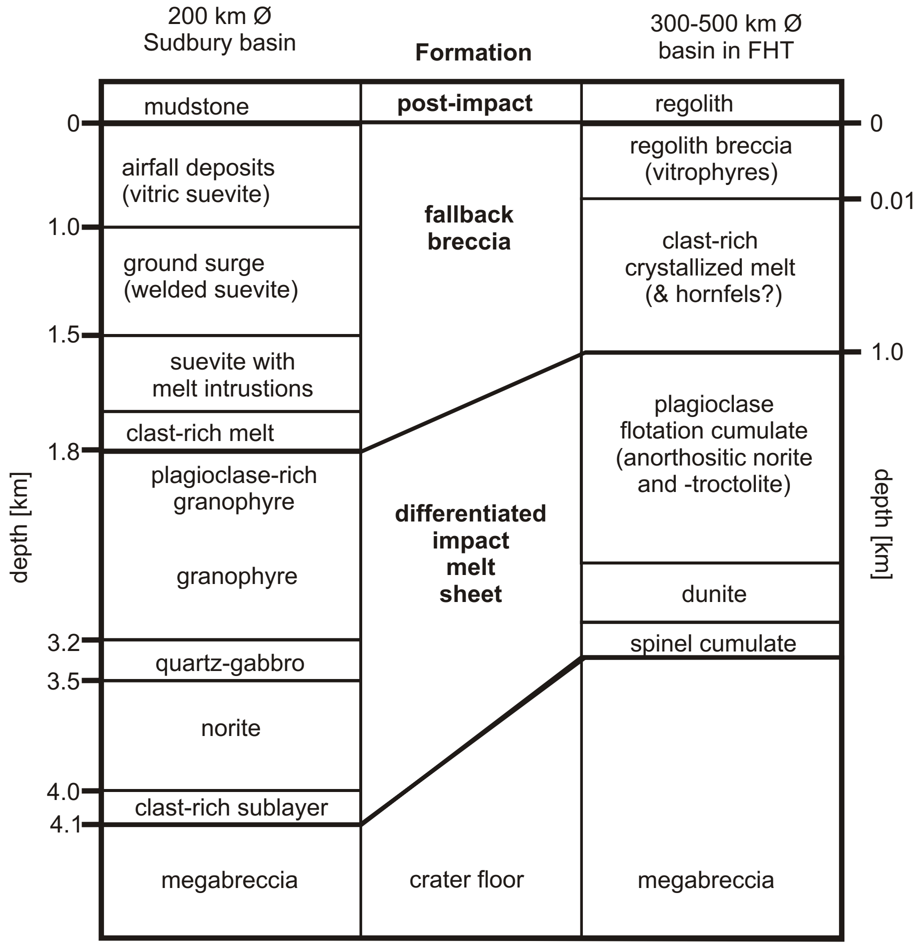


Wittmann et al. fig. 23

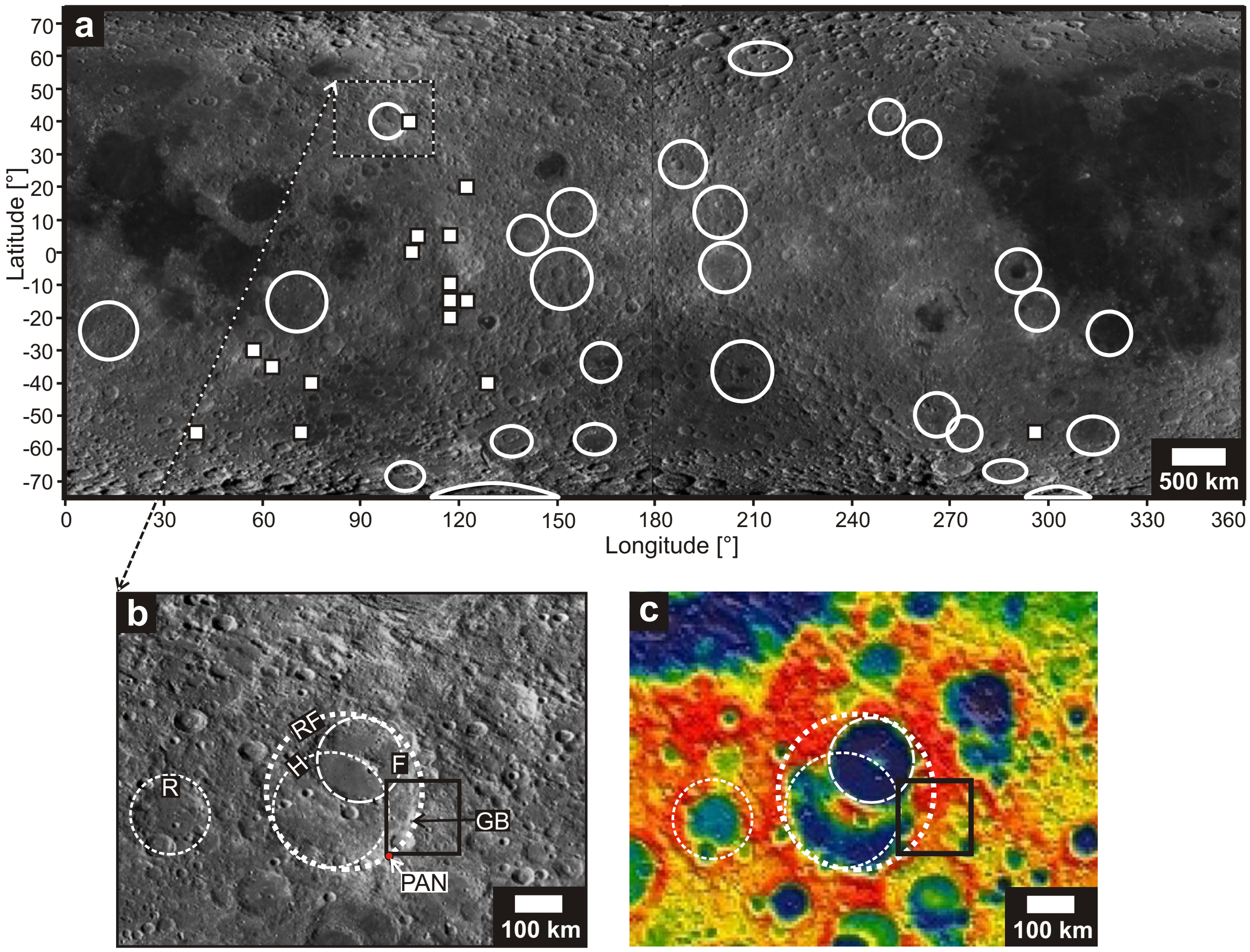


Wittmann et al. fig. 24